UNIVERSITY OF LEEDS

Enhancing Magnetic Endoscope Manoeuvrability Using Tip-Growing and Developable Roller Mechanisms for Deep Navigation and Virtual Biopsies

Nikita Jasmine Greenidge

Submitted in accordance with the requirements for the degree of Doctorate of Philosophy

The University of Leeds

Faculty of Engineering

School of Electronic and Electrical Engineering

June 2025

Intellectual Property and Publication Statements

I confirm that the work submitted is my own, except where work which has formed part of jointly authored publications has been included. My contribution and that of the other authors to this work are explicitly indicated below. I confirm that appropriate credit has been given within the thesis where reference has been made to the work of others. The author's contribution is notated by the initials **N.J.G.**

In reference to IEEE copyrighted material which is used with permission in this thesis, the IEEE does not endorse any of University of Leed's products or services. Internal or personal use of this material is permitted. If interested in reprinting/republishing IEEE copyrighted material for advertising or promotional purposes or for creating new collective works for resale or redistribution, please go to `http://www.ieee.org/publications_standards/publications/rights/rights_link.html` to learn how to obtain a License from RightsLink. If applicable, University Microfilms and/or ProQuest Library, or the Archives of Canada may supply single copies of the dissertation.

Chapter 2 includes work from the jointly authored publication:

© 2025 IEEE. Reprinted, with permission, from **N.J. Greenidge**, C. Marzi, B. Calmé, J. W. Martin, B. Scaglioni, F. Mathis-Ullrich, Pietro Valdastri, "Designing a Magnetic Endoscope for In Vivo Contact-Based Tissue Scanning Using Developable Roller", 2025 IEEE/RSJ International Conference on Intelligent Robots and Systems (IROS), Hangzhou, China, 2025.

The contribution to this work is as follows:

- Conceptualization: **N.J.G.**, C.M.
- Methodology: **N.J.G.**, C.M., J.W.M.
- Investigation: **N.J.G.**, C.M., J.W.M.
- Funding: F.M., P.V.
- Supervision: B.S., F.M., P.V.
- Writing—original draft: **N.J.G.**, C.M., B.C.
- Writing—review & editing: **N.J.G.**, C.M., B.C., F.M., P.V.

Chapter 3 includes work from the jointly authored publication:

Reproduced/modified from **N. J. Greenidge**, B. Calmé, A. C. Moldovan, B. Abaravicius, J. W. Martin, N. Marahrens, J. Woolfrey, B. Scaglioni, D. S. Chathuranga, S. Mitra, S. Cochran, P. Valdastri, "Harnessing the oloid shape in magnetically driven robots to enable high-resolution ultrasound imaging", Science Robotics, vol. 10, no. 100, p. eadq4198, Mar. 2025, DOI: 10.1126/scirobotics.adq4198, AAAS [1]

The contribution to this work is as follows:

- Conceptualization: **N.J.G.**, P.V.
- Methodology: **N.J.G.**, B.C., J.W.M., N.M., D.S.C.
- Investigation: **N.J.G.**, B.C., A.C.M., B.A., J.W.M.
- Visualization: **N.J.G.**, B.C.
- Funding: S.M., S.C., P.V
- Supervision: B.S., S.M., S.C, P.V.
- Writing—original draft: **N.J.G.**, B.C., A.C.M.
- Writing—review & editing: **N.J.G.**, B.C., A.C.M., B.A., J.W., B.S., S.C., P.V.

Chapter 4 includes work from the jointly authored publication:

N. G. Kim*, **N. J. Greenidge***, J. Davy, S. Park, J. H. Chandler, J. Ryu, P. Valdastri, 'External Steering of Vine Robots via Magnetic Actuation', Soft Robotics (Vol. 12, No. 2), pp.159 - 170. Copyright 2024, Mary Ann Liebert, Inc., publishers., DOI: 10.1089/soro.2023.0182. [2]

* N. G. Kim and **N. J. Greenidge** are to be considered co-first authors on this work. However, N. J. Greenidge is to be considered as the lead author due to the contributions as follows:

- Conceptualization: **N.J.G.**, J.R., P.V.
- Methodology: **N.J.G.**, J.D.
- Investigation: **N.J.G.**, J.D., N.G.K., S.P.
- Design of magnetic control systems: **N.J.G.**, J.D.
- Design and development of mechatronic systems: N.G.K., S.P.
- Funding: J.R., P.V.
- Supervision: J.R., P.V.
- Writing—original draft: **N.J.G.**, J.D.
- Writing—review & editing: **N.J.G.**, J.D., N.G.K., S.P., J.R., P.V.

Acknowledgements

I would like to thank my supervisor Professor Pietro Valdastri who has supported me in all my endeavors and given me the space to grow during my time at the STORM Lab.

"I have had so many rainbows in my clouds, I have had a lot of clouds, but I have had so many rainbows...and the thing to do, it seems to me, is to prepare yourself so that you can be a rainbow in somebody else's cloud." - Maya Angelou

Thank you to everyone who has ever shown me kindness. *Ubuntu* - "I am because we are" - has shaped this journey in more ways than one. What some may know only as a Linux operating system, ubiquitous in the field of robotics, is in fact named after an African philosophy that celebrates community, shared humanity, and interconnectedness. It reminds us that no success is achieved alone; we are endlessly shaped by those around us. Reaching this point is the result of every human connection I've been fortunate to share—from Saint Lucia, my island home, to every place this journey has led me. The smallest acts of kindness have made an unimaginable difference, leaving my acknowledgements list truly infinite. Please know that I carry your kindness with me, as a reminder to be a rainbow in somebody else's cloud.

To my friends and family, who support everything I do in all ways, always - thank you.

I acknowledge the use of ChatGPT-4 (OpenAI) in proofreading my final draft.

Abstract

Early detection of gastrointestinal (GI) cancers significantly improves survival outcomes; however, current diagnostic pathways are limited by manual procedures that are time-consuming, uncomfortable, and resource-intensive. In many health systems, especially those constrained by staff shortages or infrastructure, routine endoscopic screening remains inaccessible or inefficient. Colonoscopy, the gold standard for detecting colorectal cancer, is associated with discomfort, sedation requirements, and steep operator learning curves. The global push toward automation and patient-centric technologies has fueled interest in robotic solutions that can enhance the reach, dexterity, and diagnostic capability of endoscopic tools.

This thesis is motivated by the clinical imperative to make GI cancer detection faster, safer, and more scalable using intelligent magnetically actuated robotic platforms. Chapter 2 introduces an oloid-shaped, magnetically actuated endoscope that restores rotational dexterity and achieves stable contact with the GI wall during 74% of rolling motion in vivo. Building on this, Chapter 3 integrates closed-loop magnetic control and high-resolution micro-ultrasound imaging, enabling autonomous three-dimensional subsurface lesion detection and mapping, validated in benchtop and porcine in vivo models. Chapter 4 presents a tip-growing, magnetically steered "vine robot" endoscope with a minimum bending radius of 3.85 cm and stable, shear-free navigation, along with promising initial results for magnetic retraction to support deeper GI tract navigation.

My work is situated at the intersection of magnetic actuation, soft robotics, and minimally invasive diagnostic techniques.

Acronyms

2D Two- Dimensional.

3D Three-Dimensional.

CRC Colorectal Cancer.

DoF Degrees of Freedom.

EPM External Permanent Magnet.

fPAM Fabric Pneumatic Artificial Muscle.

GI Gastrointestinal.

ICC Irrigation, and Camera Cleaning.

IPM Internal Permanent Magnet.

LED Light Emitting Diode.

MFE Magnetic Flexible Endoscope.

microUS micro-ultrasound.

MVR Magnet Vine Robot.

NBI Narrowband Imaging.

OCT Optical Coherence Tomography.

OMD Oloid-shaped Magnetic Device.

OME Oloid-shaped Magnetic Endoscope.

OME-U Oloid-shaped Magnetic Endoscope - Ultrasound.

PCB Printed Circuit Board.

ROS Robot Operating System.

sPAM Series Pneumatic Artificial Muscle.

US ultrasound.

WLI White Light Imaging.

Contents

List of Figures

List of Tables

Chapter 1

Introduction

Diseases of the Gastrointestinal (GI) tract are a growing global challenge in healthcare, with GI cancers, most notably Colorectal Cancer (CRC), being among the leading causes of cancer-related mortality worldwide [1]. Early detection of CRC is particularly important because the disease progresses slowly from identifiable precancerous lesions, offering a critical window for intervention [2]. In high-income countries, where the incidence of CRC is highest, this understanding has led to the widespread adoption of national screening programs. The development of these programs over the past few decades has been strongly associated with significant reductions in CRC incidence and mortality [1], [3]. At their core is the flexible endoscope, the clinical gold standard that allows direct visualization of the entire colon, the ability to take tissue biopsies and the removal of lesions with high efficacy [2]–[4].

1.1 Standard Flexible Endoscopy

Despite its significant clinical benefits, standard flexible endoscopy has inherent limitations that hinder both its performance and global adoption [2]. These limitations are especially problematic in regions where CRC screening programs have not been implemented. Although such regions often report lower CRC incidence, their mortality rates remain comparable to those in high-incidence countries, reflecting late-stage detection

and limited access to early diagnostic tools. As socioeconomic development drives a shift toward more Westernized lifestyles, incidence rates in these areas are rising [1], highlighting the growing need for scalable screening. Moreover, even in well-resourced settings, the clinical effectiveness of flexible endoscopy is compromised by incomplete procedures and high adenoma miss rates, particularly in anatomically challenging patients such as women and individuals with tortuous colons [5], [6]. These limitations underscore the need for alternative or improved screening technologies that are both effective and broadly deployable.

Originally developed in the 1960s, the flexible endoscope is a manually operated device with cable-driven steering, a camera, and illumination for real-time visualization, and a working channel capable of performing diagnostic and therapeutic interventions within a single procedure [7]. Advancement of the scope is achieved by pushing it from the proximal end, which stretches the colon wall to navigate the tortuous bends of the colon [8]. This can lead to the formation of loops, where the scope coils within the colon and stretches the mesentery, resulting in significant patient discomfort, a small risk of perforation, and necessitating sedation in many cases [9].

Manipulating the scope involves simultaneously pushing and twisting the shaft while adjusting multiple dials on the scope's handle to deflect the tip, requiring repetitive, forceful, and sustained hand movements while maintaining awkward wrist postures [10]. This combination of physical demands leads to significant ergonomic strain and a notable prevalence of musculoskeletal injuries among endoscopists [11]. Female endoscopists are disproportionately affected by suboptimal instrument designs that do not accommodate smaller hand sizes and grip strengths [12]. In addition, manipulating standard flexible endoscopes requires significant technical skill, with a steep learning curve and prolonged training periods [13], [14]—contributing to reduced global capacity at a time when demand for colonoscopy screening continues to rise [15].

Beyond the challenges of manipulation, the mechanical complexity and reusability of flexible endoscopes demand extensive cleaning and reprocessing workflows [16], [17]. These

processes significantly increase costs and pose a persistent risk of cross-contamination, even in high-resource settings [17], [18]. In lower-resource regions, where the initial investment in endoscopy suites and sterile reprocessing infrastructure is often prohibitive, these requirements present a major barrier to adoption [1], [16].

1.2 Capsule Endoscopy

Capsule endoscopy emerged in the early 2000s as a gentler, patient-friendly alternative to traditional endoscopic procedures [19]. Initially developed for the small bowel, an area notoriously difficult to access with conventional scopes, these swallowable devices enabled passive visualization of the GI tract. However, their diagnostic yield is limited by the inability to steer and control their movement [20]. In response, actively controlled capsules, including those guided by external magnetic fields [21], have recently been introduced to the market (NaviCam). These systems offer directional control, improving image acquisition and lesion detection, but still lack the capacity to perform therapeutic interventions, such as biopsies or polyp removal.

1.3 Robotic Endoscopy

To address the challenges in navigation and reduce training bottlenecks, various tethered robotic endoscope systems have been developed [22]. These include inchworm-inspired soft pneumatic robots [23], [24], pressure-driven propulsion devices [25], and magnetically actuated endoscopes [26]–[29]. These platforms aim to reduce the operator's cognitive and physical load by replacing complex manual maneuvers with intuitive joystick controls or autonomous navigation [30], [31]. With the integration of AI-based diagnostic aids, such as Medtronic's "GI Genius" lesion detection system and the development of colon reconstruction [32], robotic endoscopes are poised to enable parallelized workflows, allowing a single clinician to supervise multiple procedures [8]. Nevertheless, the only robotic platform currently adopted in clinical practice, the Endotics system, still falls short of matching the speed and effectiveness of standard colonoscopy.

1.4 Magnetic Flexible Endoscopy

Magnetically manipulated, soft-tethered endoscopes combine the therapeutic capabilities of standard flexible endoscopes scopes with the advantages of "pull" locomotion and progressively more advanced autonomy, further bridging the gap between traditional and robotic endoscopy [30], [31]. Magnetically manipulated platforms have demonstrated comparable traversal times, reduced discomfort and pain, and improved ease of use [30], [33], but have yet to demonstrate diagnostic abilities beyond those of traditional endoscopes.

1.5 Contributions

One frontier in GI diagnostics is the concept of virtual biopsy, which is a real-time, non-invasive tissue characterization using advanced imaging technologies such as micro-ultrasound (microUS) or Optical Coherence Tomography (OCT). These modalities offer the possibility of in situ histological assessment, eliminating the need for biopsies and subsequent laboratory processing time and costs [34]. However, its clinical integration has been limited. Current implementations rely on rigid or single-element probes [35] that are difficult to control and require highly skilled manipulation. Previous work on embedding microUS into magnetic endoscopes [26] demonstrated the promise of such integration but also exposed a core limitation of magnetic control: the inability to apply torque around a magnet's magnetization axis. This restriction hinders rotational scanning, making full 3D imaging, which is crucial for virtual biopsies, difficult to achieve.

Another critical challenge with magnetically manipulated endoscopes is that the propulsion performance declines in highly tortuous anatomies owing to increased tether drag, which combats the magnetic advancement force. One workaround has been to increase the size of the embedded magnets; however, this introduces trade-offs in terms of safety, cost, and spatial constraints. Addressing this issue would not only improve completion rates but could also extend the reach of these systems into the small bowel, an area still

underserved by current technologies.

This thesis seeks to expand the dexterity, diagnostic ability, and depth of navigation of magnetically actuated endoscopes (see Figure 1.1. It explores the integration of microUS arrays capable of performing 3D scans and introduces a novel solution, bioinspired vine-like tip-growing technology, to mitigate the effects of tether drag. Together, these advances aim to build a more robust, steerable, and diagnostically capable platform, pushing us closer to a future in which robotic endoscopy is not only more accessible but also more precise, scalable, and intelligent.

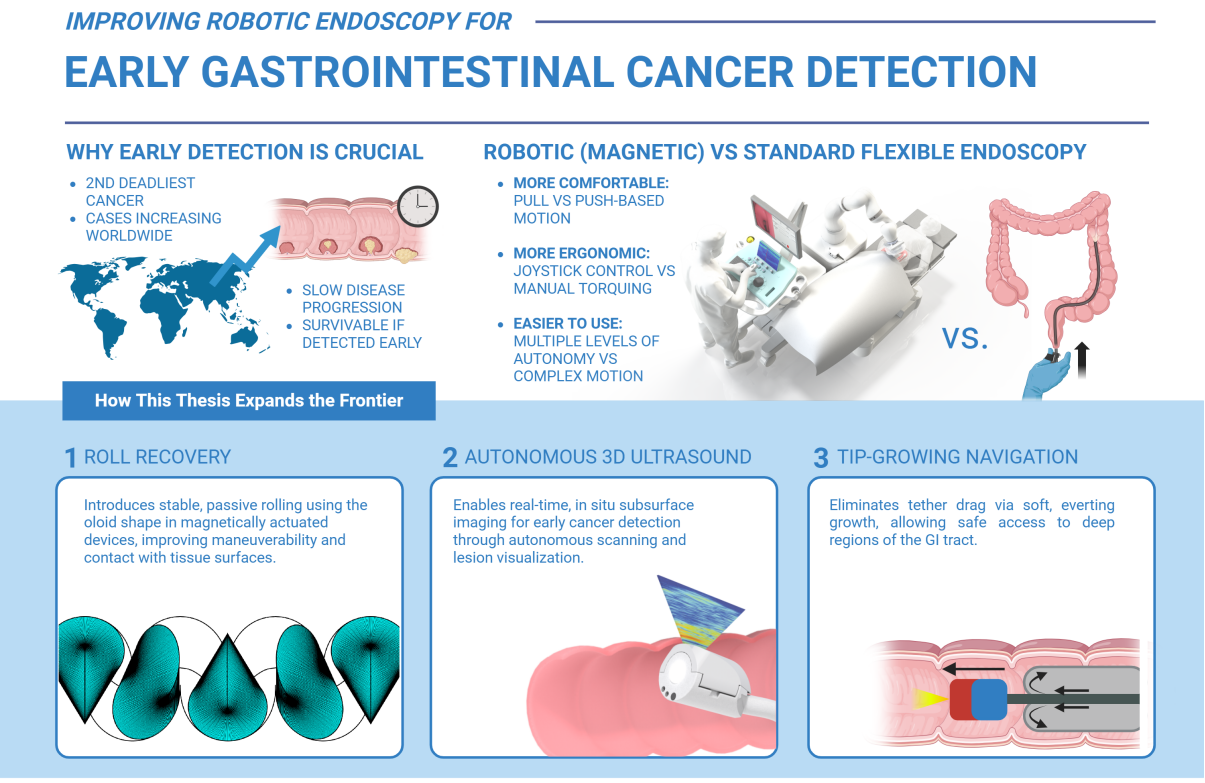

Figure 1.1: **Graphical Abstract:** This thesis addresses critical limitations in colorectal cancer screening by advancing the design of magnetically actuated endoscopes. It introduces: (1) oloid-inspired geometry for enhanced rolling and maneuverability, (2) integrated micro-ultrasound with closed-loop control for real-time, in situ tissue characterization, and (3) tip-growing soft robotic mechanisms to overcome tether drag and improve navigation in tortuous anatomies. Created in `https://BioRender.com`

1.6 Clinical Impact and Translational Outlook

The work presented in this thesis addresses critical bottlenecks in CRC screening and gastrointestinal diagnostics, with implications for cost reduction, improved access, and increased patient adherence to screening protocols.

The integration of oloid-based rotational control and autonomous subsurface scanning introduces the possibility of virtual biopsy, which could drastically reduce reliance on physical tissue extraction and histopathology. This can cut per-procedure diagnostic costs by eliminating consumables (e.g., biopsy forceps, pathology lab processing) and shortening diagnostic timeframes. Additionally, automated image acquisition and lesion detection support task-shifting to less experienced operators, reducing the dependence on highly trained specialists and thus lowering operational costs in resource-constrained environments.

The tip-growing magnetic endoscope tackles one of the most pressing limitations of conventional and magnetic endoscopy—tether drag in tortuous anatomies—by introducing a shear-free propulsion mechanism that allows deeper navigation with minimal force. This could increase completion rates in anatomically challenging patients, reducing the need for repeated procedures and associated costs.

From an accessibility and equity standpoint, these innovations are especially impactful. The simplified joystick-based or semi-autonomous control interfaces dramatically reduce the training burden compared to conventional colonoscopy, which typically requires 200–300 supervised procedures to achieve competence. Robotic and magnetically actuated systems could enable competency with much fewer procedures, thereby expanding the pool of eligible operators, especially in regions facing gastroenterologist shortages. In terms of adherence, minimizing pain, sedation, and procedural complexity can lead to significantly higher screening uptake.

1.7 Thesis Structure

This thesis presents a series of design innovations detailed in Chapters 2 to 4, which contain material from peer-reviewed journal and conference publications where the author is either the first or joint-first (*) author. These chapters represent the core contributions of this thesis, which aims to advance the design of magnetic endoscopes for the early detection of GI cancers. Chapter 5 concludes the thesis with a discussion of the key findings and future work directions. Chapters 2 to 4 each address one or more of the challenges outlined in Chapter 1, as follows:

- **Chapter 2:** This chapter addresses the limited dexterity of magnetically actuated endoscopic systems by introducing a method to recover rotational control around the longitudinal axis. Developable roller geometry is explored, specifically the oloid shape. A soft-tethered magnetic endoscope incorporating an oloid shape was proposed. The oloid enables passive rolling and consistent contact with the surface. The device, built with clinically relevant dimensions and integrated with contact sensors, was evaluated in a porcine non-survival model. The results show that stable contact with the GI wall during over 100° of rolling was maintained for 74% of the motion. This design enhances magnetic maneuverability and lays the foundation for the future integration of contact-based subsurface sensing within minimally invasive gastrointestinal procedures.

  N.J. Greenidge, C. Marzi, B. Calmé, J. W. Martin, B. Scaglioni, F. Mathis-Ullrich, Pietro Valdastri, "Designing a Magnetic Endoscope for In Vivo Contact-Based Tissue Scanning Using Developable Roller", 2025 IEEE/RSJ International Conference on Intelligent Robots and Systems (IROS), Hangzhou, China, 2025.

- **Chapter 3:** This chapter extends the work presented in Chapter 2 by developing a closed-loop control strategy for the magnetic manipulation of an oloid-shaped endoscope. A control model was proposed and evaluated on various benchtop surfaces. A 28 MHz microUS array was integrated into the device to enable real-time

subsurface imaging. A contact detection and autonomous scanning algorithm was introduced and validated through in vitro and in vivo experiments using a porcine non survival model. The system was used to perform sweeping motions, detect artificially injected lesions, and generate 3D subsurface images of the GI tissue.

N. J. Greenidge, B. Calmé, A. C. Moldovan, B. Abaravicius, J. W. Martin, N. Marahrens, J. Woolfrey, B. Scaglioni, D. S. Chathuranga, S. Mitra, S. Cochran, P. Valdastri, "Harnessing the oloid shape in magnetically driven robots to enable high-resolution ultrasound imaging", Science Robotics, vol. 10, no. 100, p. eadq4198, Mar. 2025, doi: 10.1126/scirobotics.adq4198. [36]

- **Chapter 4:** This chapter investigates the use of the everting nature of tip-growing robots, or "vine robots," to minimize tether drag and provide stronger axial force in magnetic flexible endoscopes to improve access to high-curvature and deep regions of the GI tract. A 25 mm diameter tip-growing magnetic endoscope is presented, which is capable of achieving a minimum bending radius of 3.85 cm at 30 kPa internal pressure. The system demonstrated stable shear-free navigation. Initial results on magnetically enabled retraction are also presented, a feature that is an open challenge in the world of vine robots but is necessary for clinical applications.

  N. G. Kim*, **N. J. Greenidge***, J. Davy, S. Park, J. H. Chandler, J. Ryu, P. Valdastri, 'External Steering of Vine Robots via Magnetic Actuation', Soft Robotics, Sep. 2024, doi: 10.1089/soro.2023.0182. [37]

  * N. G. Kim and N. J. Greenidge are to be considered co-first authors on this work. However, N. J. Greenidge is to be considered as the lead author due to the contributions listed in the "Intellectual Property and Publication Statements" section of this dissertation.

- **Chapter 5:** Conclusions and Future Directions.

References

[1] F. Bray, M. Laversanne, H. Sung, *et al.*, "Global cancer statistics 2022: GLOBOCAN estimates of incidence and mortality worldwide for 36 cancers in 185 countries," en, *CA: A Cancer Journal for Clinicians*, vol. 74, no. 3, pp. 229–263, 2024, ISSN: 1542-4863. DOI: 10.3322/caac.21834. [Online]. Available: https://onlinelibrary.wiley.com/doi/abs/10.3322/caac.21834.

[2] K. Simon, "Colorectal cancer development and advances in screening," *Clinical Interventions in Aging*, vol. 11, pp. 967–976, Jul. 2016, ISSN: 1176-9092. DOI: 10/gm78hd. [Online]. Available: https://www.ncbi.nlm.nih.gov/pmc/articles/PMC4958365/.

[3] F. E. Shekleton and M. Okocha, "UK Screening and Surveillance For Bowel Cancers," eng, in *StatPearls*, Treasure Island (FL): StatPearls Publishing, 2025. [Online]. Available: http://www.ncbi.nlm.nih.gov/books/NBK599509/.

[4] Y. Hazewinkel and E. Dekker, "Colonoscopy: Basic principles and novel techniques," en, *Nature Reviews Gastroenterology & Hepatology*, vol. 8, no. 10, pp. 554–564, Oct. 2011, ISSN: 1759-5053. DOI: 10.1038/nrgastro.2011.141. [Online]. Available: https://www.nature.com/articles/nrgastro.2011.141.

[5] J. C. Anderson, M. Dorfman, Z. Alpern, *et al.*, "Colonoscopy in Women: Is It Still More Difficult Than Colonoscopy in Men and Is a Low BMI Still a Challenge?" English, *Gastrointestinal Endoscopy*, vol. 65, no. 5, AB363, Apr. 2007, ISSN: 0016-5107, 1097-6779. DOI: 10.1016/j.gie.2007.03.940. [Online]. Available: https://www.giejournal.org/article/S0016-5107(07)01431-9/fulltext#relatedArticles.

[6] B. P. Saunders, M. Fukumoto, S. Halligan, *et al.*, "Why is colonoscopy more difficult in women?" English, *Gastrointestinal Endoscopy*, vol. 43, no. 2, pp. 124–126, Feb. 1996, ISSN: 0016-5107, 1097-6779. DOI: 10.1016/S0016-5107(06)80113-6. [Online]. Available: https://www.giejournal.org/article/S0016-5107(06)80113-6/fulltext.

[7] B. I. Hirschowitz, "Historical perspectives on technology in GI endoscopy," *Techniques in Gastrointestinal Endoscopy*, Emerging Technologies, vol. 5, no. 2, pp. 56–64, Apr. 2003, ISSN: 1096-2883. DOI: 10.1053/tgie.2003.1. [Online]. Available: https://www.sciencedirect.com/science/article/pii/S1096288303800025.

[8] P. Valdastri, M. Simi, and R. J. Webster, "Advanced Technologies for Gastrointestinal Endoscopy," *Annual Review of Biomedical Engineering*, vol. 14, no. 1, pp. 397–429, 2012. DOI: 10.1146/annurev-bioeng-071811-150006. [Online]. Available: https://doi.org/10.1146/annurev-bioeng-071811-150006.

[9] K. Sato, S. Fujinuma, and Y. Sakai, "Evaluation of the Looping Formation and Pain During Insertion into the Cecum in Colonoscopy," en, *Digestive Endoscopy*, vol. 18, no. 3, pp. 181–187, 2006, ISSN: 1443-1661. DOI: 10.1111/j.0915-5635.2006.00601.x. [Online]. Available: https://onlinelibrary.wiley.com/doi/abs/10.1111/j.0915-5635.2006.00601.x.

[10] A. K. Shergill, K. R. McQuaid, and D. Rempel, "Ergonomics and GI endoscopy," en, *Gastrointestinal Endoscopy*, vol. 70, no. 1, pp. 145–153, Jul. 2009, ISSN: 00165107. DOI: 10.1016/j.gie.2008.12.235. [Online]. Available: https://linkinghub.elsevier.com/retrieve/pii/S0016510708032203.

[11] D. E. Yung, T. Banfi, G. Ciuti, A. Arezzo, P. Dario, and A. Koulaouzidis, "Musculoskeletal injuries in gastrointestinal endoscopists: A systematic review," *Expert Review of Gastroenterology & Hepatology*, vol. 11, no. 10, pp. 939–947, Oct. 2017, ISSN: 1747-4124. DOI: 10/gm6dsj. [Online]. Available: https://doi.org/10.1080/17474124.2017.1356225.

[12] A. Bhatt, P. Patil, and N. C. Thosani, "Endoscopy ergonomics: A survey-based study exploring gender differences," English, *Gastrointestinal Endoscopy*, vol. 100, no. 1, pp. 17–26, Jul. 2024, ISSN: 0016-5107, 1097-6779. DOI: 10.1016/j.gie.2024.01.003. [Online]. Available: https://www.giejournal.org/article/S0016-5107(24)00006-3/fulltext.

[13] B. J. Spier, M. Benson, P. R. Pfau, G. Nelligan, M. R. Lucey, and E. A. Gaumnitz, "Colonoscopy training in gastroenterology fellowships: Determining competence,"

eng, *Gastrointestinal Endoscopy*, vol. 71, no. 2, pp. 319–324, Feb. 2010, ISSN: 1097-6779. DOI: 10/d43r8s.

[14] L. Wintzer-Wehekind, L. Moulis, M. Camus, *et al.*, "Prospective assessment of learning curve and impact of intensive versus progressive training in colonoscopy competence among French residents," *BMC Medical Education*, vol. 25, no. 1, p. 367, Mar. 2025, ISSN: 1472-6920. DOI: 10.1186/s12909-025-06924-2. [Online]. Available: https://doi.org/10.1186/s12909-025-06924-2.

[15] F. Van Wifferen, L. De Jonge, J. Worthington, *et al.*, "Prioritisation of colonoscopy services in colorectal cancer screening programmes to minimise impact of COVID-19 pandemic on predicted cancer burden: A comparative modelling study," en, *Journal of Medical Screening*, vol. 29, no. 2, pp. 72–83, Jun. 2022, ISSN: 0969-1413, 1475-5793. DOI: 10.1177/09691413211056777. [Online]. Available: https://journals.sagepub.com/doi/10.1177/09691413211056777.

[16] N. Kenters, E. Tartari, J. Hopman, *et al.*, "Worldwide practices on flexible endoscope reprocessing," en, *Antimicrobial Resistance and Infection Control*, vol. 7, p. 153, Dec. 2018. DOI: 10.1186/s13756-018-0446-6. [Online]. Available: https://pmc.ncbi.nlm.nih.gov/articles/PMC6296091/.

[17] C. L. Ofstead, H. P. Wetzler, O. L. Heymann, E. A. Johnson, J. E. Eiland, and M. J. Shaw, "Longitudinal assessment of reprocessing effectiveness for colonoscopes and gastroscopes: Results of visual inspections, biochemical markers, and microbial cultures," eng, *American Journal of Infection Control*, vol. 45, no. 2, e26–e33, Feb. 2017, ISSN: 1527-3296. DOI: 10/f9x4sr.

[18] S. Larsen, A. Kalloo, and S. Hutfless, "The hidden cost of colonoscopy including cost of reprocessing and infection rate: The implications for disposable colonoscopes," en, *Gut*, vol. 69, no. 2, pp. 197–200, Feb. 2020, ISSN: 0017-5749, 1468-3288. DOI: 10/gm79vr. [Online]. Available: https://gut.bmj.com/content/69/2/197.

[19] G. Iddan, G. Meron, A. Glukhovsky, and P. Swain, "Wireless capsule endoscopy," en, *Nature*, vol. 405, no. 6785, pp. 417–417, May 2000, ISSN: 1476-4687. DOI:

10.1038/35013140. [Online]. Available: https://www.nature.com/articles/35013140.

[20] S. H. Kim and H. J. Chun, "Capsule Endoscopy: Pitfalls and Approaches to Overcome," en, *Diagnostics*, vol. 11, no. 10, p. 1765, Oct. 2021, ISSN: 2075-4418. DOI: 10.3390/diagnostics11101765. [Online]. Available: https://www.mdpi.com/2075-4418/11/10/1765.

[21] N. Shamsudhin, V. I. Zverev, H. Keller, *et al.*, "Magnetically guided capsule endoscopy," en, *Medical Physics*, vol. 44, no. 8, e91–e111, 2017, ISSN: 2473-4209. DOI: 10/gmt4p2. [Online]. Available: https://onlinelibrary.wiley.com/doi/abs/10.1002/mp.12299.

[22] G. Ciuti, K. Skonieczna-Żydecka, W. Marlicz, *et al.*, "Frontiers of Robotic Colonoscopy: A Comprehensive Review of Robotic Colonoscopes and Technologies," en, *Journal of Clinical Medicine*, vol. 9, no. 6, p. 1648, May 2020, ISSN: 2077-0383. DOI: 10/gm258h. [Online]. Available: https://www.mdpi.com/2077-0383/9/6/1648.

[23] F. Cosentino, E. Tumino, G. R. Passoni, E. Morandi, and A. Capria, "Functional evaluation of the endotics system, a new disposable self-propelled robotic colonoscope: In vitro tests and clinical trial," eng, *The International Journal of Artificial Organs*, vol. 32, no. 8, pp. 517–527, Aug. 2009, ISSN: 0391-3988. DOI: 10/gnnpq6.

[24] L. Manfredi, E. Capoccia, G. Ciuti, and A. Cuschieri, "A Soft Pneumatic Inchworm Double balloon (SPID) for colonoscopy," en, *Scientific Reports*, vol. 9, no. 1, p. 11 109, Jul. 2019, ISSN: 2045-2322. DOI: 10.1038/s41598-019-47320-3. [Online]. Available: https://www.nature.com/articles/s41598-019-47320-3.

[25] B. Vucelic, D. Rex, R. Pulanic, *et al.*, "The aer-o-scope: Proof of concept of a pneumatic, skill-independent, self-propelling, self-navigating colonoscope," eng, *Gastroenterology*, vol. 130, no. 3, pp. 672–677, Mar. 2006, 00137 ZSCC: 0000137, ISSN: 0016-5085. DOI: 10/bvvctq.

[26] J. C. Norton, P. R. Slawinski, H. S. Lay, *et al.*, "Intelligent magnetic manipulation for gastrointestinal ultrasound," *Science Robotics*, vol. 4, no. 31, eaav7725, Jun.

2019. DOI: 10/gjpgdc. [Online]. Available: https://www.science.org/doi/10.1126/scirobotics.aav7725.

[27] M. Mattille, Q. Boehler, J. Lussi, N. Ochsenbein, U. Moehrlen, and B. J. Nelson, "Autonomous Magnetic Navigation in Endoscopic Image Mosaics," en, *Advanced Science*, vol. 11, no. 19, p. 2 400 980, 2024, ISSN: 2198-3844. DOI: 10.1002/advs.202400980. [Online]. Available: https://onlinelibrary.wiley.com/doi/abs/10.1002/advs.202400980.

[28] F. Bianchi, A. Masaracchia, A. Damone, *et al.*, "Hybrid 6-DoF Magnetic Localization for Robotic Capsule Endoscopes Compatible With High-Grade Magnetic Field Navigation," *IEEE Access*, vol. 10, pp. 4414–4430, 2022, ISSN: 2169-3536. DOI: 10.1109/ACCESS.2021.3136796. [Online]. Available: https://ieeexplore.ieee.org/document/9656131/.

[29] A. Mesot, M. Mattille, Q. Boehler, *et al.*, "Teleoperated Magnetic Endoscopy: A Case Study and Perspective," en, *Advanced Intelligent Systems*, p. 2 400 522, Aug. 2024, ISSN: 2640-4567, 2640-4567. DOI: 10.1002/aisy.202400522. [Online]. Available: https://onlinelibrary.wiley.com/doi/10.1002/aisy.202400522.

[30] J. W. Martin, B. Scaglioni, J. C. Norton, *et al.*, "Enabling the future of colonoscopy with intelligent and autonomous magnetic manipulation," en, *Nature Machine Intelligence*, vol. 2, no. 10, pp. 595–606, Oct. 2020, ISSN: 2522-5839. DOI: 10/gm79tx. [Online]. Available: https://www.nature.com/articles/s42256-020-00231-9.

[31] J. W. Martin, L. Barducci, B. Scaglioni, *et al.*, "Robotic Autonomy for Magnetic Endoscope Biopsy," *IEEE Transactions on Medical Robotics and Bionics*, vol. 4, no. 3, pp. 599–607, Aug. 2022, ISSN: 2576-3202. DOI: 10.1109/TMRB.2022.3187028.

[32] C. Lena, D. Milesi, A. Casella, *et al.*, "ENHANCED MONOCULAR DEPTH ESTIMATION FROM MOTION IN COLONOSCOPY," en, *Gastrointestinal Endoscopy*, 2024. [Online]. Available: https://www.giejournal.org/article/S0016-5107(24)00901-5/fulltext.

[33] K. Obstein, C. Landewee, J. Norton, *et al.*, "The Magnetic Flexible Endoscope: Phase 1 First-In-Human Trial," *Gastrointestinal Endoscopy*, 2024 DDW Abstract

Issue, vol. 99, no. 6, Supplement, AB581, Jun. 2024, ISSN: 0016-5107. DOI: 10.1016/j.gie.2024.04.2659. [Online]. Available: https://www.sciencedirect.com/science/article/pii/S0016510724029183.

[34] G. Cummins, B. F. Cox, G. Ciuti, *et al.*, "Gastrointestinal diagnosis using non-white light imaging capsule endoscopy," en, *Nature Reviews Gastroenterology & Hepatology*, vol. 16, no. 7, pp. 429–447, Jul. 2019, ISSN: 1759-5053. DOI: 10/gnj458. [Online]. Available: https://www.nature.com/articles/s41575-019-0140-z.

[35] *ExactVu™ Micro-Ultrasound System - Exact Imaging.* [Online]. Available: https://www.exactimaging.com/exactvu-micro-ultrasound-system.

[36] N. J. Greenidge, B. Calmé, A. C. Moldovan, *et al.*, "Harnessing the oloid shape in magnetically driven robots to enable high-resolution ultrasound imaging," *Science Robotics*, vol. 10, no. 100, eadq4198, Mar. 2025. DOI: 10.1126/scirobotics.adq4198. [Online]. Available: https://www.science.org/doi/10.1126/scirobotics.adq4198.

[37] N. G. Kim, N. J. Greenidge, J. Davy, *et al.*, "External Steering of Vine Robots via Magnetic Actuation," *Soft Robotics*, Sep. 2024, ISSN: 2169-5172. DOI: 10.1089/soro.2023.0182. [Online]. Available: https://www.liebertpub.com/doi/abs/10.1089/soro.2023.0182.

Chapter 2

Developable Roller Shaped Endoscopes for Roll Recovery

2.1 Abstract

Magnetic manipulation has been adopted as a method of actuation in both wireless capsule endoscopy and soft-tethered endoscopy, with the goal of improving gastrointestinal procedures. However, by nature of magnetic manipulation, these endoscopes are typically limited to a maximum of five Degrees of Freedom (DoF). With the need to introduce additional contact-based sensing modalities for subsurface investigation into these systems as well as to improve overall dexterity, it is both practically and clinically beneficial to recover the lost DoF, i.e., the roll around the main axis. This paper presents a method of achieving the magnetic manipulation of an underactuated device by leveraging developable surfaces, specifically, the oloid shape. The design of a clinically relevant magnetic

endoscope with all its ancillary elements, as well as contact sensors, is proposed and demonstrated in vivo. The contact sensor data from the in vivo experiments show that for sweeping motions over 100° of roll, contact between the endoscope's sensor region and the colon wall can be maintained for 74% of the motion.

2.2 Introduction

GI cancers, particularly in the colon, stomach, and esophagus, account for 18.7% of new cancer cases and 22.6% of cancer-related deaths globally [1]. These slow-progressing diseases have a prolonged asymptomatic phase [2], making early detection through screening essential. Conventional flexible endoscopy (FE) is the gold standard for visualization, but its push-driven mechanism often causes pain, requires sedation, and risks perforation. Key clinical challenges include improving patient comfort, enhancing adenoma detection, and expanding diagnostic and therapeutic capabilities [3].

Capsule endoscopy, first introduced as an ingestible pill-sized camera [4], has since evolved into actively manipulated tethered and untethered systems. Magnetic actuation has demonstrated 5-DoFs control in both categories [5]–[7], enabling front-driven propulsion with reduced patient discomfort and lower procedural risks. Additionally, real-time localization and automation [8] can ease operator workload and reduce training time.

Magnetic manipulation relies on external fields to generate forces and torques on an embedded magnetic element. The commonly used magnetic dipole model describes this interaction, where the device aligns with the field to minimize potential energy. A fundamental limitation of this approach is the inability to induce torque around the magnetization axis (see "Lost DoF" in Figure 2.1), restricting full dexterity. This affects precise tool positioning for biopsy and therapy, as well as the integration of advanced sensing modalities.

Previous work using the Magnetic Flexible Endoscope (MFE) [9] demonstrated microUS imaging within the GI tract but remained constrained by 5-DoF control, limiting image acquisition quality. Solutions such as mechanically rotating transducers [10], [11] add me-

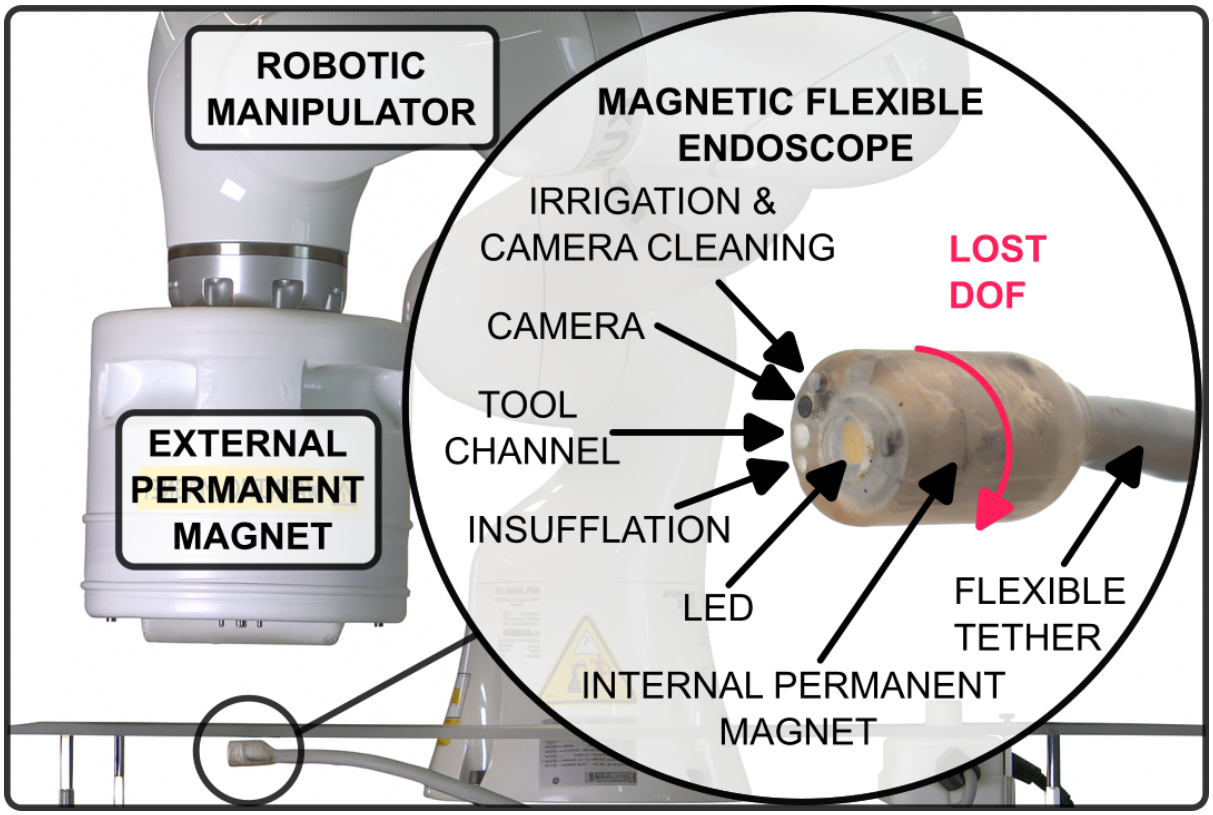

Figure 2.1: **Overview of the MFE system:** Illustration of the "lost DoF" in magnetic manipulation and key elements.

chanical complexity without addressing overall dexterity. Meanwhile, standard FE has reported adenoma miss rates up to 30% [12], particularly for flat or right-sided lesions. While enhanced optical techniques such as Narrowband Imaging (NBI) and chromoendoscopy [13] improve mucosal visualization, subsurface imaging methods like microUS [14], OCT[15], photoacoustics [16] and Terahertz imaging [17] are necessary for in situ histological assessment.

Recovering roll control is critical before integrating additional sensing modalities. This work explores a novel underactuated approach that exploits endoscope-tissue interactions to restore roll motion using only external magnetic actuation. By leveraging differential geometric principles, we introduce a developable roller design, where controlled pitching and yawing induce continuous roll motion. This method maintains low power consumption, lightweight design, and reduced mechanical complexity while improving diagnostic and therapeutic precision.

2.3 Methods

2.3.1 Choosing the Right Developable Roller

Most developable rollers are characterized by their ability to develop their entire surface while rolling and possess the property of keeping their center of mass at a constant height. The oloid has some unique characteristics which set it apart from the rest of its developable roller family, but, it is most closely related to the sphericon as both can be generated by calculating the convex hull of circular arcs (as shown in Figure 2.2). A side-by-side geometric comparison of the sphericon and the oloid is summarized in Table 2.1.

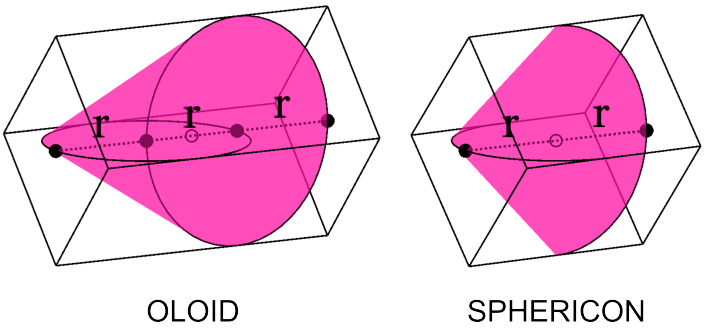

Figure 2.2: Convex hull and bounding box of the Oloid (left) and the sphericon (right) where r is the radius of the forming circles.

Table 2.1: Properties of the Oloid and the Sphericon

Property	**Oloid**	**Sphericon**
Angle of inclination	30°	45°
Length of generator	$\sqrt{3}r$	$\sqrt{2}r$
Number of vertices	0	4
Number of edges	2	2
Internal volume	$3.0524r^3$	$2.0943r^3$
Cross-section	$2r^2$	$2r^2$
Length	$3r$	$2r$
Overall volume	$5.9921r^3$	$3.9921r^3$
Volume ratio	0.509	0.525

For scopes used in the GI tract, the limiting dimensions are those of the cross-section across the transverse plane as this determines ease and therefore comfort of insertion and

manipulation. Due to the long tubular form factor of the majority of the tract, endoscopes can acceptably have rigid lengths of up to 30 mm for upper GI and 60 mm for lower GI [18] to be considered a clinically relavant size. This means that for the same cross-sectional dimensions (r), the oloid shape provides more space for internal components, especially those with cylindrical form factor. One other unique feature of the oloid is that it has zero vertices compared to the 4 of the sphericon which means that in applications where sharp edges are to be avoided in order to reduce damage to tissue, the oloid is favorable. For these reasons the oloid was chosen as the developable roller for this demonstration of roll recovery in magnetic endoscopes.

2.3.2 Geometrical Description of the Oloid

The meandering motion of the oloid, shown in Figure 2.3 demonstrates the coupling of pitch and yaw movement with its movement in the roll direction. This way, in a system where roll is not controllable independently, the roll can be controlled by adjusting the magnetic moment along the pitch and yaw directions.

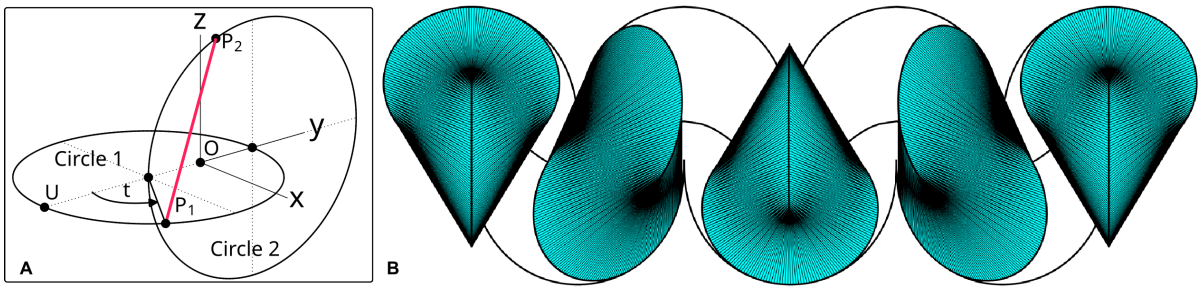

Figure 2.3: **The oloid:** (**A**) Geometric representation with generator line in red and (**B**) Rolling motion with generator lines shown in black. Adapted from [19].

The oloid is a 3D shape defined by generator lines that connect two identical, perpendicular circles [19] as shown in Figure 2.3. These generator lines serve as fundamental structural elements, creating the oloid's surface. The shape is discretized along an arc length parameter, t, where each value of t corresponds to a unique point on circle 1 (P_1), and a corresponding point on circle 2 (P_2). The generator line is formed by connecting corresponding points P_1 and P_2. To fully define the oloid, the arc length parameter t is constrained to the range $\frac{2\pi}{3} \leq t \leq \frac{2\pi}{3}$ for both circles. As the oloid rolls on a horizontal

surface, each generator line sequentially makes contact with the surface, ensuring smooth motion. The line in contact at any given moment dictates the pose of the oloid, meaning that the existence of a generator line directly impacts the achievable range of motion.

To quantify how closely a shape adheres to the geometrical properties of a full oloid, we defined a term "oloidicity". This was determined by the range of t values and the completeness of the generator lines.

We define the completeness of generator lines by a function $g(t)$, where:

$$g(t) = \frac{\text{Length of generator line at t}}{r\sqrt{3}} \tag{2.1}$$

For a full oloid, $g(t) = 1$ for all t, whereas for partial oloids, $0 \leq g(t) < 1$. The oloidicity metric is therefore given by:

$$\text{Oloidicity} = \frac{\int_{-2\pi/3}^{2\pi/3} \int_{-2\pi/3}^{2\pi/3} g(t_1, t_2) dt_1 dt_2}{(4\pi/3)^2} \tag{2.2}$$

This integral normalizes generator line completeness over the surface area, providing a quantitative measure of oloidicity across different hybridized shapes. A full oloid is achieved when t spans the full range for both circles, while a partial oloid has a reduced range, limiting its contact points with the rolling surface.

2.3.3 Magnetic Manipulation System

While this approach can be applied to a wide range of devices that are manipulated by magnetic fields (including wireless capsule endoscopes), we adopt the MFE platform from previous work by [9] and [8] to prove the principle of operation.

The MFE platform (Figure 2.1) is a robotically controlled magnetic endoscope system comprised of a KUKA LBR, 7- DoF robotic manipulator which has a large cylindrical External Permanent Magnet (EPM) mounted as the end effector, a tethered magnetic endoscope with an embedded Internal Permanent Magnet (IPM) and a real-time endoscope

localization system.

The magnetic manipulation of the MFE is achieved by adjusting the pose of the EPM in 6 DoF which imparts magnetic force and torques onto the IPM allowing for the MFE to be pulled and steered through the GI tract in 5- DoF. On-board sensors and a complex localization algorithm [20] are used to obtain 6- DoF real-time pose feedback of the MFE in order to attain effective control. This enables the user to successfully navigate the GI tract with the endoscope using just a joystick as an input.

2.3.4 Magnetic Field Control

The magnetic field control method presented here utilizes the dipole-dipole model and is based on [8], [9], [20] where full derivations can be found.

The dipole moments of the EPM and the IPM are denoted as $\mathbf{m_E} \in \mathbb{R}^3$ and $\mathbf{m_I} \in \mathbb{R}^3$ respectively, and their positions as $\mathbf{p_E} \in \mathbb{R}^3$ and $\mathbf{p_I} \in \mathbb{R}^3$. All points and vectors are represented in the global frame.

The input to this portion of the control is a desired rotation matrix of the IPM which is converted into a vector representing the desired IPM heading, $\hat{\mathbf{m}}_{\mathbf{I_d}}$. From the desired IPM heading, the required torque can be calculated based on the heading error $(\hat{\mathbf{m}}_{\mathbf{I}} \times \hat{\mathbf{m}}_{\mathbf{I_d}})$ where the magnitude is the angle between the two vectors.

Given a magnetic field $\mathbf{B_E}$ generated by the EPM, Maxwell's force and torque equations can be rewritten to represent the magnetic force $\mathbf{f}$ and torque $\boldsymbol{\tau}$ on the IPM.

$$\mathbf{f} = (\mathbf{m_I} \cdot \nabla)\mathbf{B_E} \tag{2.3}$$

$$\boldsymbol{\tau} = \mathbf{m_I} \times \mathbf{B_E} \tag{2.4}$$

The robot arm is controlled in joint space and has generalized coordinates denoted by $\mathbf{q} \in \mathbb{R}^7$. The relationship between the twist of the EPM which is mounted as the robot's

end effector and the robot's joint velocities can be linearized using the robot's geometric Jacobian $J_R(\mathbf{q}) \in \mathbb{R}^{6\times7}$ as follows:

$$\begin{bmatrix} \dot{\mathbf{p}}_\mathbf{E} \\ \boldsymbol{\omega}_\mathbf{E} \end{bmatrix} = J_R(\mathbf{q})\,\dot{\mathbf{q}} \tag{2.5}$$

Due to the magnetic symmetry explained, we know that any rotation in $\boldsymbol{\omega}_\mathbf{E}$ along the EPM's magnetization axis will not affect the EPM's dipole moment $\hat{\mathbf{m}}_\mathbf{E}$ and therefore we can define the EPM's Jacobian, $J_E(\mathbf{q})$ as:

$$\begin{bmatrix} \dot{\mathbf{p}}_\mathbf{E} \\ \dot{\hat{\mathbf{m}}}_\mathbf{E} \end{bmatrix} = \begin{bmatrix} \mathbb{I}_3 & \mathbb{O}_3 \\ \mathbb{O}_3 & S(\hat{\mathbf{m}}_\mathbf{E})^T \end{bmatrix} J_R(\mathbf{q})\,\dot{\mathbf{q}} = J_E(\mathbf{q})\,\dot{\mathbf{q}} \tag{2.6}$$

where $\mathbb{I}_3$ is a 3x3 Identity matrix, $\mathbb{O}_3$ is a 3x3 zero matrix and $S()$ is the skew-symmetric form of the cross-product compensating for the symmetries in the magnetic field.

The linearized form of the dipole-dipole model is therefore:

$$\begin{bmatrix} \dot{\mathbf{f}} \\ \dot{\boldsymbol{\tau}} \end{bmatrix} = \begin{bmatrix} \frac{\partial \mathbf{F_m}}{\partial \mathbf{p}} & \frac{\partial \mathbf{F_m}}{\partial \widehat{m}_\mathbb{E}} & \frac{\partial \mathbf{F_m}}{\partial \widetilde{m}_\mathbf{I}} \\ \frac{\partial \tau_\mathbf{m}}{\partial \mathbf{p}} & \frac{\partial \tau_\mathbf{m}}{\partial \mathrm{m}_\mathbf{E}} & \frac{\partial \tau_\mathrm{m}}{\partial \mathrm{m}_\mathbf{I}} \end{bmatrix} \begin{bmatrix} \dot{\mathbf{p}} \\ \dot{\hat{\mathbf{m}}}_\mathbf{E} \\ \dot{\hat{\mathbf{m}}}_\mathbf{I} \end{bmatrix} \tag{2.7}$$

$$= J_f(\mathbf{p}, \mathbf{m_E}, \mathbf{m_I}) \begin{bmatrix} \dot{\mathbf{p}} \\ \dot{\hat{\mathbf{m}}}_\mathbf{E} \\ \dot{\hat{\mathbf{m}}}_\mathbf{I} \end{bmatrix} \tag{2.8}$$

where $\mathbf{p} = \mathbf{p_I} - \mathbf{p_E}$

Assuming the pose of the IPM remains constant, Equation 2.7 can be reduced to:

$$\begin{bmatrix} \dot{\mathbf{f}} \\ \dot{\boldsymbol{\tau}} \end{bmatrix} = J_f(\mathbf{p}, \mathbf{m_E}, \mathbf{m_I}) \begin{bmatrix} \dot{\mathbf{p}}_E \\ \dot{\hat{\mathbf{m}}}_\mathbf{E} \end{bmatrix} \tag{2.9}$$

The Jacobian J_f is computed at every time step to ensure that the local linearization of the dipole-dipole model and the constant IPM pose remain locally valid assumptions.

The overall control function can be defined as follows:

$$\begin{bmatrix} \dot{\mathbf{p}}_E \\ \dot{\hat{\mathbf{m}}}_{\mathbf{E}} \end{bmatrix} = J_f^{\dagger} \boldsymbol{pid} \left(\begin{bmatrix} \dot{\mathbf{f}} \\ \dot{\boldsymbol{\tau}} \end{bmatrix} \right) \tag{2.10}$$

The computation of the pseudoinverse of the Jacobian, $J_f^{\dagger}$ is then carried out by means of weighted/damped least squares algorithm shown in [8]. The angular and linear motions of the EPM are then transformed into desired changes in robot joint angles $\dot{\boldsymbol{q}} \in \mathbb{R}^7$ using the following:

$$\dot{\mathbf{q}} = J_f^{\dagger} \mathbf{W_a} \begin{bmatrix} \dot{\mathbf{p}}_{\mathbf{E}} \\ \dot{\hat{\mathbf{m}}}_{\mathbf{E}} \end{bmatrix} \tag{2.11}$$

Where $\mathbf{J}^{\dagger} \in \mathbb{R}^{7\times6}$ is the pseudoinverse of the robot's Jacobian, $\mathbf{W_a} \in \mathbb{R}^{6\times6}$ is a suitable weighting matrix.

The desired changes in joint angles are fed to the robot controller for the robot to calculate the required inverse kinematics and to perform the necessary motion.

2.3.5 Integration into a Robotic Colonoscopy Platform and Preclinical Evaluation

To accommodate the ancillary components of a magnetic endoscope, a full oloid would need to be scaled beyond a clinically relevant size. In contrast, a cylinder is optimal for component integration but lacks controllable roll. Consequently, the functional areas of the oloid were evaluated to facilitate the development of a hybrid design.

The endoscope had to be comparable in size to other magnetically manipulated endoscopes, such as the cylindrical MFE endoscope, which measures $20 \times 20 \times 40$ mm [21]. It had to also incorporate magnetic manipulation and localization capabilities, requiring a magnet core and a localization system. Additionally, the design had to support White

Light Imaging (WLI) and essential endoscopic functions, including insufflation, irrigation, and camera cleaning (see Figure 2.1. Safety considerations included smooth edges to prevent damage to the colon wall and waterproofing to protect internal components. The endoscope also had to be sensor-agnostic, to allow compatibility with various submucosal visualization sensors. Finally, the design had to achieve a minimum range of motion of $\pm 25^\circ$ in roll, yaw, and pitch.

2.3.6 Endoscope Shape Optimization

To compare component integration across designs, we scaled each design to fit within a $20 \times 20 \times 40$ mm bounding box and used a dimensionless volume ratio, which represents the shape's volume relative to the volume of the bounding box (green box in Figure 2.4).

Figure 2.4 illustrates a sample of the designs considered and the trade-offs made to achieve a hybrid design that meets the design requirements.

The full oloid design provided the largest roll range but had the lowest volume ratio of 0.50. In contrast, the cylindrical design achieved the highest volume ratio of 0.79, indicating that the full oloid endoscope would need to be approximately 1.6 times larger than the cylinder to achieve the same internal volume. By limiting the controllable roll range to 180°, the half oloid design improved the volume ratio to 0.53. This was further increased to 0.63 by the hybrid (oloid and cylinder) design while maintaining the controllable roll range of the half oloid design. Since the internal components to be integrated into the endoscope are primarily cylindrical, the size of the largest internal cylinder that could fit within each design was an important consideration. To accommodate a given cylindrical component, the full oloid, half oloid, and hybrid designs would need to be approximately 10, 5, and 3 times larger, respectively, than the cylinder.

When comparing the half oloid design to the hybrid design, although the number of generator lines remained the same, some were reduced in length to produce a smaller overall cross-section. This modification is reflected in the oloidicity values. The hybrid design was selected overall because it was the closest to the cylinder in terms of cross-

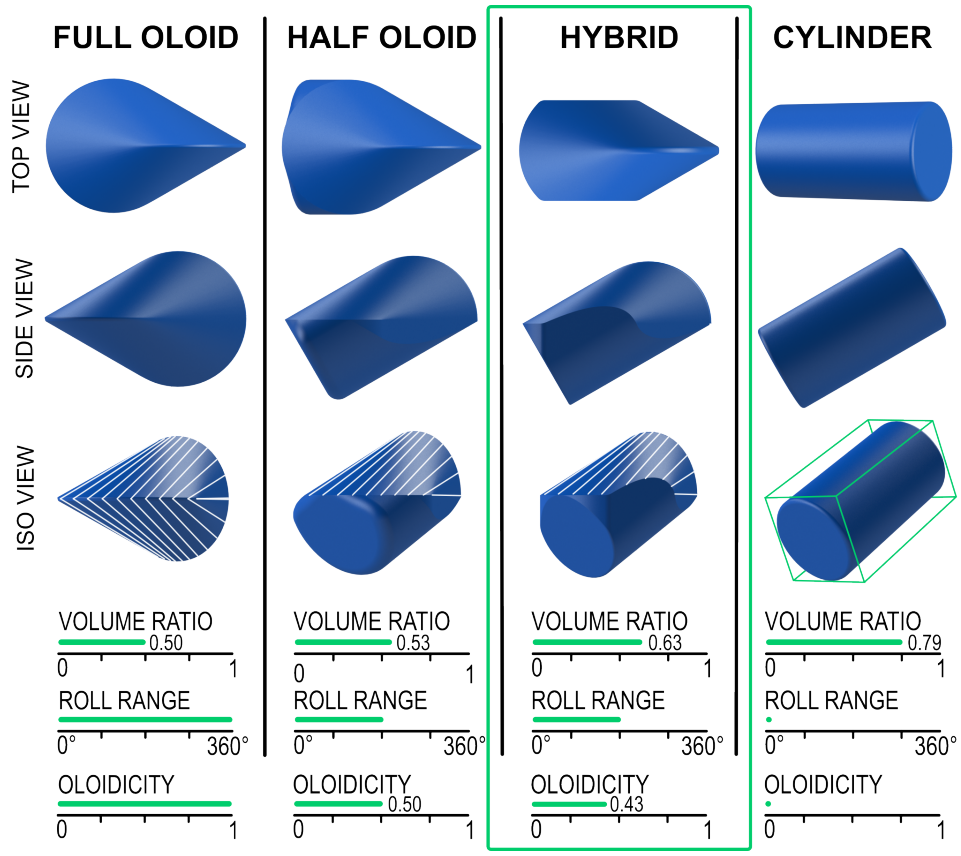

Figure 2.4: **Summary table for hybrid oloid-cylinder endoscope designs**: oloid generator lines are shown in white in iso view. Volume ratio, roll range and oloidicity are defined in the text.

section and volume ratio while maintaining a sufficient roll range to achieve the desired sweeping motions. In this case, the design constraints significantly limited the parameter space, making formal optimization unnecessary; however, as a fully defined mathematical concept, the shape could readily be optimized.

2.3.7 Contact Sensors

Our vision is to use this device for submucosal visualization, such sensors usually rely on constant contact with the tissue. Therefore, here we integrated a multi-point contact sensor to evaluate and characterize our approach. On its upper centerline, the endoscope provides the largest and flattest area (shown in Figure 2.5(A)). This area provides the best conditions for the integration of this sensing modality. To provide in situ information on contact of this surface, contact sensors were integrated into a 4 x 10 mm^2 area in this location. The sensor is based on capacitive measurement using eight electrodes

distributed in a 2 x 4 pattern over this area. Capacitive sensing allows for very thin electrodes with low volume profile. The electrodes are manufactured as flexible printed circuit board of 10 mm width, 0.1 mm thickness and 26 mm length, including solder pads inside the endoscope (Figure 2.5(B)). The sensor's transducers and processing unit were implemented at the distal part of the system at the robot's base. The electrode array was placed in a notch prepared for the sensor and aligned using a mounting hole on the Printed Circuit Board (PCB). The sensor system is based on the method presented in [22]. Sensor values were published to the robot's robot operating system (ROS) network. The sensor array was split into four quarters; the combined readings from the electrode provide binary information of contact for each quarter section at a rate of 50 Hz.

2.3.8 Endoscope Manufacture

The 3D endoscope shell was printed in resin on the Form3 3D printer (FormLabs) in three parts, the top half, the bottom right and the bottom left shown in Figure 2.5(C). The magnet core, camera, Irrigation, and Camera Cleaning (ICC), and insufflation tubes were carefully inserted into their positions before sealing the two bottom halves together.

The endoscope was designed to be sensor-agnostic, with an interchangeable or "hot swappable" feature so that a singular base could form the test bed for multiple sensor types and designs. This was done to reduce waste, but may have utility in the clinical setting, where the user can have the option to swap between sensor types in the middle of a procedure.

For this reason, the bottom half had to be fully encapsulated for waterproofing. This was done by creating small ventilation holes in the endoscope's shell before filling all the gaps with high viscosity cyanoacrylate (Permabond 4c40). By doing this, the mechanical connection between the two halves does not have to be watertight, significantly reducing the complexity of this portion of the design. The mechanical connection between the two halves leverages the 3D printed structure with an integrated clip mechanism on the side of the endoscope (shown in Figure 2.5(C)) which is easy to clip on and off, but secure

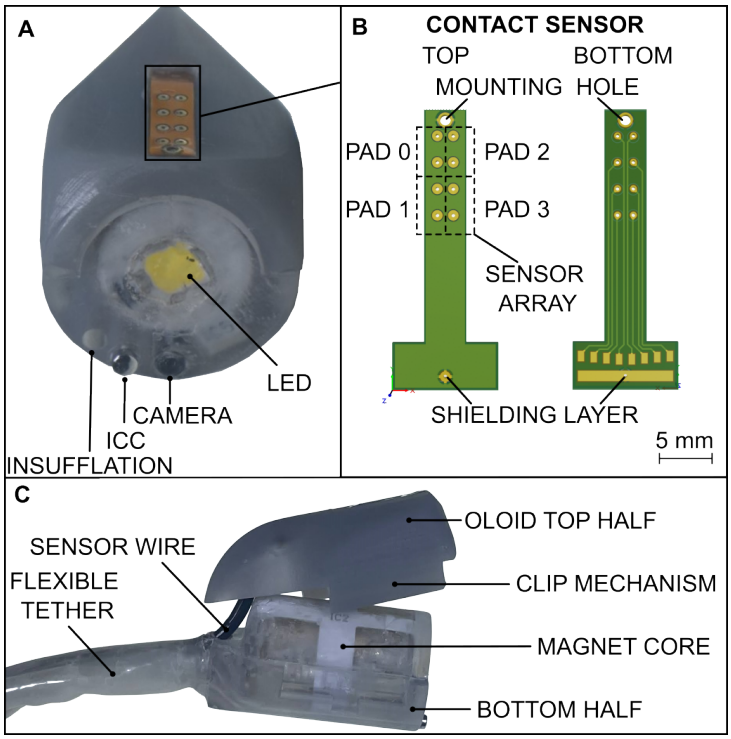

Figure 2.5: **Oloid Magnetic Endoscope (OME)**: **(A)** Front view of OME showing the camera, LED, ICC and insufflation, **(B)** Top and bottom view of the contact sensor PCB and **(C)** Side view of OME showing the clip mechanism and magnet core with top half unclipped.

enough to stay on during use. The sensor wire for the contact sensors was fed through a channel in the tether using a biopsy tool as shown in Figure 2.5(C).

The resulting Oloid-shaped Magnetic Endoscope (OME) design shown in Figure 2.5 meets all the design requirements set out in at the beginning of this section and has overall dimensions of 20 x 20 x 35 mm.

2.4 Results and Discussion

2.4.1 In Vivo Demonstration of Sweeping and Rolling Motions

With an endoscope that fulfilled all the necessary design criteria, in vivo experiments were carried out to showcase the system's potential for clinical use. A porcine model was selected for these tests due to the significant similarity between a pig's gastrointestinal anatomy and that of a human.

The experiments were carried out on a 39 kg large white female pig under general anesthesia, following this procedure. These trials were authorized by the home office (UK) under license (procedure project license: PF5151DAF) and complied with the animal (scientific procedures) act 1986.

After thoroughly cleansing the colon with several enemas, the OME was inserted through the rectum and advanced approximately 20 cm into the colon. This length offered a long, straight section of the bowel suitable for experimentation. The OME's auxiliary components were employed for colon distension and irrigation as needed.

The primary goals of these trials were to prove that the OME could successfully roll in vivo and execute clinically relevant motions for contact-based sensing (Supplementary Video). To validate this, two experiments were devised. The first involved a sweeping motion over the upper half of the colon surface (Figure 2.6(A)), while the second focused on a pure rolling motion within a $\pm 50^\circ$ range (Figure 2.6(B)). Each experiment was conducted five times. These motions were performed using open-loop joy-stick control. To provide proof of contact, the visual evidence was backed up with the contact-sensing data, which monitored contact with the colon wall throughout the experiments.

Figure 2.6 shows the sweeping and rolling motions along with the contact data processed as binary measurements of contact/no-contact and the OME's orientation data. A range of 100° roll was achieved during the sweeping motion. Contact data was analyzed over 2 repetitions, showing that contact was maintained on all pads 74% of the time, with mean contact on individual pads being 92%. To analyze what subsections of the potential sensor head area remain in contact during roll motion, combined contact of two pads was analyzed. Figure 2.7 shows the matrix of contact data over the sweeping motion for all contact pads. The strongest correlation was seen on the pads 0 and 1 (left side) and the weakest on pads 0 and 3. Thus, maintaining the top-left to bottom right diagonal in contact seems to be most difficult. However, we believe that these results can be improved if the contact data is used in the feedback control loop for the OME and a properly integrated sensor head will cover less than the tested surface.

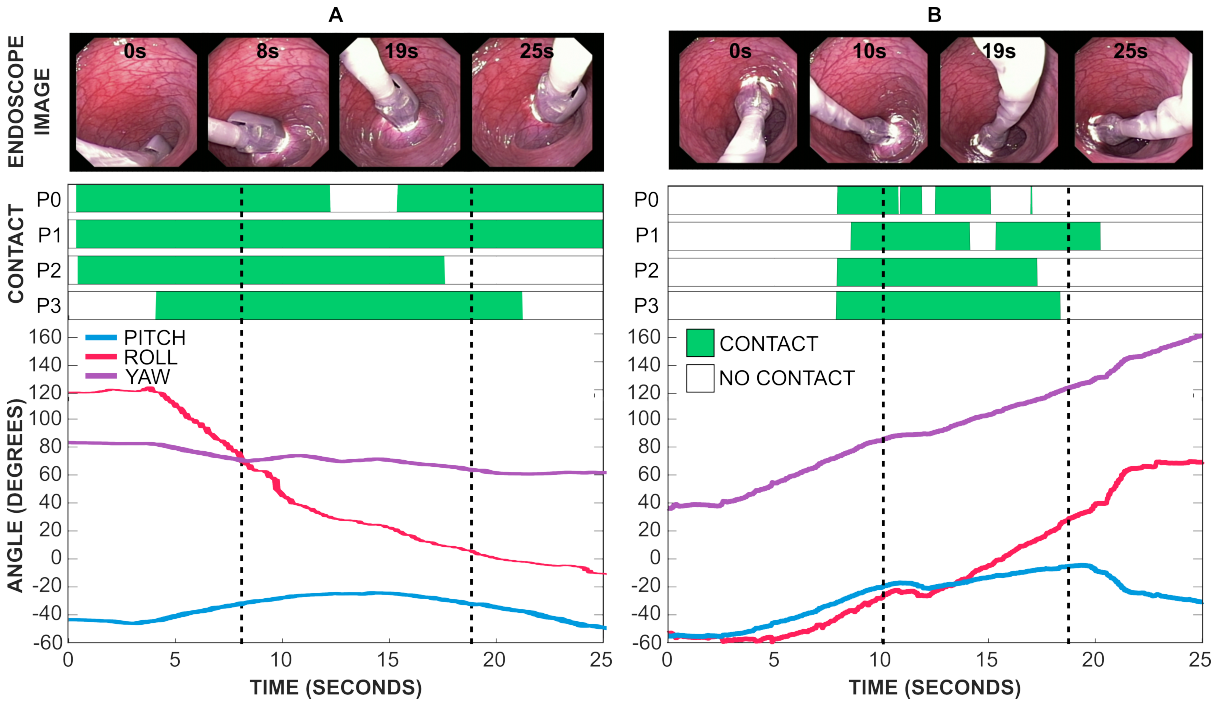

Figure 2.6: **In vivo OME results**: Contact sensor data plotted over time with orientation data from the endoscope's localization and selected scenes from the standard endoscopes video stream and OME orientation data during a **(A)** sweeping and **(B)** rolling motion in vivo.

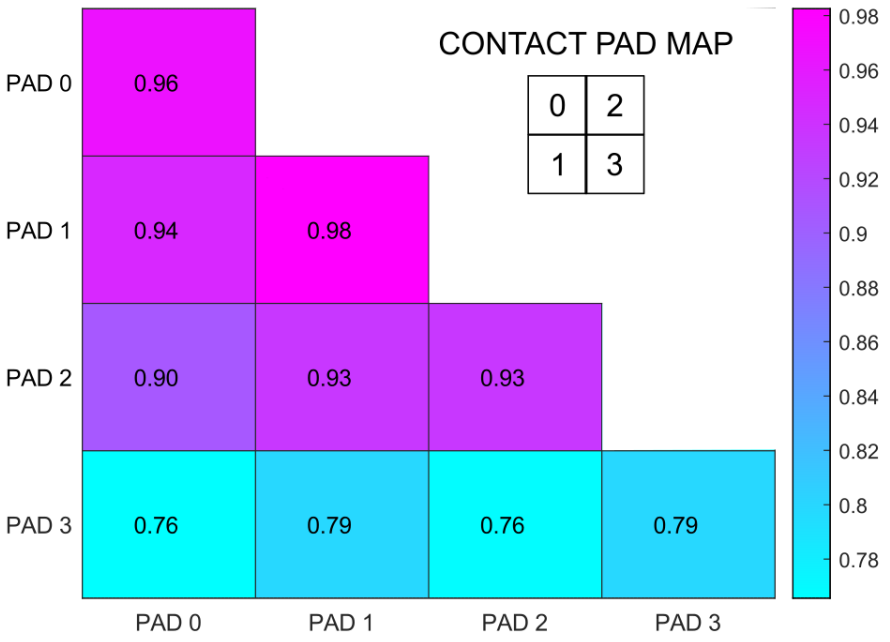

Figure 2.7: **Sweep motion in vivo contact data**: Average contact data for all four contact pads during in vivo sweeping motions over a 100° roll range.

2.5 Conclusion

In this work we were able to present a design using the oloid shape that met all the design requirements of an endoscope and perform sweeping motions whilst maintaining a contact area of 4mm x 10mm area throughout 74% of the motion.

With this, we can say that the use of the oloid shape as a roll recovery method was successful. This method of roll recovery presents a novel way to improve position control, scope stabilization, and surface scanning to magnetically manipulated endoscopes without requiring additional power and is therefore applicable to both tethered and untethered applications. The oloid shape can be scaled up or down to allow this method to be applied to a range of applications.

Future work will look at integrating submucosal visualization sensors such as ultrasound and Terahertz sensors in the pursuit of 'virtual biopsy' and to include this data in the feedback control in order to achieve higher contact percentages. Another avenue to explore would be developing more advanced control algorithms for roll control to enable complex procedures such as endoscopic submucosal dissection (ESD).

References

[1] Yue Xi and Pengfei Xu, "Global colorectal cancer burden in 2020 and projections to 2040," *Translational Oncology*, 2021. DOI: 10.1016/j.tranon.2021.101174.

[2] C.-K. Yeung, J. L. Cheung, and B. Sreedhar, "Emerging next-generation robotic colonoscopy systems towards painless colonoscopy," en, *Journal of Digestive Diseases*, vol. 20, no. 4, pp. 196–205, 2019, ISSN: 1751-2980. DOI: 10/gm78tw.

[3] J. W. Rey, R. Kiesslich, and A. Hoffman, "New aspects of modern endoscopy," *World Journal of Gastrointestinal Endoscopy*, vol. 6, no. 8, pp. 334–344, Aug. 2014, ISSN: 1948-5190. DOI: 10.4253/wjge.v6.i8.334. [Online]. Available: https://www.ncbi.nlm.nih.gov/pmc/articles/PMC4133412/.

[4] G. Iddan, G. Meron, A. Glukhovsky, and P. Swain, "Wireless capsule endoscopy," en, *Nature*, vol. 405, no. 6785, pp. 417–417, May 2000, ISSN: 1476-4687. DOI: 10.1038/35013140. [Online]. Available: https://www.nature.com/articles/35013140.

[5] N. Shamsudhin, V. I. Zverev, H. Keller, *et al.*, "Magnetically guided capsule endoscopy," en, *Medical Physics*, vol. 44, no. 8, e91–e111, 2017, ISSN: 2473-4209. DOI: 10/gmt4p2. [Online]. Available: https://onlinelibrary.wiley.com/doi/abs/10.1002/mp.12299.

[6] S. Nouda, K. Ota, and K. Higuchi, "Retrograde colon capsule endoscopy with the self-propelling capsule endoscope: The first human trial (with videos)," en, *Digestive Endoscopy*, vol. 30, no. 1, pp. 117–118, 2018, ISSN: 1443-1661. DOI: 10.1111/den.12969. [Online]. Available: https://onlinelibrary.wiley.com/doi/abs/10.1111/den.12969.

[7] A. Mahoney and J. J. Abbott, "Generating Rotating Magnetic Fields With a Single Permanent Magnet for Propulsion of Untethered Magnetic Devices in a Lumen," *IEEE Transactions on Robotics*, 2014. DOI: 10/ghfgp6.

[8] J. W. Martin, B. Scaglioni, J. C. Norton, *et al.*, "Enabling the future of colonoscopy with intelligent and autonomous magnetic manipulation," en, *Nature Machine Intelligence*, vol. 2, no. 10, pp. 595–606, Oct. 2020, ISSN: 2522-5839. DOI: 10/gm79tx. [Online]. Available: https://www.nature.com/articles/s42256-020-00231-9.

[9] J. C. Norton, P. R. Slawinski, H. S. Lay, *et al.*, "Intelligent magnetic manipulation for gastrointestinal ultrasound," *Science Robotics*, vol. 4, no. 31, eaav7725, Jun. 2019. DOI: 10/gjpgdc. [Online]. Available: https://www.science.org/doi/10.1126/scirobotics.aav7725.

[10] X. Wang, V. Seetohul, R. Chen, *et al.*, "Development of a Mechanical Scanning Device With High-Frequency Ultrasound Transducer for Ultrasonic Capsule Endoscopy," eng, *IEEE transactions on medical imaging*, vol. 36, no. 9, pp. 1922–1929, Sep. 2017, ISSN: 1558-254X. DOI: 10/gmxdk5.

[11] Y. Qiu, Y. Huang, Z. Zhang, *et al.*, "Ultrasound Capsule Endoscopy With a Mechanically Scanning Micro-ultrasound: A Porcine Study," English, *Ultrasound in Medicine and Biology*, vol. 46, no. 3, pp. 796–804, Mar. 2020, ISSN: 0301-5629, 1879-291X. DOI: 10.1016/j.ultrasmedbio.2019.12.003. [Online]. Available: https://www.umbjournal.org/article/S0301-5629(19)31623-0/fulltext.

[12] P. Wang, P. Liu, J. R. G. Brown, *et al.*, "Lower Adenoma Miss Rate of Computer-Aided Detection-Assisted Colonoscopy vs Routine White-Light Colonoscopy in a Prospective Tandem Study," English, *Gastroenterology*, vol. 159, no. 4, 1252–1261.e5, Oct. 2020, ISSN: 0016-5085, 1528-0012. DOI: 10.1053/j.gastro.2020.06.023. [Online]. Available: https://www.gastrojournal.org/article/S0016-5085(20)34820-4/fulltext.

[13] S. H. Kim and H. J. Chun, "Capsule Endoscopy: Pitfalls and Approaches to Overcome," en, *Diagnostics*, vol. 11, no. 10, p. 1765, Oct. 2021, ISSN: 2075-4418. DOI: 10.3390/diagnostics11101765. [Online]. Available: https://www.mdpi.com/2075-4418/11/10/1765.

[14] B. F. Cox, F. Stewart, H. Lay, *et al.*, "Ultrasound capsule endoscopy: Sounding out the future," en, *Annals of Translational Medicine*, vol. 5, no. 9, pp. 9–9, May 2017, ISSN: 2305-5847, 2305-5839. DOI: 10/gnj47g. [Online]. Available: https://atm.amegroups.com/article/view/14711.

[15] Y. Li, Z. Zhu, J. J. Chen, *et al.*, "Multimodal endoscopy for colorectal cancer detection by optical coherence tomography and near-infrared fluorescence imaging," *Biomedical Optics Express*, vol. 10, no. 5, pp. 2419–2429, Apr. 2019, ISSN: 2156-7085. DOI: 10.1364/BOE.10.002419. [Online]. Available: https://www.ncbi.nlm.nih.gov/pmc/articles/PMC6524571/.

[16] S. Choi, J. Kim, H. Jeon, C. Kim, and E.-Y. Park, "Advancements in photoacoustic detection techniques for biomedical imaging," en, *npj Acoustics*, vol. 1, no. 1, p. 1, Mar. 2025, Publisher: Nature Publishing Group, ISSN: 3005-141X. DOI: 10.1038/s44384-025-00005-w. [Online]. Available: https://www.nature.com/articles/s44384-025-00005-w (visited on 07/26/2025).

[17] G. Reese, C. Reid, R. Goldin, *et al.*, *Using terahertz pulsed imaging (TPI) to identify colonic pathology.* English. IEEE, 2008, ISBN: 978-1-4244-2119-0. DOI: 10.1109/ICIMW.2008.4665690. [Online]. Available: https://www.infona.pl//resource/bwmeta1.element.ieee-art-000004665690.

[18] L. Barducci, J. C. Norton, S. Sarker, *et al.*, "Fundamentals of the gut for capsule engineers," en, *Progress in Biomedical Engineering*, vol. 2, no. 4, p. 042 002, Sep. 2020, ISSN: 2516-1091. DOI: 10/gk94hm. [Online]. Available: https://doi.org/10.1088/2516-1091/abab4c.

[19] H. Dirnbock and H. Stachel, "The Development of the Oloid," *Journal for Geometry and Graphics*, vol. 1, Jan. 1997.

[20] A. Z. Taddese, P. R. Slawinski, M. Pirotta, E. De Momi, K. L. Obstein, and P. Valdastri, "Enhanced real-time pose estimation for closed-loop robotic manipulation of magnetically actuated capsule endoscopes," en, *The International Journal of Robotics Research*, vol. 37, no. 8, pp. 890–911, Jul. 2018, ISSN: 0278-3649. DOI: 10/gd5k9x. [Online]. Available: https://doi.org/10.1177/0278364918779132.

[21] N. G. Kim, N. J. Greenidge, J. Davy, *et al.*, "External Steering of Vine Robots via Magnetic Actuation," *Soft Robotics*, Sep. 2024, ISSN: 2169-5172. DOI: 10.1089/soro.2023.0182. [Online]. Available: https://www.liebertpub.com/doi/abs/10.1089/soro.2023.0182.

[22] H. Alagi, S. E. Navarro, M. Mende, and B. Hein, "A versatile and modular capacitive tactile proximity sensor," in *2016 IEEE Haptics Symposium (HAPTICS)*, Apr. 2016, pp. 290–296. DOI: 10.1109/HAPTICS.2016.7463192.

2.6 Evaluation and Summary of Findings

This chapter presented the design and experimental validation of a magnetic flexible endoscope that passively achieves rolling capability using a developable roller geometry. Rolling an endoscope around its longitudinal axis is a fundamental challenge for both standard and magnetic endoscopes, as torque applied at the shaft rarely translates effi-

ciently to the tip, especially in complex anatomy. Even in tethered magnetic systems, the inherent flexibility or lack of torsional rigidity in the soft tether impedes torque transmission. By employing the oloid, this work demonstrates a geometric solution that does not require additional actuation or onboard power and is miniaturizable for wireless applications, including capsule endoscopy.

Motivated by the need for a simple, scalable, and passive means of roll recovery to support high-quality tissue scanning, the design drew inspiration from coupled mechanical systems like the corkscrew and leveraged a shape that inherently couples pitch and yaw motions to generate rolling. A prototype OME was developed collaboratively, featuring an integrated capacitive contact sensor with four pads to provide direct, real-time tissue contact feedback developed by Karlsruhe Institute of Technology (KIT). Open-loop in vivo experimental trials directly assessed the shape's ability to maintain sweeping contact; results showed consistent tissue contact for 74% of the rolling trajectory over arcs exceeding 100°, validating the hypothesis that developable rollers can restore roll dexterity in magnetic endoscopy.

While promising, these results highlight opportunities for further advancement. The current sensor offers only coarse, binary feedback from four pads, limiting resolution and nuance in contact assessment. Future work will focus on integrating higher-resolution sensing and closed-loop sensor-based control, allowing the endoscope to adapt to anatomical variability and optimize contact performance dynamically.

Importantly, this work lays the foundation for the integration of advanced subsurface imaging and intelligent navigation. The next chapter builds directly upon these findings, introducing a closed-loop control strategy for the OME with integrated high-frequency microUS, enabling real-time virtual biopsy and detailed 3D tissue mapping. These forthcoming advancements move the field closer to fully autonomous, sensor-driven, magnetically actuated endoscopes with precision navigation and diagnostic capabilities, addressing limitations identified in this chapter and advancing the prospects for minimally invasive GI screening.

Chapter 3

Autonomous 3D Micro-ultrasound Virtual Biopsies

Chapter source: Reproduced/modified from **N. J. Greenidge**, B. Calmé, A. C. Moldovan, B. Abaravicius, J. W. Martin, N. Marahrens, J. Woolfrey, B. Scaglioni, D. S. Chathuranga, S. Mitra, S. Cochran, P. Valdastri, "Harnessing the oloid shape in magnetically driven robots to enable high-resolution ultrasound imaging", Science Robotics, vol. 10, no. 100, p. eadq4198, Mar. 2025, DOI: 10.1126/scirobotics.adq4198, AAAS [1]

All supplementary videos and supporting data can be found in `https://www.science.org/doi/10.1126/scirobotics.adq4198`, `https://www.youtube.com/playlist?list=PLWtIpCj5v7Nez_fUVWN239PC-4kG1nhsh` and `https://datadryad.org/dataset/doi:10.5061/dryad.t1g1jwtbx`.

3.1 Abstract

Magnetic fields enable remote manipulation of objects and are ideal for medical applications, as they pass through human tissue harmlessly. This capability is promising for surgical robots, allowing navigation deeper into the human anatomy and accessing organs beyond the reach of current technologies. However, magnetic manipulation is typically

limited to a maximum of two DoF orientation, restricting complex motions, especially those including rolling around the main axis of the magnetic robot. To address this challenge, we introduce a robot design inspired by embodied intelligence and the unique geometry of developable rollers, leveraging the oloid shape. The oloid, with its axial asymmetry and sinusoidal motion, facilitates rolling when precisely controlled by an external magnetic field. We present a versatile closed-loop control model to ensure precise magnetic manipulation of an oloid-shaped robot. This capability was validated in endoluminal applications through the integration of a 28 MHz microUS array to perform virtual biopsies – non-invasive real-time histological imaging. Extensive in vitro and in vivo tests using a porcine model showed the robot's ability to execute sweeping motions, identify lesions, and generate detailed 3D scans of gastrointestinal subsurface tissue. This research not only restores a critical movement capability to magnetic medical robots but also enables additional clinical applications deep within the human body.

3.2 Introduction

The application of magnetic manipulation to medical robots, such as robotic catheters [1], [2], flexible endoscopes [3]–[5], and capsule endoscopes (NaviCam® [6]), has streamlined device design by eliminating the need for complex internal actuation mechanisms [7]. This approach enables miniaturization and enhances adaptability for navigating intricate anatomical pathways within the body.

Magnetic manipulation involves the use of a controlling magnetic field source to induce a force, $\mathbf{F} \in \mathbb{R}^3(newton)$, and torque, $\tau \in \mathbb{R}^3(newton \cdot meter)$, on a magnetic object, allowing control over its position and orientation. In medical applications, where the robot is typically considerably smaller than its distance from the controlling field source, the robot behaves as a simple north-south magnetic dipole with a symmetric field around its magnetization axis (denoted by $\mathbf{X}_\mathrm{I}$ in Figure 3.1). As such, magnetic manipulation of objects is typically limited to a maximum of two degrees-of-freedom (DoFs) in orientation and three DoFs in position.

Related works [8]–[11] have explored the use of magnetic force to produce off-axis rigid body torques to control roll around the object's magnetization axis through various methods detailed in the Results section. However, these techniques, including newer soft magnet methods [12], [13], remain unsuitable in clinical applications. They have only been demonstrated in fluid environments with low force and torque demands, and on micro-scale robots controlled by electromagnetic coil systems. Furthermore, they rely on complex field-generating setups with at least eight magnetic control inputs [1], [14]–[16]. A detailed comparison of these approaches, including power consumption and workspace size, is available in Table A.1 and the Supplementary Discussion.

In terms of generating the controlling magnetic field, electromagnetic coil systems provide high control precision and adaptability, which are crucial in some applications. However, these systems typically have large physical footprints, limited workspaces, consume substantial power, require cooling, and are expensive to implement [15]–[17].

Robotically manipulated single EPM systems offer several advantages for slower, larger-scale applications such as flexible endoscopy. These systems require no energy to sustain a static magnetic field, making them energy-efficient and suitable for prolonged use. They can generate strong fields over larger workspaces while being more compact, portable, and cost-effective compared to electromagnetic coil systems [3], [18]. The MFE system enables painless [19], automated, and remote colonoscopy procedures [20] while retaining the same functionalities as standard flexible endoscopes. Although its feasibility has been validated during clinical trials [19], it has yet to demonstrate diagnostic capabilities that surpass those of standard flexible endoscopes.

At the cutting edge of GI endoscopic technology is the concept of virtual biopsies where high-fidelity diagnostic sensors are used to perform in situ histopathology. In the context of GI cancer screening, where early and accurate detection is critical [21], the ability to perform virtual biopsies could eliminate the delays, costs, and complications associated with traditional histological analysis, allowing screening, diagnosis, and therapy to occur in a single procedure [22]. A modality used alongside standard flexible endoscope is

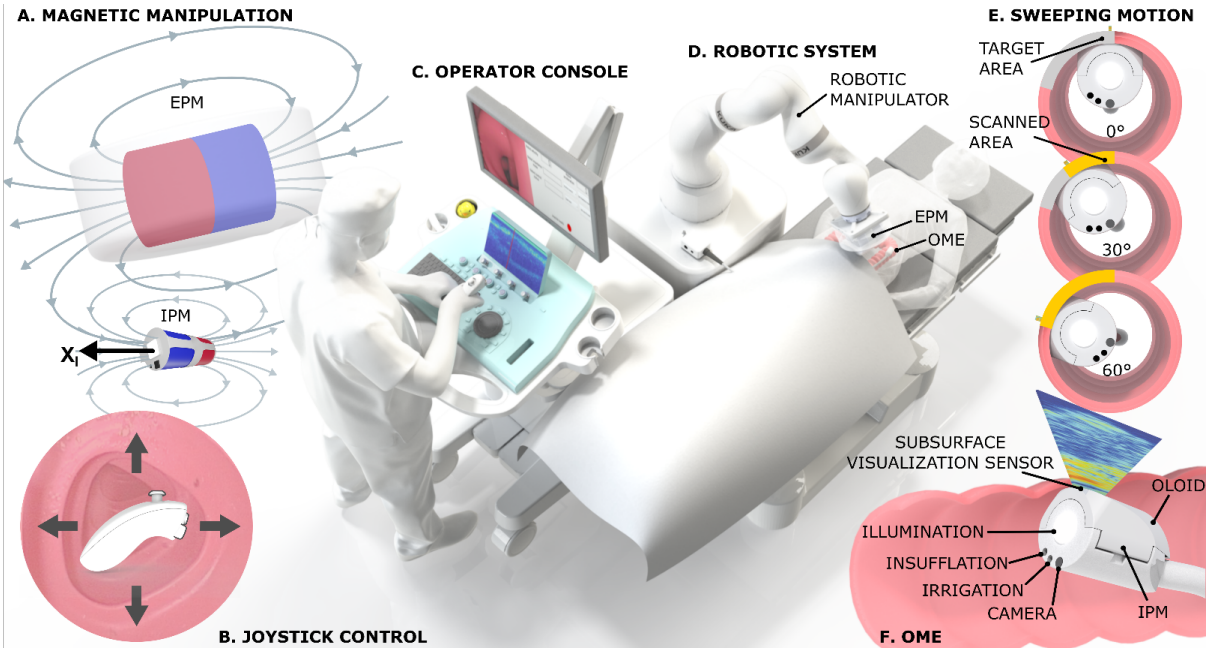

Figure 3.1: **OME for recovering a lost DoF in magnetic medical robots, enabling virtual biopsies during endoscopy.** (**A**) The magnetic manipulation system relies on the use of cylindrical permanent magnets where the field generated by the EPM pulls and orients the IPM during the procedure. The lost DoF ("roll") in magnetic manipulation around a magnet's magnetization axis ($\mathbf{X_I}$) is shown by the arrow on the IPM. (**B**) A joystick is used to control the robotic system where the operator only has to consider the desired direction based on the camera frame. (**C**) The operator console is used to visualize the camera feed for navigation and to inspect the 3D reconstructed virtual biopsies. (**D**) The robotic system, which includes a robotic manipulator, is used to manipulate the EPM and therefore the magnetic field to control the OME. (**E**) The sweeping motion is used to demonstrate the clinical viability of recovering the rolling motion for diagnostic sweeps. (**F**) The OME with the subsurface microUS visualization sensor. See Movie S1 for a visual representation of the concept overview.

OCT or high-frequency ultrasound (US), typically delivered via mini-probe endoscopic ultrasound systems like the 20 MHz UM-3R (Olympus America Inc.), that are passed through the flexible endoscope's working channel. While effective for in situ cancer staging [23], positioning these probes precisely is essential to produce artifact-free imaging [24] which can be difficult in manual manipulation. Additionally, using a microUS probe occupies the working channel, limiting its use for tasks such as margin assessment during therapeutic procedures where access to the working channel is required for other purposes. Another example of GI microUS is transrectal microUS, such as the ExactVu^{TM} probe [25] which can perform 29 MHz of the prostate and has been externally controlled robotically to create 3D microUS images [26]. However, these probes are specifically designed for

rectal imaging and cannot reach deep within the GI tract, resulting in an unmet need.

Previous research on MFEs integrated a single microUS transducer capable of capturing histologically relevant images of the colon wall [3]. However, the absence of roll control limited its ability to target specific areas, restore contact if misaligned, or perform radial sweeping motions. Designing 360° curved arrays presents substantial manufacturing challenges, as bending delicate thin transducer elements often leads to high failure rates [27]. Some approaches introduce motors to rotate sensors [28]; however, these compromise the simplicity and safety of magnetic manipulation, increase power consumption, and fail to address the overall dexterity of magnetic medical robots. These challenges underscore the need for enhanced dexterity in a clinically applicable manner, without additional actuation modes.

Inspired by embodied intelligence and the geometry of developable rollers, this work introduces a clinically applicable approach for generating torque around the magnetization axis in magnetic medical robots. This is achieved by geometrically coupling the existing two DoFs magnetic torque using just five magnetic control inputs for roll control, while still maintaining independent control over the original two DoFs. Developable rollers, observed in applications such as classical and quantum optics [29], sphericon-shaped magnetic milli-robots [30], and fluid mixing are known for their unique meandering rolling motions (Figure 3.2B). This innovation specifically leverages the oloid shape to achieve axial rotation, utilizing its axial asymmetry and interaction with the environment (see Movie S1). This method, demonstrated on the MFE platform, is agnostic to how the controlling magnetic field is generated, extending roll recovery to any magnetic manipulation system with at least five magnetic control inputs, including electromagnetic coil systems.

To validate this approach, we developed and evaluated a differential geometry-based control model for source-agnostic magnetic manipulation of an Oloid-shaped Magnetic Device (OMD) on various clinically relevant surfaces. In line with its motivation in GI endoscopy, OME was designed and its ability to perform rolling and sweeping motions

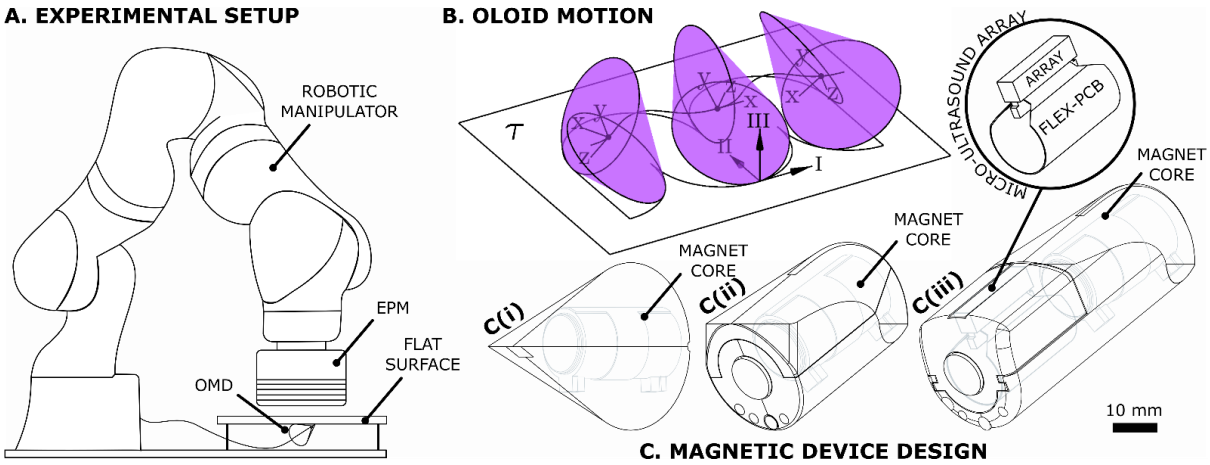

Figure 3.2: **Experimental setup and design overview of the Oloid-shaped Magnetic Devices.** (**A**) Benchtop experimental setup for the roll control experiments. (**B**) Illustration of the oloid shape rolling on a horizontal plane, T (based on Dirnbock et al. [31] (**C(i)**) Oloid-shaped magnetic device, (**C(ii)**) Oloid-shaped magnetic endoscope and, (**C(iii)**) Oloid shaped magnetic endoscope with integrated microUS array.

alongside existing DoFs demonstrated. To enable virtual biopsies, a 32-element, 28 MHz microUS linear array (Figure 3.2C(iii)) was integrated to capture high-resolution subsurface images. Autonomous microUS sweeping and 3D subsurface image reconstruction were achieved using a custom coupling detection algorithm, validated through both in vitro and in vivo testing in a porcine model. Finally, the system's ability to provide clinicians with in-situ lesion margin and staging information was evaluated in vivo by performing virtual biopsies of an artificially introduced polyp.

3.3 Results

3.3.1 The DoF Limitation in Magnetic Manipulation

Magnetic manipulation in medical robotics is simplified through the dipole model where magnets are represented as magnetic dipoles (see Figure 3.3). This simplification remains accurate as the distance between the controlling source and the robot generally exceeds two times the size of the internal magnet [32].

As shown in Figure 3.3B, a magnetic object (internal dipole) with magnetic moment, $\mathbf{m}_I \in \mathbb{R}^3(ampere \cdot square\ meter)$ placed in an external magnetic field $\mathbf{B}_E \in \mathbb{R}^3(tesla)$

experiences both an alignment torque τ_m and gradient-induced force $\mathbf{F}_m$. These are generated by the external dipole to minimize the system's potential energy. Conventionally, the magnetization axis of a magnetic object aligns with its local coordinate frame such that $\mathbf{X_I}$ is parallel to $\mathbf{m}_I$. However, since magnetic alignment torque is defined by the cross product $\tau_m = \mathbf{m}_I \times \mathbf{B_E}$, when $\mathbf{m}_I$ is parallel to $\mathbf{B_E}$, $\tau_m = \mathbf{0}$. As a result, magnetic alignment torque can only be generated around axes perpendicular to $\mathbf{m}_I$, meaning it is not possible to generate magnetic alignment torque around an object's magnetization axis to control the roll angle (ϕ). A visual representation and practical demonstration of this phenomenon are provided in Movie S1 along with a detailed mathematical explanation in the Supplementary Discussion.

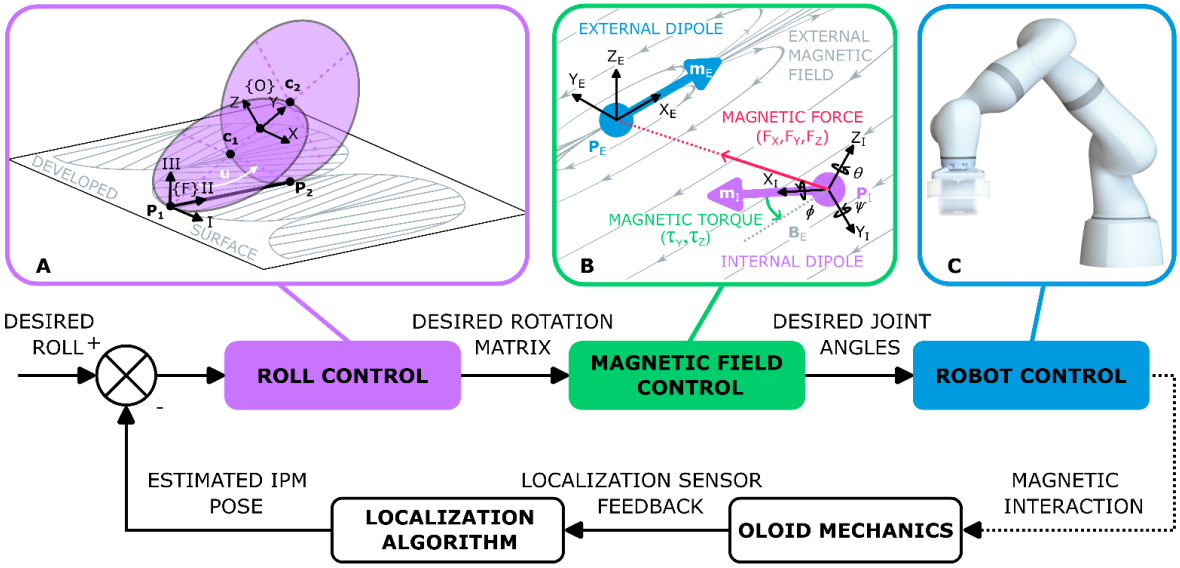

Figure 3.3: **Block diagram control schematic for closed-loop control of the Oloid.** (**A**) Roll control (purple): The differential geometry model of the oloid is illustrated according to [31] with (**X,Y,Z**) representing the local oloid coordinate frame {O} and (**I,II,III**) the fixed frame {F}. The developed surface corresponding to the projection of the oloid's generators is shown in grey. The centers of the oloid's defining circles are marked by $\mathbf{c}_1$ and $\mathbf{c}_2$ with contact points on the plane denoted by $\mathbf{P}_1$ and $\mathbf{P}_2$. (**B**) Magnetic field control: Shows the dipole-dipole model approximation where $\mathbf{p}_E$ and $\mathbf{p}_I$ are point dipoles and $\mathbf{m}_E$ and $\mathbf{m}_I$ represent the magnetic moments. Magnetic forces F_x, F_y and F_z and aligning torques τ_y and τ_z act on the internal dipole. Magnetic field lines represent the magnetic field $\mathbf{B}_E$ generated by the external dipole, which becomes uniform near the internal dipole. No torque τ_x is shown, as torque cannot be generated around the internal dipole's magnetization axis X_I (**C**) Robot control (blue): Single EPM system enabling precise magnetic field manipulation to control the Oloid's motion.

Related work has explored the use of magnetic force to produce off-axis rigid body torques

to control roll around the object's magnetization axis. This is achieved by coupling force and torque control through the inclusion of multiple discrete magnets [8], [9], [33] or by using a single magnet with a non-uniform magnetization or anisotropic shape [10]–[13].

The Oloid

Coupling existing DoFs to regain roll control in magnetic manipulation required a geometry with axial asymmetry. For bi-directional rolling, the geometry also needed at least one plane of symmetry, allowing roll actions in two distinct, opposing directions.

The oloid, distinguished from others in the developable roller family, is formed by joining two perpendicular, equal intersecting circles with a distance between their centers ($\mathbf{c}_1$ and $\mathbf{c}_2$) equal to their radii (shown in Figure 3.3). This unique shape lacks vertices and maintains continuous surface contact during rolling due to its developable, flattenable (developed) surface (Figure 3.3). As a ruled surface, it is generated by straight lines (generators) connecting its circles at points $\mathbf{P}_1 \in \mathbb{R}^3$ and $\mathbf{P}_2 \in \mathbb{R}^3$, along a directrix. This leads to its parametric equation:

$$\mathbf{r}(u, v) = \mathbf{P}_1(u) + \ v\,(\mathbf{P}_2(u) - \mathbf{P}_1(u)) \tag{3.1}$$

where $\frac{-2\pi}{3} \leq u \leq \frac{2\pi}{3}$, $0 \leq v \leq 1$.The script to generate the 3D surface of the oloid using Equation 3.1 has been made available in our accompanying Data repository.

When an oloid rolls on a flat plane, one generator line contacts the plane becoming the instantaneous axis of rotation, with angular velocity, $\omega \in \mathbb{R}^3$ (rad/s), parallel to this line and tangent to the plane, expressed as:

$$\omega \parallel \mathbf{P}_2 - \mathbf{P}_1 \Rightarrow \omega \times (\mathbf{P}_2 - \mathbf{P}_1) = \mathbf{0} \tag{3.2}$$

To control rotation around a robot's magnetization axis using geometric misalignment and two DoFs magnetic torque, the magnetization axis must not be parallel to the object's angular velocity.

This exists in the oloid over the controllable range, in direct contrast with a shape like the cylinder where its angular velocity is always parallel to its central axis. See "Roll Generation in the Oloid" in the Supplementary Discussion for further details.

OME versus MFE DoFs

To embody the unique rolling abilities of the oloid into the OME design (Figure 3.2C(ii)), its pure form was adapted to meet clinical requirements and to incorporate essential endoscope features. This required evaluating the oloid's functional areas and their relation to the range of roll motion. By merging the key elements of the oloid with the cylindrical MFE, a hybrid design was achieved that adhered to clinical size constraints, as detailed in "Oloid Shape Integration" in Materials and Methods.

Dexterity was assessed through a direct comparison between the MFE which has a cylindrical shape and the OME, evaluating their ability to perform independent tilt and yaw motions, as well as coupled rolling motion (see "Magnetic Actuation of the Endoscope" in Materials and Methods for details). These experiments were conducted on lubricated Perspex using the MFE's robotic system as illustrated in Figure 3.2A.

As shown in Figure 3.4 and Movie S2, the OME not only enabled controlled rolling motion—albeit coupled with tilt and yaw—but also allowed for more independent tilt and yaw control compared to the MFE's cylindrical design. The MFE experienced uncontrollable roll during manipulation, minimized in past designs through offset IPM placement for corrective torque and minimal-energy orientation. In GI endoscopy, due to its tubular nature, tilt and yaw are the primary DoFs, with roll desired only for specific tasks like tissue scanning or tool or camera manipulation. See Figure A.2 in Supplementary Figures for x, y translational experiments and the orientation-time graphs used to generate the radar plots in Figure 3.4.

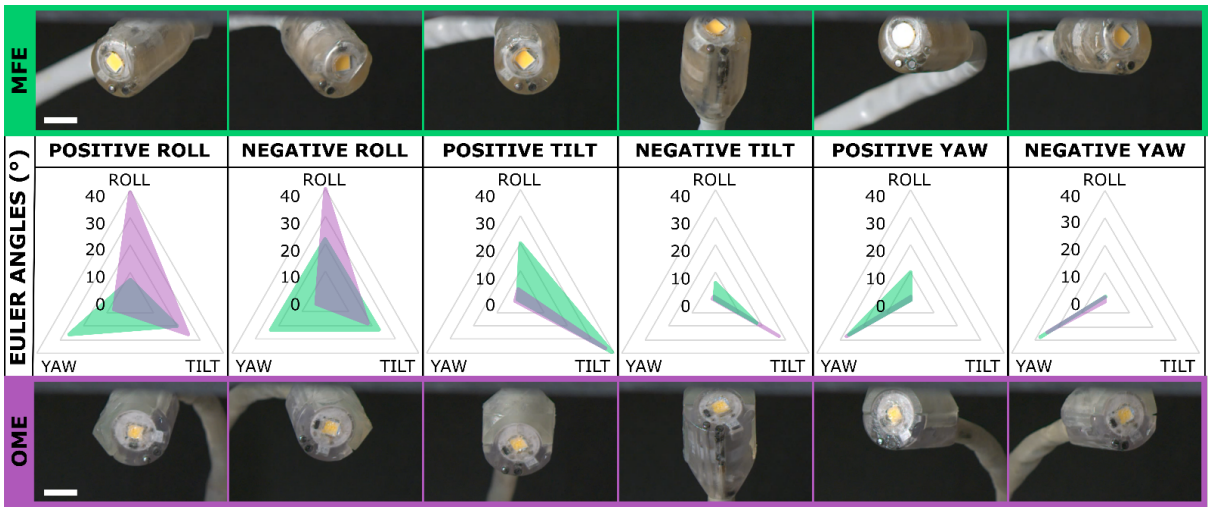

Figure 3.4: **Comparison of 3-DoF orientation control between the Oloid Magnetic Endoscope (OME) and the Magnetic Flexible Endoscope (MFE).** The figure illustrates the coupling between positive and negative roll, tilt, and yaw for the MFE (green) and OME (purple). Radar plots for each DoF display the average absolute deviations in roll, tilt, and yaw (measured in degrees) across three repetitions (Figure S2). The scale bars represent 10 mm. See Movie S2 for related multimedia.

3.3.2 Generating Rolling Motion with the Oloid in Open-Loop

To control the oloid's rolling motion, we used an analytical differential geometry model detailed in "The Oloid Model" in Materials and Methods. This model defined the line of contact during rolling and calculated the corresponding transformation matrix for the oloid's local coordinate frame. We hypothesized that adjusting the applied magnetic field according to this sequence would replicate the desired rolling motion in an OMD in open-loop.

We developed an OMD (Figure 3.2C(i)) with a 3D-printed oloid-shaped shell (20 mm radius, 60 mm length) that accommodated an IPM with integrated localization. This localization data tracked the roll and compared it to the model's predictions. Assuming perfect magnetic coupling, the EPM was programmed to follow the transformation matrix sequence. Initial tests on a high-friction silicone substrate (Figure 3.5A and Movie S3) emulated the model's non-slip condition. Tests were repeated on bumpy foam, flat foam, and Perspex (Figures 3.5B-D and Movie S3) to evaluate performance across different surfaces over a 180° range (see Figure A.3 for extended results). The silicone surface closely

matched the model's non-slip condition, showing the highest correlation with predicted motion, while Perspex, which was unable to maintain the non-slip condition, showed the least correlation. A scaled-down demonstration was performed in an electromagnetic coil with a mini-OMD (Figure A.4) to assess the model's versatility and scalability. These results indicate that although this open-loop setup can achieve rolling motions in a range of conditions, a closed-loop control system was crucial for precise control, particularly when environmental conditions differed from model assumptions.

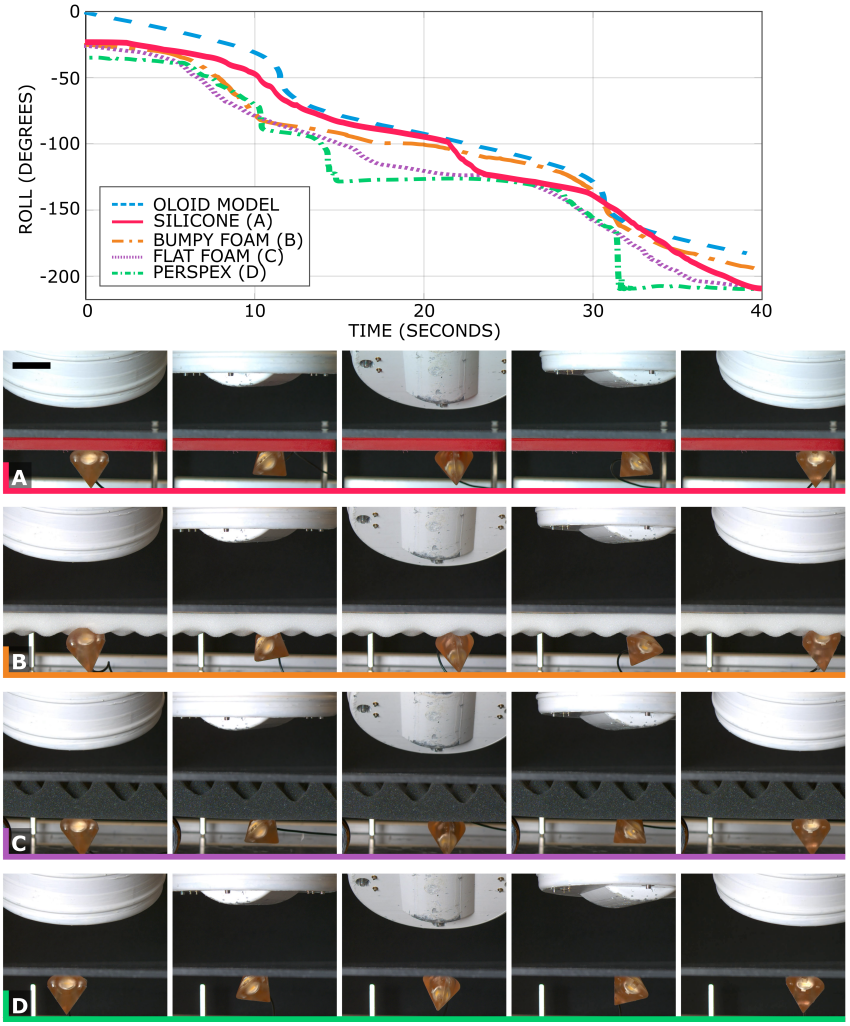

Figure 3.5: **Open-loop control of the OMD on various surfaces.** The oloid's rolling behavior on (**A**) silicone, (**B**) bumpy foam, (**C**) flat foam and (**D**) Perspex, compared to the predicted roll from the oloid model. Each snapshot shows the EPM position and orientation for reference. The scale bars represent 30 mm. See Movie S3 for related multimedia

Closed-Loop Control of the Oloid

In real-world medical settings, magnetic coupling cannot be reliably assumed, necessitating device localization. Additionally, manufacturing imperfections and environmental factors lead to deviations from the model, prompting the development of a differential geometry-based closed-loop control system for the oloid (detailed in Materials and Methods). Here the oloid's closed-loop controllability and therefore its potential for innovation in medical devices was evaluated. The OMD was tested on surfaces simulating the internal GI tract structures, such as mucus-lubricated curved (colon, esophagus) and flat (stomach) surfaces.

Initial tests on a non-lubricated flat surface established a performance baseline (Figure 3.6A). Subsequently, more complex conditions were introduced, including lubricated (Figure 3.6C & D) and curved surfaces (Figure 3.6B & D). On the initial flat surface, a 0° to 180° step function input demonstrated a full range of motion. For lubricated and curved surfaces, a 0° to 90° step function input was applied. The results, exhibited in Figure 3.6 (see Figure A.5 for extended results) and Movie S4, highlight the system's adaptability and precise control across all test conditions. The lubricated surfaces enabled the oloid's ability to decouple roll from translation and generate pseudo-on-axis roll effectively.

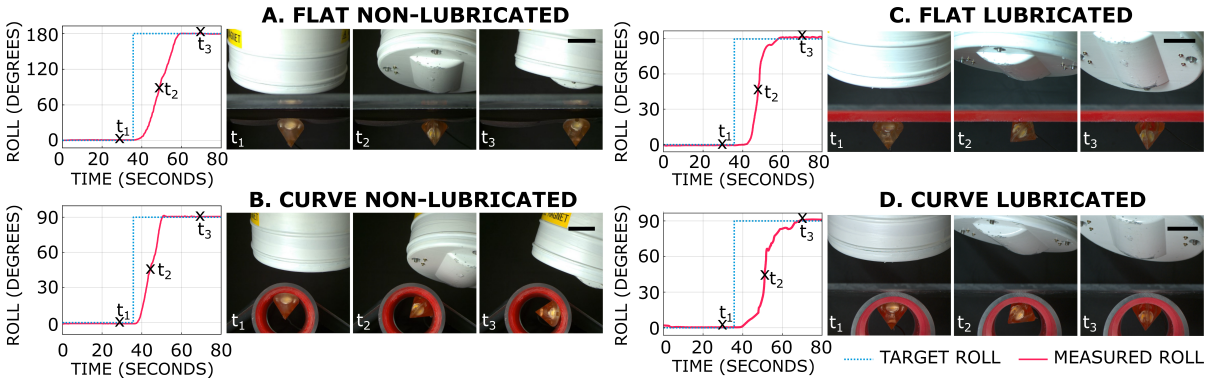

Figure 3.6: **Closed-loop control of the OMD with step input on various surfaces.** Rolling performance is shown on (**A**) a flat, non-lubricated surface, (**B**) a curved, non-lubricated surface, (**C**) a flat, lubricated surface, (**D**) a curved, lubricated surface. Snapshots at times t_1, t_2, and t_3 progress from left to right. The scale bars represent 30 mm. See Movie S4 for related multimedia.

3.3.3 In vivo Rolling and Sweeping Motions

For a practical in vivo demonstration of the system's clinical relevance, we selected a porcine model due to the similarity of porcine and human GI anatomy. The primary goal of the in vivo trials was to validate the OME's ability to perform controlled rolling and sweeping motions in realistic conditions of friction and tissue interaction.

Two distinct experiments were designed to support these capabilities: one to observe the OME's sweeping motion across the top half of the lumen of the colon and the other to assess its pure rolling motion within a ±50° range. The results, displayed in Figure 3.7 and Movie S5, include snapshots from a separate standard endoscope camera (see Figure A.8) capturing the sweeping and rolling motions of the OME. Notably, the sweeping motion, which combined horizontal translation and roll motion to produce an arch-like effect, achieved a range of ±60°. This combined motion enabled radial scanning by the sensor, with rolling adjusting the probe's orientation and translation moving the endoscope across the surface.

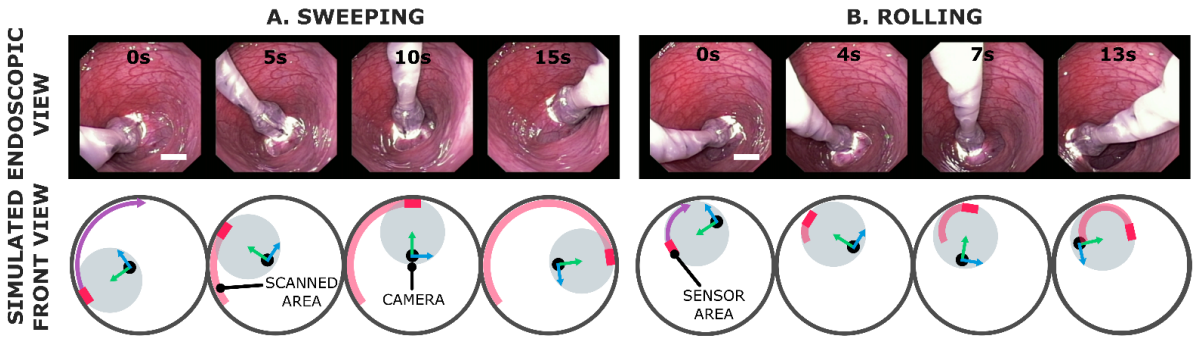

Figure 3.7: **In vivo sweeping and rolling of the Oloid Magnetic Endoscope (OME).** Selected views from the standard endoscope camera and mirrored simulated front views show the motion of the OME's sensor area and camera during (**A**) sweeping and (**B**) rolling motions. The black circle with blue and green arrows represents the OME's onboard camera and its frame, while the purple arrow indicates the planned motion of the sensor area. The scale bars represent 20 mm. See Movie S5 for related multimedia.

3.3.4 Pre-clinical Validation – Virtual Biopsy 3D Reconstruction

The primary motivation of this work was to enable virtual biopsies in MFEs, to enhance diagnostic capabilities beyond those of standard flexible endoscopes. Virtual biopsies allow for detailed tissue analysis, such as assessing lesion malignancy and margins, without the need for physical biopsies.

The OME is sensor-agnostic, however, for demonstration purposes, we integrated a 32-element 28 MHz microUS array called the Oloid-shaped Magnetic Endoscope - Ultrasound (OME-U) (see the "Ultrasound Integration" section). By combining our autonomous sweeping algorithm (see the "Autonomous Sweeping" section) with precise six DoF localization, the system generated comprehensive microUS imaging datasets. These datasets integrated high-quality Two- Dimensional (2D) ultrasound images with positional data, allowing for the creation of high-fidelity 3D reconstructions of target areas. This process is outlined in the "3D Reconstruction" section.

Preliminary validation was conducted on a benchtop setup with a silicone phantom and the OME-U (Figure 3.2C(iii)). The phantom included copper bands as echogenic subsurface targets. Signals were accurately captured and reconstructed, confirming system precision (see Figures S6, S7 and Supplementary Methods).Further validation was conducted in vivo by performing an autonomous sweep over healthy tissue followed by a simulated flat polyp in the same region of the porcine colon, created by injecting submucosal lifting agent (see Figure 3.8A and Movie S6).

The 3D reconstructed volumes were visualized dynamically using MATLAB (Figure 3.8C and Movie S6), allowing operators to rotate, translate, and zoom. An isosurface representation feature enabled detailed inspection of tissue features (Figure 3.8D) through customizable visibility thresholds (see "3D Reconstruction").

This was particularly effective in visualizing the flat polyp structure within the 3D volume (Figure 3.8D(ii)), showcasing the diagnostic potential of the approach. While elements at depth can be observed even in the no polyp case, these features are less intense and

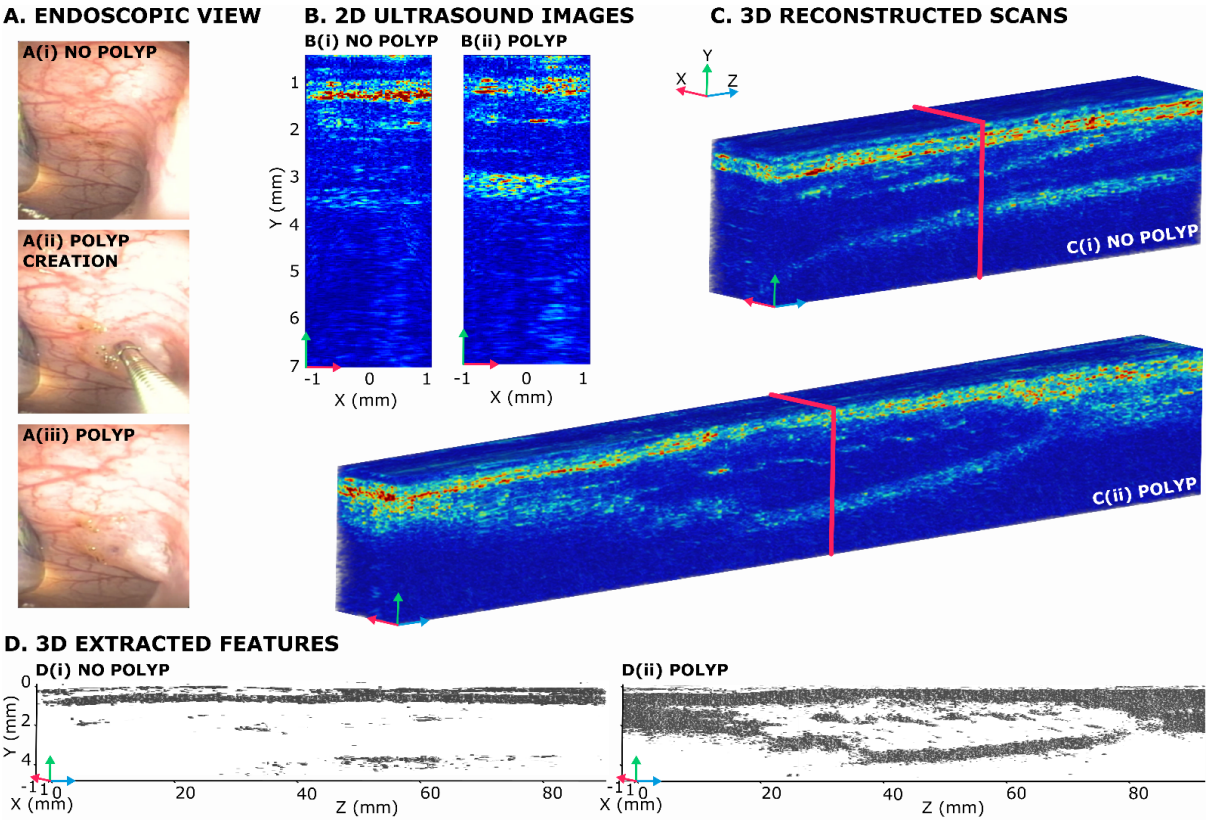

Figure 3.8: **In vivo subsurface 3D reconstruction of microUS images for achieving virtual biopsies with the OME.** (**A**) Endoscopic view showing stages 1-3 of polyp creation. (**B**) 2D Ultrasound images: (**B(i)**) without polyp and (**B(ii)**) with polyp, (**C**) 3D Reconstruction of the ultrasound scans: (**C(i)**) without polyp and (**C(ii)**) with polyp, with the red square indicating the position of the 2D images (**B(i)**) and (**B(ii)**) within the 3D scan. (**D**) 3D Isosurface rendering highlights extracted features of interest: (**D(i)**) without polyp and (**D(ii)**) with polyp. See Movie S6 for related multimedia.

inconsistent, whereas the polyp case shows a discontinuity in two layers that meet at both ends.

The accuracy of the 3D reconstruction was assessed by comparing the reconstructed volume of the polyp against the injected volume, showing a 9.6% overestimation (injected volume: 1 ml, reconstructed volume: 1.106 ml).

3.4 Discussion

This work introduces an approach to closed-loop roll control in magnetic medical devices, particularly MFEs, using an oloid-shaped design. This shape provides additional dexterity, enabling controlled rolling without additional power consumption or actuation modes,

ideal for endoscopes including untethered capsule endoscopes. A precise closed-loop control scheme that integrates MFE localization was developed, addressing scenarios where perfect magnetic coupling cannot be assumed. Roll control was effectively demonstrated in benchtop trials and subsequently in in vivo trials.

This study has demonstrated the approach across different scales (OMD, OME, and mini OMD) and control sources (single EPM and electromagnetic coil system), in both tethered and untethered configurations. Although our differential geometry-based model provides a framework for broad clinical applications using any magnetic field source with at least five magnetic control inputs, comprehensive parametric studies are needed to validate utility in other applications. For example, extending this approach to more dynamic surfaces than the colon will require real-time model parameter estimation.

The design and in vivo testing of the OME within the colon demonstrated the capacity of the oloid to be integrated into a device that met the specific design requirements for colonoscopy achieving safe rolling motion and an application-specific sweeping motion. Our results also demonstrated that the OME could roll, tilt, and yaw with greater independence and stability than cylindrical MFEs, which do not have active roll control.

Previous work [3] was confined to 2D scans using single-element transducers, as linear arrays were impractical due to the absence of roll control. By leveraging roll control, our approach enabled robotically controlled, autonomous sweeping to create 3D microUS images with deeper anatomical reach than transrectal microUS. These virtual biopsies offer potential real-time diagnostic insights without requiring physical samples.

The OME's sensor-agnostic design supports the integration of various diagnostic or therapeutic modalities, such as Optical Coherence Tomography [34] or therapeutic lasers [35], making it adaptable for future applications. In addition, roll control could facilitate precise interventions like submucosal dissection, and targeted ultrasound-triggered drug delivery [36], [37].

The oloid-based roll control system and autonomous virtual biopsies contribute to the expanding autonomy of MFEs, which includes autonomous navigation [38], polyp de-

tection, and shared control physical biopsy tasks [20]. These advancements could allow endoscopists to focus on critical diagnostic and therapeutic decisions while autonomous systems handle routine navigation and tasks [39]. This could also reduce the training times for endoscopists and potentially allow multiple procedures to be supervised simultaneously.

The single EPM system of the MFE has been validated in human trials with patients of normal Body Mass Index (BMI) [19], however, patients with higher BMI pose challenges due to increased EPM- IPM distances, reducing magnetic force and torque. Increasing the EPM size to generate stronger magnetic fields, can potentially address these limitations. Additionally, the current single EPM system limits vertical (z-axis) control, causing the endoscope to remain in constant contact with the top half of the lumen of the colon. To extend the sweeping range to include the lower half, patient repositioning is required. This design approach is consistent with standard clinical practice, where patient repositioning is a method for ensuring comprehensive colon examination [40]. However, implementing more complex field generation systems [1], [14]–[16] would enable full 360° scanning in scenarios where patient repositioning is not possible. Rolling demonstrations with the electromagnetic coil system revealed this potential, showing successful oloid movement across lower surfaces.

Furthermore, the OME's enhanced dexterity and diagnostic capabilities have the potential to address gender disparities in colonoscopies, as standard flexible endoscope procedures tend to be more challenging in women, leading to higher rates of incomplete procedures and lower adenoma detection rates [41]. In conclusion, the oloid shape facilitates clinically applicable torque generation around the magnetization axis in magnetic medical robots, enhancing the dexterity, diagnostic capabilities, and autonomy of MFEs and magnetic medical robots overall. This approach sets the stage for more autonomous and efficient medical procedures deep within the anatomy. With ongoing clinical validation, such advancements have the potential to transform minimally invasive diagnostics and treatments, making them more accessible and effective for a broader range of patients.

3.5 Methods

The Oloid Model

For the successful control of magnetically manipulated oloid-shaped devices, a deep understanding of the oloid's motion was crucial. Although previous studies have modeled the behavior of the oloid—or "two-circle roller"—on flat surfaces [34], [42], [43], our work is based on an adaptation of the differential geometry framework by Dirnbock et al. [31] where full derivations can be found. In this work, the application of the previous model was extended to curved and lubricated surfaces for any defining oloid radius, r.

We assign a fixed coordinate frame {F} with orthonormal vectors $\mathbf{I},\ \mathbf{II}, \mathbf{III} \in \mathbb{R}^3$ on the plane for the initial position and orientation of the oloid. As the oloid moves along the plane, its motion can be parametrized by the arc length u (*radian*) of the contact point, $\mathbf{P}_1$, on the edge of one of its circles over the region:

$$u \in \left(-\frac{2\pi}{3}, 0\right) \cup \left(0, \frac{2\pi}{3}\right) \tag{3.3}$$

If {O} denotes the coordinate frame with orthonormal vectors $\mathbf{x},\ \mathbf{y}, \mathbf{z} \in \mathbb{R}^3$ at the geometric center of the oloid, then the homogeneous transformation matrix of {O} with respect to {F} is:

$$\mathbf{T}_F^O = \begin{bmatrix} \mathbf{R}_F^O & \mathbf{t}_F^O \\ \mathbf{0} & 1 \end{bmatrix} \in SE(3) \tag{3.4}$$

where, using $s = sin(u)$ and $c = cos(u)$ for brevity:

$$\mathbf{t}_F^O = \frac{r\sqrt{3}}{9}\begin{bmatrix} \frac{cs\sqrt{1+2c}}{2(1+c)\sqrt{2(1+c)}} + sign(u)arccos(u)\frac{c\sqrt{2}}{\sqrt{1+c}} \\ \frac{15+13c-c^2}{2(1+c)} + ln\left(\frac{2}{1+c}\right) \\ \frac{3\sqrt{3}(2+c)}{2\sqrt{2(1+c)}} \end{bmatrix} \in \mathbb{R}^3 \tag{3.5}$$

is the translation vector and:

$$\mathbf{R}_p^O = \frac{\sqrt{3}}{9}\begin{bmatrix} \frac{(5+c)\sqrt{1+2c}}{\sqrt{2(1+c)}} & \frac{(2+c)s\sqrt{1+2c}}{(1+c)\sqrt{2(1+c)}} & \frac{(5+4c)s}{(1+c)\sqrt{2(1+c)}} \\ \frac{(c-1)s}{1+c} & \frac{5+5c-c^2}{1+c} & -\frac{(1+2c)\sqrt{1+2c}}{1+c} \\ -\frac{3s\sqrt{3}}{\sqrt{2(1+c)}} & \frac{3c\sqrt{3}}{\sqrt{2(1+c)}} & \frac{3\sqrt{3(1+2c)}}{\sqrt{2(1+c)}} \end{bmatrix} \in SO(3) \tag{3.6}$$

is the rotation matrix.

The model assumes that the oloid undergoes pure, no-slip rolling on a perfectly horizontal surface. Additionally, its center of mass aligns with its geometric center and its overall rolling direction remains fixed in the initial reference frame.

These assumptions demonstrate that while the pure oloid model captures rolling on flat, high-friction surfaces, modifications were required for curved and lubricated environments.

To adapt the model for non-planar surfaces and to select rolling direction, we introduced a rolling surface element, $\mathbf{R}_S \in SO(3)$, and a rolling direction element, $\mathbf{R}_D \in SO$ with respect to {F}. $\mathbf{R}_S$ rotates the model in **II** to account for changes in the angle of the surface normal as the oloid rolls on non-planar surfaces and $\mathbf{R}_D$ adjusts for the desired rolling direction in **III**.

For curved cylindrical surfaces, adjustments were calculated based on the surface's approximate radius, $r_c(meters)$. The translation in **I** (Figure 3.2B) of the oloid's center of mass, $\mathbf{s}(u) \in \mathbb{R}^3$, was used in the arc length equation to derive the angle of the surface

normal, $\boldsymbol{\theta}(u)$, relative to the horizontal, as a function of u.

$$\boldsymbol{\theta}(u) = \mathbf{s}(u)/r_c \tag{3.7}$$

$\boldsymbol{\theta}(u)$ was then used to define $\mathbf{R_s}$ for every u.

This adjustment was only necessary on non-lubricated surfaces since lubricated surfaces characterized by stick-slip motion [44], remove the pure no-slip constraint, decoupling translation from rotation. For lubricated surfaces, the control system used the unaltered rotation matrix for orientation and original control for x and y translation. In open-loop, the full unaltered transformation matrix assumed the no-slip condition. For closed-loop, this condition was assumed only in non-lubricated cases, with adjustments applied for curved surfaces using pre-measured parameters (r_c). In both lubricated cases, the system utilized the unaltered rotation matrix exclusively, omitting translation to maintain a central position and demonstrate pseudo on-axis roll. The MATLAB scripts for this model have been made available in our accompanying Data repository.

Roll Closed-Loop Control

To control the rolling motion of the OMD in a closed-loop system, we leveraged the closure and inverse property of the SO group to denote the rotation matrix error as follows:

$$\mathbf{E} = \mathbf{R}_d\mathbf{R}^T = e^{S(\boldsymbol{\varepsilon})} \in SO(3) \tag{3.8}$$

where $S(\boldsymbol{\varepsilon}) \in \mathfrak{so}(3)$ is the Lie algebra of $\mathbf{E}$ (a skew-symmetric matrix). Here, $\widehat{\boldsymbol{\varepsilon}} = \frac{\boldsymbol{\varepsilon}}{\|\boldsymbol{\varepsilon}\|} \in \mathbb{R}^3$ is the axis of rotation error, and $\| \boldsymbol{\varepsilon} \|$ is the magnitude of the rotation error in radians. Taking the time derivative of the error, we obtained:

$$\dot{\mathbf{E}} = S(\dot{\boldsymbol{\varepsilon}})\mathbf{E},\ \dot{\boldsymbol{\varepsilon}} = \boldsymbol{\omega}_d - \boldsymbol{\omega} \tag{3.9}$$

From this, we denote the input angular velocity as:

$$\boldsymbol{\omega} \triangleq \boldsymbol{\omega}_d + \mathbf{K}_1\boldsymbol{\varepsilon} \tag{3.10}$$

where $\mathbf{K}_1 \in \mathbb{R}^{3\times3}$ is a positive-definite gain matrix. This formulation ensured that errors decay exponentially over time:

$$\dot{\boldsymbol{\varepsilon}} = -\mathbf{K}_1\boldsymbol{\varepsilon} \implies \boldsymbol{\varepsilon}(\mathrm{t}) = e^{-\mathbf{K}_1\boldsymbol{\varepsilon}\mathrm{t}}\boldsymbol{\varepsilon}_0 \tag{3.11}$$

with ε_0 is the initial error at $t = 0$. The setup guaranteed that the error decays exponentially:

$$\lim_{\mathrm{t}\to\infty} \boldsymbol{\varepsilon}(\mathrm{t}) = \mathbf{0} \tag{3.12}$$

At $\boldsymbol{\varepsilon} = \mathbf{0}$, we have $e^{S(0)} = \mathbf{I}$, meaning that $\mathbf{R} = \mathbf{R}_d$, which aligns the desired and actual orientations. Finally, the torque variation is set proportional to velocity. For $\omega_d = \mathbf{0}$, the equation simplifies to:

$$\delta\boldsymbol{\tau} = \mathbf{K}_2\boldsymbol{\omega} = \underbrace{\mathbf{K}_2\ \mathbf{K}_1}_{\mathbf{K}}\boldsymbol{\varepsilon} \tag{3.13}$$

This desired torque variation served as the control input for the magnetic field system, enabling precise roll control as detailed in "Magnetic Actuation of the Endoscope". Through

magnetic interactions and the mechanics of the oloid, the device's pose was adjusted, with continuous pose measurement via the IPM's localization system, completing the feedback loop. As illustrated in Figure 3.3, the roll control stage calculated the necessary torque adjustments. This information was fed into the magnetic field control, where a simple proportional controller managed orientation control. To enhance operational efficiency, a predefined lookup table of the oloid's differential geometry model was employed to eliminate the need to recompute transformation matrices at each step.

Robotic System Design

The system (Figure 3.2A) consisted of an EPM (cylindrical, axially magnetized, 101.6 mm in diameter and length, NdFeB, N52 grade, KJ Magnetics) positioned at the end effector of a medical-grade, 7- DoF serial robotic manipulator (LBR Med R820, KUKA) which was used to steer a tethered magnetic device with an embedded IPM. Actuation was achieved by applying magnetic forces and torques to the IPM to modify its position and orientation by adjusting the pose of the EPM. Surrounding the IPM was a flexible circuit containing Hall Effect sensors and an Inertial Measurement Unit (IMU) for IPM localization. The data from the Hall effect and IMU sensors of the IPM, influenced by its current pose within the EPM's magnetic field, along with an additional non-actuating field generated by an electromagnetic coil surrounding the EPM, enabled real-time estimation of the magnetic device's pose at a frequency of 100 Hz [44]. This feedback was crucial for implementing closed-loop control and automated tasks.

The user interface included a joystick to navigate the GI tract with the OME based on visual feedback from the embedded camera (Figure 3.1B). Diagnostic images were captured with the microUS array using a research array controller (Vantage HF 128, Versaonics) and post-processed using MATLAB (MathWorks, Inc.). The components were interfaced with the Robot Operating System (ROS) owing to the modularity and straightforward multi-threading capabilities of ROS.

Three magnetic devices were developed for this paper. The first was an OMD (Figure 3.2C(i)), used to validate a differential geometry-based closed loop control model for the

oloid shape. The second was an OME (Figure 3.2C(ii)), utilized to demonstrate the clinical applicability of this approach. The third was an adapted version of the OME, which included a microUS array (OME-U) (Figure 3.2C(iii)). A design-specific localization calibration process (see Supplementary Methods) was implemented to mitigate the effect of any manufacturing imperfections in each of these designs.

Magnetic Actuation of the Endoscope

The control of the endoscope pose was split into two separate subsystems, one dedicated to the orientation control, and another one dedicated to the position control. Due to the inherent nonlinearities of the field $\mathbf{B}_E$, the global relation between EPM motions and torques/forces is nonlinear. Given the local nature of the movements and the low velocity of the robot and the endoscope, the control approach adopted was linearized. The validity of the models and control action were therefore only local, commanded movements must be small and the boundary conditions needed to be computed at every time step.

Orientation control was achieved locally by converting the desired torque variation ($\delta\boldsymbol{\tau}$) into the desired motion of the EPM. In the case of roll control, $\delta\boldsymbol{\tau}$ was an output of the roll control stage. For tilt and yaw, $\delta\boldsymbol{\tau}$ was simply the desired change in τ_y and τ_z, respectively. Using the magnetic dipole model and Maxwell's force/torque equations (see Supplementary Discussion), we defined a magnetic Jacobian that relates the positions and orientations of the IPM and EPM to the forces and torques applied to the IPM, assuming a constant pose of the IPM:

$$\begin{bmatrix} \delta\mathbf{f}_{lin} \\ \delta\tau_{lin} \end{bmatrix} = \mathbf{J}_F\left(\mathbf{p}_E, \mathbf{p}_I, \widehat{\mathbf{m}_E}, \widehat{\mathbf{m}_I}\right) \begin{bmatrix} \delta\mathbf{p}_E \\ \delta\widehat{\mathbf{m}_E} \end{bmatrix} \tag{3.14}$$

where $\mathbf{p}_E$, $\mathbf{p}_I \in \mathbb{R}^3$ are the positions of the EPM and IPM (Figure 3.3), $\widehat{\mathbf{m}_E}$ and $\widehat{\mathbf{m}_I}$ $\in \mathbb{R}^3$ are their orientations, and $\delta\mathbf{F}_{lin}$, $\delta\boldsymbol{\tau}_{lin} \in \mathbb{R}^3$ represent the variation of $\mathbf{F}_m$ and $\boldsymbol{\tau}_m \in \mathbb{R}^3$ with respect to a local configuration change.

By inverting the Jacobian (using a damped least-squares approach), we compute $\delta\mathbf{p}_E$ and $\delta\widehat{\mathbf{m}_E}$, favoring rotation for torque control to maintain the EPM's position directly above the IPM. Further details on force/torque control, including how the dipole-dipole model was used to determine the motion of the EPM and the robot joints necessary to control the IPM, as well as the real-time 6 DoFs localization system, were presented in previous work (3).

Oloid Shape Integration

While the pure oloid provides a theoretical maximum range of 360° rotation and roll stability, incorporating essential magnetic endoscopic components such as a camera, Light Emitting Diode (LED), IPM with localization, tubes for insufflation, irrigation, and Camera Cleaning requires enlarging the device beyond a clinically practical size. Conversely, cylindrical designs accommodate these components but offer no controlled rolling motion. Embedding the oloid within a cylindrical form retains essential rolling capabilities while maintaining a practical device size, achieving a balanced hybrid design suitable for clinical applications.

These generator lines that develop the oloid's surface determine its interaction with surfaces, allowing for a smooth rolling motion as each line sequentially contacts the surface. The extent of these lines on a device determines its range of motion. In a single EPM system like the MFE, the endoscope is primarily attracted to the upper surface of the environment, specifically the top half of the lumen of the colon. Thus, only the upper surface of the endoscope required functionalization, incorporating two of the four quadrants of the oloid shape. To maintain pure tilt control from a neutral position, a flat chamfer was added to the top edge of the oloid shape.

The OME was manufactured using a 3D printed resin shell (Form 3+, Formlabs). The resulting OME, shown in Figure 3.2C(ii), has compact dimensions of 20 mm x 20 mm x 35 mm in line with the previous MFE design.

Ultrasound Integration

The microUS probe incorporated into the OME was a commercially supplied 28 MHz, 128-element linear array (L28SXTech, VERMON S.A) that was adapted for the application. Microcoaxial cables (42 AWG - Alpha Wire) were directly soldered to the flexible PCB pads corresponding to the array elements, with an additional cable for the PCB's ground connection. The microcoaxial cables from the array were terminated with LEMO connectors and connected to the Verasonics controller for US transmission and data acquisition.

Modifications were made to the OME design to accommodate the microUS probe resulting in the OME-U (Figure 3.2C(iii)), comprising a detachable section incorporating the sensor. This design choice was driven by sustainability considerations to facilitate the testing and reuse of various sensors, while the main endoscope can be discarded as its lumens are difficult to clean. This also ensures that the endoscope remains adaptable and versatile for different medical applications.

The array was driven using a synthetic aperture protocol [45] modified to use five transmitting elements (Tx) in parallel and all receive elements (Rx) for each acquisition to maintain electrical power levels within reasonable bounds, while improving the Signal to Noise Ratio (SNR) compared to the conventional US B-mode imaging protocol that uses only one Tx element per acquisition [46]. The magnitude of the Tx signal was set to 20 V_{peak} and the frame rate of the imaging system was ~9 Hz, compatible with the speed of motion of the OME-U. The real-time generated B-scans or 2D microUS images were transmitted over ROS and post-processed using logarithmic time gain compensation (TGC) for improved contrast.

In vivo Trials for Roll and Sweep

The trials were conducted on a 39 kg pig under general anesthesia at the Large Animal Experimental Facility, University of Leeds. These trials were carried out under Project Licence PC71ADE55, approved by the University of Leeds (establishment license number XDE639D76) in compliance with the Home Office (UK) legislation, the Animal (Scientific Procedures) Act 1986, and NC3Rs guidelines. This report adheres to the ARRIVE

guidelines.

After cleaning the colon through multiple rounds of enema, the OME was inserted through the rectum into the colon and advanced to about 20 cm beyond the rectum. This distance provided a long, straight region of the bowel for experimentation. The OME was followed with a standard endoscope (Olympus PCF-160AL) to render rear visualization of the OME and surrounding tissue. The ancillary elements of the OME were used for distension of the colon and irrigation when necessary.

The main objectives of these trials were to demonstrate that the OME can be successfully manipulated in the roll direction in vivo and that it can perform clinically applicable motions for contact-based sensing. Two experiments were designed to provide proof. The first consisted in a sweeping motion across the upper half of the colon surface, and the second involved a pure rolling motion within a $\pm 50^{\circ}$ roll. Each experiment was repeated five times. After the experiments were completed, the OME was removed by pulling it from its soft tether. Then, the standard endoscope was used to scan the colon surface to assess damage, with no evidence observed.

Contact Detection

To enable autonomous sweeping, a contact detection algorithm (see Supplementary Methods) was developed to assess the quality of contact between the microUS array and the tissue. This evaluation was crucial for the control loop that ensured continuous imaging by compensating for any loss of contact during sweeping.

For precise contact detection, microUS images underwent initial cropping to isolate a specific "zone of interest". This zone typically encompassed the region from 0% to 7% of the image depth, where differences indicative of contact versus no contact were most discernible. These differences were particularly noticeable due to an increase in high-intensity reverberations near the array's surface when the device was not in contact with the tissue, a phenomenon caused by the large difference in acoustic impedance between the array material and air.

By extracting the maximum value from each column in the microUS image, corresponding to one of the 32 microUS array elements, and applying binary thresholding, the system computed an average contact value ranging from 0 ("decoupled") to 1 ("coupled"). The algorithm represented the detected coupling quality through a color-coded bar overlaid on the microUS image (Figure A.7). This bar offered immediate feedback by transitioning from green, indicating good coupling, to red, indicating poor coupling, thus visually conveying the level of contact to the operator.

Given the variation in contact quality across different testing surfaces, such as silicone phantoms and in vivo mucosal tissue, calibration was necessary to determine the exact "zone of interest" and the appropriate threshold levels for the contact value. This calibration process involved performing a sequence of five coupling-decoupling repetitions to establish these critical parameters. Adjustments were based both on the observed differences in the microUS images and the contact value output.

Autonomous Sweeping

The autonomous sweeping algorithm consisted of three stages: initialization, contact recovery and execution of a pre-planned sweeping motion. Initialization set the correct frame of reference ($\mathbf{R}_D$) for the sweep motion, accommodating the variable orientation of the colon in vivo, which cannot be predetermined without supplementary imaging such as CT scans. Using the localization system and WLI, the operator positioned the OME-U centrally within the lumen before beginning the sweep, thereby establishing an initial reference frame relative to the global frame.

Once initialized, the algorithm checked the contact quality between the array and the tissue. If the contact was insufficient, the algorithm entered a contact recovery mode, applying magnetic torque about the tilt axis to improve proximity to the GI wall. Once adequate contact was achieved, the OME-U proceeded with the pre-planned sweeping motion, which involved a combination of horizontal translation and roll. This motion continued as long as contact remained adequate; if not, the algorithm reverted to contact recovery mode. This autonomous strategy, leveraging the oloid shape, WLI, robotic

adjustments, and the microUS array feedback, enabled consistent, high-quality imaging of the colon wall. Benchtop validation of the autonomous sweeping is detailed in Figures S6, S7, and Supplementary Methods.

3D Reconstruction

Using the 2D microUS images acquired from the autonomous sweep of the porcine colon with the OME-U, a 3D visualization of the scanned colon section was created. A custom MATLAB script was developed to extract robot positional information corresponding to each image in the dataset, ensuring precise spatial alignment during reconstruction. This process entailed iterating through all the images, reading each image in turn from the specified directory, and adjusting its position based on the corresponding robot position. An interpolation was then used to fill the gaps in the 3D projection of the image stack. Detailed steps are provided in Figure A.9 and Supplementary Methods.

By adjusting thresholds, specific pixel intensities were targeted to generate an isosurface, which is a 3D surface representation of points with equal values (isovalue) in a 3D intensity volume. The isovalue could be easily adjusted by the user to suit different scenarios and enhance visualization. For the results illustrated in Figure 3.8, using the same isovalue in both the cases, greatly emphasized the depiction of the polyp in Figure 3.8D.

An analysis was conducted to assess the accuracy and reliability of the reconstructed tissue volume (see Figure A.10 and Supplementary Methods). Metrics such as spatial fidelity and volumetric accuracy were evaluated to quantify the performance of the reconstructed polyp. Spatial fidelity was established during the benchtop phantom trial, where all measurements were controlled. The OME-U was fixed to a motor and rotated at a constant speed while maintaining constant contact with the silicon phantom. Ensuring a constant speed allowed for a reconstruction where the voxels have the same size, validating the algorithm's ability to reconstruct volumes and assess its precision by comparing the obtained dimensions of known high-echogenicity elements included in the phantom. These experiments determined the accuracy of the spatial reconstruction across different trials.

The spatial resolution of the 3D scan reconstruction depended on the image resolution along the x and y axes, and the accuracy of localization along the z-axis, as shown in Figure 3.8, which was influenced by the differences between successive OME-U pose values. Volumetric accuracy was assessed by reconstructing the inner volume of the polyp after characteristic feature extraction and comparing it with the volume of the solution injected to create the polyp. Once the features were extracted from the reconstructed volume, it became possible to save them and process this information in the form of a 3D object. From this, the contents could be extracted by subtraction to determine the volume contained in the polyp, which was then compared to the actual volume.

References

[1] G. Pittiglio, J. H. Chandler, T. da Veiga, *et al.*, "Personalized magnetic tentacles for targeted photothermal cancer therapy in peripheral lungs," en, *Communications Engineering*, vol. 2, no. 1, pp. 1–13, Jul. 2023, ISSN: 2731-3395. DOI: 10.1038/s44172-023-00098-9. [Online]. Available: https://www.nature.com/articles/s44172-023-00098-9.

[2] R. Dreyfus, Q. Boehler, S. Lyttle, *et al.*, "Dexterous helical magnetic robot for improved endovascular access," en, *Science Robotics*, vol. 9, no. 87, eadh0298, Feb. 2024, ISSN: 2470-9476. DOI: 10.1126/scirobotics.adh0298. [Online]. Available: https://www.science.org/doi/10.1126/scirobotics.adh0298.

[3] J. C. Norton, P. R. Slawinski, H. S. Lay, *et al.*, "Intelligent magnetic manipulation for gastrointestinal ultrasound," *Science Robotics*, vol. 4, no. 31, eaav7725, Jun. 2019. DOI: 10/gjpgdc. [Online]. Available: https://www.science.org/doi/10.1126/scirobotics.aav7725.

[4] N. G. Kim, N. J. Greenidge, J. Davy, *et al.*, "External Steering of Vine Robots via Magnetic Actuation," *Soft Robotics*, Sep. 2024, ISSN: 2169-5172. DOI: 10.1089/soro.2023.0182. [Online]. Available: https://www.liebertpub.com/doi/abs/10.1089/soro.2023.0182.

[5] M. Mattille, Q. Boehler, J. Lussi, N. Ochsenbein, U. Moehrlen, and B. J. Nelson, "Autonomous Magnetic Navigation in Endoscopic Image Mosaics," en, *Advanced Science*, vol. 11, no. 19, p. 2 400 980, 2024, ISSN: 2198-3844. DOI: 10.1002/advs.202400980. [Online]. Available: https://onlinelibrary.wiley.com/doi/abs/10.1002/advs.202400980.

[6] C. Spada, S. Piccirelli, C. Hassan, *et al.*, "AI-assisted capsule endoscopy reading in suspected small bowel bleeding: A multicentre prospective study," English, *The Lancet Digital Health*, vol. 6, no. 5, e345–e353, May 2024, ISSN: 2589-7500. DOI: 10.1016/S2589-7500(24)00048-7. [Online]. Available: https://www.thelancet.com/journals/landig/article/PIIS2589-7500(24)00048-7/fulltext.

[7] J. J. Abbott, E. Diller, and A. J. Petruska, "Magnetic Methods in Robotics," *Annual Review of Control, Robotics, and Autonomous Systems*, vol. 3, no. 1, pp. 57–90, 2020. DOI: 10/gj3ts6. [Online]. Available: https://doi.org/10.1146/annurev-control-081219-082713.

[8] E. Diller, J. Giltinan, G. Z. Lum, Z. Ye, and M. Sitti, "Six-degree-of-freedom magnetic actuation for wireless microrobotics," *The International Journal of Robotics Research*, vol. 35, no. 1-3, pp. 114–128, Jan. 2016, ISSN: 0278-3649. DOI: 10/f7642k. [Online]. Available: https://doi.org/10.1177/0278364915583539.

[9] C. R. Thornley, L. N. Pham, and J. J. Abbott, "Reconsidering Six-Degree-of-Freedom Magnetic Actuation Across Scales," *IEEE Robotics and Automation Letters*, vol. 4, no. 3, pp. 2325–2332, Jul. 2019, ISSN: 2377-3766. DOI: 10.1109/LRA.2019.2902742.

[10] C. Xu, Z. Yang, and G. Z. Lum, "Small-Scale Magnetic Actuators with Optimal Six Degrees-of-Freedom," *Advanced Materials*, vol. 33, no. 23, p. 2 100 170, May 2021. DOI: 10.1002/adma.202100170.

[11] J. Giltinan and M. Sitti, "Simultaneous Six-Degree-of-Freedom Control of a Single-Body Magnetic Microrobot," *IEEE Robotics and Automation Letters*, vol. 4, no. 2, pp. 508–514, Apr. 2019, ISSN: 2377-3766. DOI: 10.1109/LRA.2019.2891080.

[12] A. J. Petruska, "Open-Loop Orientation Control Using Dynamic Magnetic Fields," en, *IEEE Robotics and Automation Letters*, vol. 5, no. 4, pp. 5472–5476, Oct. 2020, ISSN: 2377-3766, 2377-3774. DOI: 10.1109/LRA.2020.3009070. [Online]. Available: https://ieeexplore.ieee.org/document/9140356/.

[13] H. Wang, J. Cui, K. Tian, and Y. Han, "Three-degrees-of-freedom orientation manipulation of small untethered robots with a single anisotropic soft magnet," en, *Nature Communications*, vol. 14, no. 1, p. 7491, Nov. 2023, ISSN: 2041-1723. DOI: 10.1038/s41467-023-42783-5. [Online]. Available: https://www.nature.com/articles/s41467-023-42783-5.

[14] M. P. Kummer, J. J. Abbott, B. E. Kratochvil, R. Borer, A. Sengul, and B. J. Nelson, "OctoMag: An Electromagnetic System for 5-DOF Wireless Micromanipulation," *IEEE Transactions on Robotics*, vol. 26, no. 6, pp. 1006–1017, Dec. 2010, ISSN: 1941-0468. DOI: 10.1109/TRO.2010.2073030. [Online]. Available: https://ieeexplore.ieee.org/document/5595508.

[15] O. Erin, X. Chen, A. Bell, *et al.*, "Strong magnetic actuation system with enhanced field articulation through stacks of individually addressed coils," en, *Scientific Reports*, vol. 14, no. 1, p. 23 123, Oct. 2024, ISSN: 2045-2322. DOI: 10.1038/s41598-024-72615-5. [Online]. Available: https://www.nature.com/articles/s41598-024-72615-5.

[16] L. Song, Y. Dai, L. Wang, *et al.*, "Motion Control of Capsule Robot Based on Adaptive Magnetic Levitation Using Electromagnetic Coil," *IEEE Transactions on Automation Science and Engineering*, vol. 20, no. 4, pp. 2720–2731, Oct. 2023, ISSN: 1558-3783. DOI: 10.1109/TASE.2022.3201966. [Online]. Available: https://ieeexplore.ieee.org/document/9901490/?arnumber=9901490.

[17] Y. Huo, L. Yang, T. Xu, and D. Sun, "Design, Control, and Clinical Applications of Magnetic Actuation Systems: Challenges and Opportunities," en, *Advanced Intelligent Systems*, vol. 7, no. 3, 2025, ISSN: 2640-4567. DOI: 10.1002/aisy.202400403. [Online]. Available: https://onlinelibrary.wiley.com/doi/abs/10.1002/aisy.202400403.

[18] A. W. Mahoney and J. J. Abbott, "Five-degree-of-freedom manipulation of an untethered magnetic device in fluid using a single permanent magnet with application in stomach capsule endoscopy," en, *The International Journal of Robotics Research*, vol. 35, no. 1-3, pp. 129–147, Jan. 2016, ISSN: 0278-3649. DOI: 10.1177/0278364914558006. [Online]. Available: https://doi.org/10.1177/0278364914558006.

[19] K. Obstein, C. Landewee, J. Norton, *et al.*, "The Magnetic Flexible Endoscope: Phase 1 First-In-Human Trial," *Gastrointestinal Endoscopy*, 2024 DDW Abstract Issue, vol. 99, no. 6, Supplement, AB581, Jun. 2024, ISSN: 0016-5107. DOI: 10.1016/j.gie.2024.04.2659. [Online]. Available: https://www.sciencedirect.com/science/article/pii/S0016510724029183.

[20] J. W. Martin, L. Barducci, B. Scaglioni, *et al.*, "Robotic Autonomy for Magnetic Endoscope Biopsy," *IEEE Transactions on Medical Robotics and Bionics*, vol. 4, no. 3, pp. 599–607, Aug. 2022, ISSN: 2576-3202. DOI: 10.1109/TMRB.2022.3187028.

[21] K. Simon, "Colorectal cancer development and advances in screening," *Clinical Interventions in Aging*, vol. 11, pp. 967–976, Jul. 2016, ISSN: 1176-9092. DOI: 10/gm78hd. [Online]. Available: https://www.ncbi.nlm.nih.gov/pmc/articles/PMC4958365/.

[22] L. J. Sliker and G. Ciuti, "Flexible and capsule endoscopy for screening, diagnosis and treatment," eng, *Expert Review of Medical Devices*, vol. 11, no. 6, pp. 649–666, Nov. 2014, ISSN: 1745-2422. DOI: 10.1586/17434440.2014.941809.

[23] T. M. H. Gall, S. R. Markar, D. Jackson, A. Haji, and O. Faiz, "Mini-probe ultrasonography for the staging of colon cancer: A systematic review and meta-analysis," eng, *Colorectal Disease: The Official Journal of the Association of Coloproctology of Great Britain and Ireland*, vol. 16, no. 1, O1–8, Jan. 2014, ISSN: 1463-1318. DOI: 10.1111/codi.12445.

[24] H. Seifert, P. Fusaroli, P. G. Arcidiacono, *et al.*, "Controversies in EUS: Do we need miniprobes?" *Endoscopic Ultrasound*, vol. 10, no. 4, pp. 246–269, Aug. 2021,

ISSN: 2303-9027. DOI: 10.4103/EUS-D-20-00252. [Online]. Available: https://www.ncbi.nlm.nih.gov/pmc/articles/PMC8411553/.

[25] *ExactVu™ Micro-Ultrasound System - Exact Imaging.* [Online]. Available: https://www.exactimaging.com/exactvu-micro-ultrasound-system.

[26] R. Vassallo, T. A. Aleef, Q. Zeng, B. Wodlinger, P. C. Black, and S. E. Salcudean, "Robotically controlled three-dimensional micro-ultrasound for prostate biopsy guidance," en, *International Journal of Computer Assisted Radiology and Surgery*, vol. 18, no. 6, pp. 1093–1099, Jun. 2023, ISSN: 1861-6429. DOI: 10.1007/s11548-023-02869-3. [Online]. Available: https://doi.org/10.1007/s11548-023-02869-3.

[27] H. S. Lay, B. F. Cox, V. Seetohul, C. E. M. Démoré, and S. Cochran, "Design and Simulation of a Ring-Shaped Linear Array for Microultrasound Capsule Endoscopy," *IEEE Transactions on Ultrasonics, Ferroelectrics, and Frequency Control*, vol. 65, no. 4, pp. 589–599, Apr. 2018, ISSN: 1525-8955. DOI: 10/gnj47b.

[28] X. Wang, V. Seetohul, R. Chen, *et al.*, "Development of a Mechanical Scanning Device With High-Frequency Ultrasound Transducer for Ultrasonic Capsule Endoscopy," eng, *IEEE transactions on medical imaging*, vol. 36, no. 9, pp. 1922–1929, Sep. 2017, ISSN: 1558-254X. DOI: 10/gmxdk5.

[29] Y. I. Sobolev, R. Dong, T. Tlusty, J.-P. Eckmann, S. Granick, and B. A. Grzybowski, "Solid-body trajectoids shaped to roll along desired pathways," en, *Nature*, vol. 620, no. 7973, pp. 310–315, Aug. 2023, ISSN: 1476-4687. DOI: 10.1038/s41586-023-06306-y. [Online]. Available: https://www.nature.com/articles/s41586-023-06306-y.

[30] S. Jeon, "A sphericon-shaped magnetic millirobot rolling on a surface actuated by an external wobbling magnetic field," *AIP Advances*, vol. 7, p. 056 708, May 2017. DOI: 10/f99j7x.

[31] H. Dirnbock and H. Stachel, "The Development of the Oloid," *Journal for Geometry and Graphics*, vol. 1, Jan. 1997.

[32] A. Petruska and J. Abbott, "Optimal Permanent-Magnet Geometries for Dipole Field Approximation," *Magnetics, IEEE Transactions on*, vol. 49, pp. 811–819, Feb. 2013. DOI: 10.1109/TMAG.2012.2205014.

[33] M. Miyasaka and P. Berkelman, "Magnetic levitation with unlimited omnidirectional rotation range," *Mechatronics*, vol. 24, Apr. 2014. DOI: 10.1016/j.mechatronics.2014.02.001.

[34] M. J. Gora, M. J. Suter, G. J. Tearney, and X. Li, "Endoscopic optical coherence tomography: Technologies and clinical applications [Invited]," *Biomedical Optics Express*, vol. 8, no. 5, pp. 2405–2444, Apr. 2017, ISSN: 2156-7085. DOI: 10.1364/BOE.8.002405. [Online]. Available: https://www.ncbi.nlm.nih.gov/pmc/articles/PMC5480489/.

[35] S. W. Yoo, G. Oh, A. M. Safi, *et al.*, "Endoscopic non-ablative fractional laser therapy in an orthotopic colon tumour model," en, *Scientific Reports*, vol. 8, no. 1, p. 1673, Jan. 2018, ISSN: 2045-2322. DOI: 10.1038/s41598-018-19792-2. [Online]. Available: https://www.nature.com/articles/s41598-018-19792-2.

[36] A. Bouakaz and J. Michel Escoffre, "From concept to early clinical trials: 30 years of microbubble-based ultrasound-mediated drug delivery research," en, *Advanced Drug Delivery Reviews*, vol. 206, p. 115 199, Mar. 2024, ISSN: 0169409X. DOI: 10.1016/j.addr.2024.115199. [Online]. Available: https://linkinghub.elsevier.com/retrieve/pii/S0169409X24000218.

[37] S. Hernot and A. L. Klibanov, "Microbubbles in ultrasound-triggered drug and gene delivery," *Advanced Drug Delivery Reviews*, Ultrasound in Drug and Gene Delivery, vol. 60, no. 10, pp. 1153–1166, Jun. 2008, ISSN: 0169-409X. DOI: 10.1016/j.addr.2008.03.005. [Online]. Available: https://www.sciencedirect.com/science/article/pii/S0169409X08000811.

[38] J. W. Martin, B. Scaglioni, J. C. Norton, *et al.*, "Enabling the future of colonoscopy with intelligent and autonomous magnetic manipulation," en, *Nature Machine Intelligence*, vol. 2, no. 10, pp. 595–606, Oct. 2020, ISSN: 2522-5839. DOI: 10/gm79tx. [Online]. Available: https://www.nature.com/articles/s42256-020-00231-9.

[39] P. Valdastri, M. Simi, and R. J. Webster, "Advanced Technologies for Gastrointestinal Endoscopy," *Annual Review of Biomedical Engineering*, vol. 14, no. 1, pp. 397–429, 2012. DOI: 10.1146/annurev-bioeng-071811-150006. [Online]. Available: https://doi.org/10.1146/annurev-bioeng-071811-150006.

[40] A. Wilson and B. P. Saunders, "Position change during colonoscopy: The oldest and best trick in the book," English, *Gastrointestinal Endoscopy*, vol. 82, no. 3, pp. 495–496, Sep. 2015, ISSN: 0016-5107, 1097-6779. DOI: 10.1016/j.gie.2015.03.1987. [Online]. Available: https://www.giejournal.org/article/S0016-5107(15)02313-5/fulltext.

[41] K. L. Andersson, J. B. Ha, D. R. Abraczinskas, E. J. Campbell, and J. M. Richter, "Gender Differences in Colonoscopy: Implications for Clinical Practice and Female Gastroenterologists," eng, *Digestive Diseases and Sciences*, vol. 67, no. 3, pp. 810–816, Mar. 2022, ISSN: 1573-2568. DOI: 10.1007/s10620-021-07079-y.

[42] I. Hiroshi, *The Development of the Two-Circle-Roller in a Numerical Way*, 2011. [Online]. Available: http://ilabo.bufsiz.jp/Development/2c-english.pdf.

[43] A. S. Kuleshov, M. Hubbard, D. L. Peterson, and G. Gede, "On the motion of the Oloid toy," en, in *XXXIX International Summer School–Conference APM 2011*, 2011, p. 8.

[44] A. Z. Taddese, P. R. Slawinski, M. Pirotta, E. De Momi, K. L. Obstein, and P. Valdastri, "Enhanced real-time pose estimation for closed-loop robotic manipulation of magnetically actuated capsule endoscopes," en, *The International Journal of Robotics Research*, vol. 37, no. 8, pp. 890–911, Jul. 2018, ISSN: 0278-3649. DOI: 10/gd5k9x. [Online]. Available: https://doi.org/10.1177/0278364918779132.

[45] T. L. Szabo, "10 - Imaging Systems And Applications," en, in *Diagnostic Ultrasound Imaging*, ser. Biomedical Engineering, T. L. Szabo, Ed., Burlington: Academic Press, Jan. 2004, pp. 297–336, ISBN: 978-0-12-680145-3. DOI: 10.1016/B978-012680145-3/50011-6. [Online]. Available: https://www.sciencedirect.com/science/article/pii/B9780126801453500116.

[46] A. C. Moldovan, B. Abaravičius, S. Mitra, and S. Cochran, "Power Consumption Considerations for Ultrasound Capsule Endoscopy," in *2023 IEEE International Ultrasonics Symposium (IUS)*, Montreal, QC, Canada: IEEE, Sep. 2023, pp. 1–4, ISBN: 9798350346459. DOI: 10.1109/IUS51837.2023.10306773. [Online]. Available: https://ieeexplore.ieee.org/document/10306773/.

3.6 Evaluation and Summary of Findings

This chapter presents the development and evaluation of an OME designed for autonomous, high-resolution ultrasound imaging in the GI tract. Building on the previous chapter, a closed-loop control scheme was established for the magnetic control of the roll of the oloid shape and validated across a range of surfaces. This enabled the integration of a 28 MHz microUS array into the OME, supporting autonomous closed-loop sweeping and 3D imaging, as demonstrated in both in vitro and in vivo settings. The OME achieved real-time, non-invasive 3D virtual biopsies and subsurface lesion detection, showcasing its ability to consistently maintain optimal tissue contact using the contact detection algorithm. In addition, the OME outperformed the cylindrical MFE in independent roll, tilt, and yaw maneuvers, demonstrating an improvement in overall dexterity for magnetic endoscopes achieved with only five magnetic control inputs.

The sensor-agnostic nature of the system lays a robust foundation for incorporating advanced imaging modalities such as OCT or terahertz in future work, which will drive the development of optimized contact and force-sensing strategies to match emerging technologies. Additionally, although the current device size is determined by commercially available microUS arrays, this presents a promising avenue for miniaturization through the creation of custom, flexible arrays, enabling even broader diagnostic and therapeutic applicability throughout the GI tract.

While future directions may include the application of this concept to wireless capsule platforms for diagnostic applications, the development and refinement of tethered magnetic endoscopes remain highly relevant, as they allow for the delivery of therapeutic

interventions as well as diagnostic procedures. However, as discussed in the introduction, all tethered systems suffer from the friction and drag imposed by the tether, which restricts the depth and reach of navigation, especially in complex anatomy.

The next chapter addresses these depth and friction challenges by introducing magnetically controlled vine robots, which is a novel approach to endoluminal navigation. Inspired by the tip-growing motion of climbing plants, this approach eliminates the buildup of friction and tether drag observed in conventional designs. This chapter details a 25 mm diameter vine robot integrated with the MFE, achieving controlled steering while maintaining shear-free navigation.

Chapter 4

Tip-growing Magnetic Flexible Endoscopes

Chapter source: N. G. Kim*, **N. J. Greenidge***, J. Davy, S. Park, J. H. Chandler, J. Ryu, P. Valdastri, 'External Steering of Vine Robots via Magnetic Actuation', Soft Robotics (Vol. 12, No. 2), pp.159 - 170. Copyright 2024, Mary Ann Liebert, Inc., publishers., DOI: 10.1089/soro.2023.0182. [2]

* N. G. Kim and N. J. Greenidge are to be considered co-first authors on this work. However, N. J. Greenidge is to be considered as the lead author due to the contributions listed in the "Intellectual Property and Publication Statements" section of this dissertation.

4.1 Abstract

This paper explores the concept of external magnetic control for vine robots to enable their high curvature steering and navigation for use in endoluminal applications. Vine robots, inspired by natural growth and locomotion strategies, present unique shape adaptation capabilities that allow passive deformation around obstacles. However, without additional steering mechanisms, they lack the ability to actively select the desired direction of growth. The principles of magnetically steered growing robots are discussed,

and experimental results showcase the effectiveness of the proposed magnetic actuation approach. We present a 25 mm diameter vine robot with integrated magnetic tip capsule, including 6 DoF localization and camera and demonstrate a minimum bending radius of 3.85 cm with an internal pressure of 30 kPa. Furthermore, we evaluate the robot's ability to form tight curvature through complex navigation tasks, with magnetic actuation allowing for extended free-space navigation without buckling. The suspension of the magnetic tip was also validated using the 6 DoF localization system to ensure that the shear-free nature of vine robots was preserved. Additionally, by exploiting the magnetic wrench at the tip, we showcase preliminary results of vine retraction. The findings contribute to the development of controllable vine robots for endoluminal applications, providing high tip force and shear-free navigation.

4.2 Introduction

Inspired by the growth and locomotion strategies of climbing plants observed in nature [1], [2], vine robots possess a unique ability to adapt their shape, to passively deform around obstacles and navigate complex environments, making them highly versatile for various applications. Their utility has been considered for application to medical procedures [3]–[5], exploration [6], and environmental monitoring [7].

Vine robot growth is typically driven by pneumatic actuation, where pressurization of an inverted inflatable cylinder causes internal material to be continuously transported and inflated at the tip, resulting in lengthening of the robot's body. This growth mechanism (extension from the tip), as opposed to translational motion, mitigates friction with the surrounding environment, therefore allowing the robot to move without drag. Furthermore, this mechanism for growth enables the robot to adapt to existing channels, facilitating gentle navigation within the environment [7]. However, vine robots operating in open space and without any additional steering mechanism lack the ability to control tip position and orientation, and thus growth direction. Therefore, the development of steering mechanisms to facilitate this capability while preserving the unique properties

of the vine robot represents a significant research challenge.

To address this issue, conventional approaches to steering vine robots have relied on embedding actuation systems throughout their bodies, such as Series Pneumatic Artificial Muscles (sPAMs) [8], [9], Fabric Pneumatic Artificial Muscles (fPAMs) [10], and tendon-driven actuation [11]. Fluidic approaches typically offer moderate distributed actuation along the length of the robot's body, realizing integrated designs with limited curvatures. Conversely, tendon-driven approaches can typically achieve higher curvatures, however, suffer from buckling and challenges due to tendon friction when the robot encounters consecutive bends.

As an alternative to whole-body actuation methods, tip-focused steering has been explored using rigid mechanisms that steer only the tip of the robot. This approach enables the robot to achieve higher curvature than the conventional whole-body steering, which is particularly useful for operating within small spaces. For example, a vine with an additional internal pneumatic bending mechanism was used to navigate a vine robot in a confined space [12], a hybrid vine robot was developed to induce buckling via an internal rigid steering mechanism to achieve high bending angles at discrete points along its length [13], and a rolling contact-based tip steering mechanism was proposed for improved target reachability [14].

Until now, the forces that trigger the steering of vine robots have been grounded within the robot itself, requiring the integration of additional mechanisms. Moreover, mounting and maintaining components at the robot's tip represents a unique challenge for vine robots due to their everting nature, typically necessitating either a rigid cap-like mount [15], internal pneumatic mechanisms [16] or a complicated control process [17]. Achieving tip-steering or stable tip mounts in vine robots has therefore come at the cost of having to include mechanisms that occupy significant space within the vine, interfere with their compliant nature, limit miniaturization potential and increasing the overall mechanical complexity of the system. In this paper, we investigate for the first time the concept of external actuation of the tip of a vine robot through magnetically induced torques and

forces.

By integrating a magnetic element into the structure of the robot and manipulating the external field, forces and torques can be induced on the robot's body. This principle has been proposed for use in medical applications such as tethered endoscopic navigation of the GI tract [18], and in soft magnetic catheters for navigation through the cardiovascular system [19] or the bronchial tree [20]. Conventional flexible endoscopes and catheters are all introduced into the human body by pushing them from the distal side. In order for them to advance inside a convoluted anatomy, they all have to apply pressure on the lumen wall whenever they approach a bend. This often leads to complications for the patient such as pain or perforations. Magnetic actuation facilitates designs that can conform better to the anatomy and can be deployed under open and closed loop control strategies using various localization methods. However, these methods suffer limitations due to their low actuation force and the build-up of friction during insertion [21].

The generation of actuating magnetic fields is possible via systems of electromagnetic coils [22] or the use of manipulated External Permanent Magnets (EPMs) [23], [24]. The use of manipulated EPMs comes with the advantage of larger workspace, lower power requirements, but increased control complexity [23]. Relatively, systems based on electromagnets produce weaker fields for the same size system and require large external power supplies and cooling systems. However, control is simplified due to the linear relationship between produced field and applied current.

In this study, we explore the application of an EPM mounted to a 7 DoF robot manipulator to generate the magnetic fields required for tip steering a Magnet Vine Robot (MVR) (See Figure 4.1), building on our previous work on magnetically manipulated flexible endoscopes with 6 DoF real-time tip localization[18]. By introducing a novel mounting system, we allow for the secure placement of a magnetic element at the robot's tip during eversion, enabling the robotically controlled EPM to induce the desired forces and torques required for precise tip navigation. This MVR approach aims to overcome the limitations of current vine robot steering techniques and allow the compliant, shear-free

growing nature of vine robots to be harnessed for improved navigation in delicate environments like endoluminal anatomies (e.g. the gastrointestinal tract, the bronchial tree or the cardiovascular system).

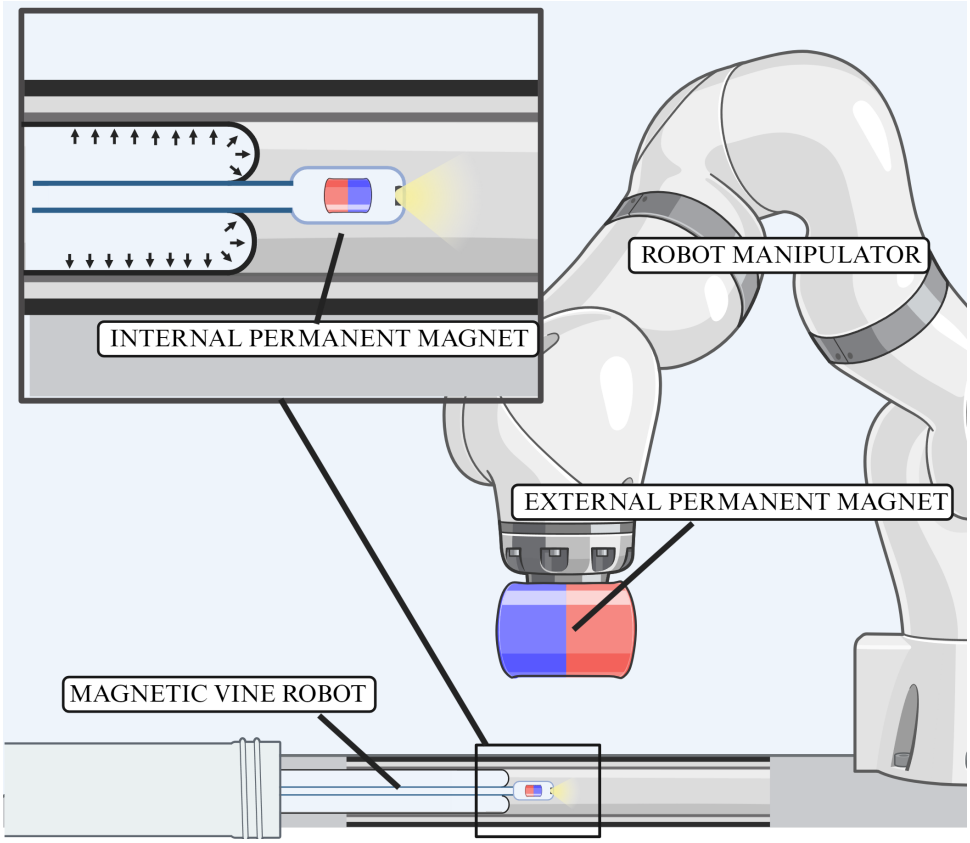

Figure 4.1: Overview of the proposed system. The robot consists of a growing section with a tip containing an IPM. By manipulation of the magnetic field via a large EPM mounted to a robotic manipulator, the growing robot can be steered without complex internal mechanisms. (created with Biorender.com)

We investigate the capability of magnetic actuation to facilitate high-curvature, tip-focused steering and independent tip orientation of vine robots without relying on complex internal mechanisms. Further experimentation evaluates how the MVR's growing nature can effectively expand the workspace of magnetic endoluminal navigation with its enhanced axial pushing force and eliminate tether drag. Furthermore, we validate the reproducibility and repeatability of the control of the MVR, by studying deviation across multiple fixed trajectories. We also present magnetic tip suspension tests that demonstrate the MVR's maintained shear free motion despite the integration of a rigid component at the tip and a preliminary examination of retraction.

While in this work the magnetic field is generated by a robotic EPM, the proposed approach can be generalized to any method of magnetic actuation, provided sufficient magnetic field can be generated and controlled.

4.3 Materials and Methods

4.3.1 Principles of Magnetic Vine Robots

In this section, we explain the principles of MVRs. In particular, we discuss the mathematical fundamentals of magnetic manipulation in order to justify the design choices in the MVR hardware as-well as experimental setup. We also discuss the considerations of the vine portion and how this pressurized body affects the overall deformation of the robot. For simplicity, internal forces and gravity are omitted. We assume that the bending stiffness of the tether is negligible compared to that of the inflated vine, and we consider magnetic forces to act directly on the robot's tip.

The use of both magnetic and growing actuation compounds the large tip forward force provided by the growing system with the magnetic forces and torques (wrench) on a magnet within an external field [7], [24]. This combination of actuation methodologies enables the remote steering of MVRs though external magnetic field manipulation.

To realize this combined actuation method, we propose the introduction of an IPM at the tip of a pneumatically actuated vine robot. When operated within an external magnetic field, the IPM and thus the tip of the vine robot experiences magnetic forces and torques which can be used to steer the vine robot. To provide suitable external magnetic fields for positioning and steering, we manipulate the pose of an EPM around the vine robot's workspace. (See Figure 4.2).

The magnetic field $\mathbf{B}$ at a point $\mathbf{r}$ produced by an EPM with magnetic moment $\mathbf{m}_e$ is given as

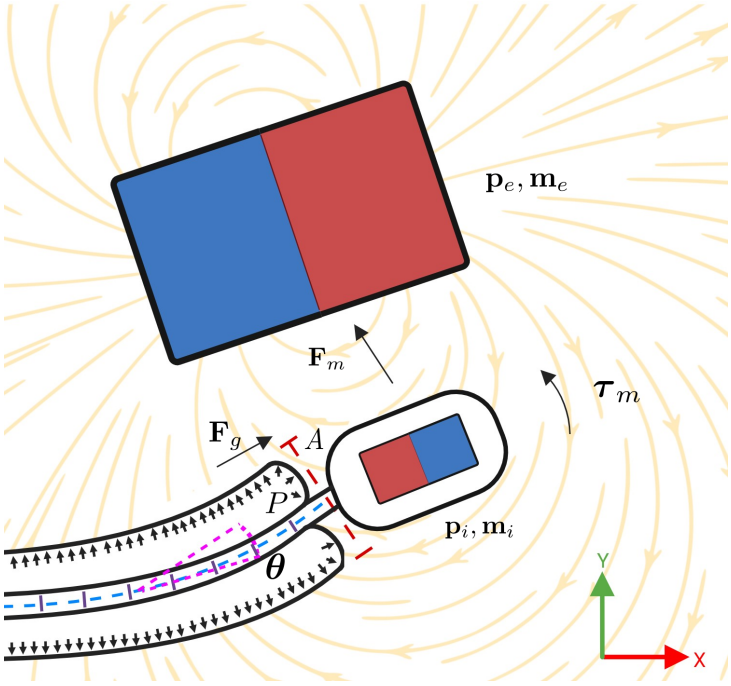

Figure 4.2: Diagram of contributing forces and torques to the movement of the robot. The total force is the sum of the pressurized growing section of the robot and the attractive force between EPM and IPM. The bending moment is a balance between the magnetic wrench of the IPM within the EPM's field and the restoration moment of the growing section. θ is the deflection of the vine body. (created with Biorender.com)

$$\mathbf{B}\left(\mathbf{m_e}, \mathbf{r}\right) = \left(\frac{\mu_\mathbf{0}}{\mathbf{4}\pi \parallel \mathbf{r} \parallel^{\mathbf{3}}} \left(\mathbf{3}\hat{\mathbf{r}}\hat{\mathbf{r}}^{\mathbf{T}} - \mathbf{I}\right)\right) \mathbf{m_e}, \tag{4.1}$$

where we consider $\mathbf{r} = \mathbf{p}_e - \mathbf{p}_i$, the relative displacement between the EPM position $\mathbf{p}_e$ and IPM position $\mathbf{p}_i$. $\hat{\mathbf{r}}$ is the direction vector of $\mathbf{r}$, $\hat{\mathbf{r}} = \frac{\mathbf{r}}{|\mathbf{r}|}$. $\mathbf{I}$ is the identity matrix and μ_0 is the vacuum permeability equal to $4\pi \times 10^{-7}$ Hm^{-1}.

The magnetic torque $\boldsymbol{\tau}_m$ on the IPM is

$$\boldsymbol{\tau}_m = \mathbf{m}_i \times \mathbf{B}. \tag{4.2}$$

$\mathbf{m}_i$ is the magnetic moment of the IPM equal to

$$\mathbf{m}_i = \frac{\mathbf{B}_r v}{\mu_0}, \tag{4.3}$$

where $\mathbf{B}_r$ is the residual magnetic flux density vector, v is the volume of magnetic material [23].

The spatial gradient of the EPM field is given as

$$\mathbf{B}_{\nabla}\left(\mathbf{m}_e\ ,\mathbf{r}\right) = \frac{3\mu_0}{4\pi\left\|\mathbf{r}\right\|^4}(\mathbf{m}_e\widehat{\mathbf{r}}^T + \widehat{\mathbf{r}}\mathbf{m}_e{}^T + \widehat{\mathbf{r}}^T\mathbf{m}_e\left(\mathbf{I} - 5\widehat{\mathbf{r}}\widehat{\mathbf{r}}^T\right)), \tag{4.4}$$

which relates to the magnetic force on the IPM $\mathbf{F}_m$ as

$$\mathrm{F}_m = \mathbf{B}_{\nabla}{}^T\mathbf{m}_i. \tag{4.5}$$

The growing portion of the robot exerts a force on the tip due to the pressurized section of the robot. The pushing force under quasi-static conditions can be simplified:

$$F_g = \frac{1}{2}PA - C, \tag{4.6}$$

where P is the internal pressure of the vine robot, A is the cross-sectional area of the vine robot, and C is a drag term related to material deformation, tip velocity etc. Details can be found in the work of Blumenschein et al. [25].

The inflated vine body, creates a restoration moment $\boldsymbol{\tau}_g$ which is a non-linear function of the diameter of the vine D , deflection angle $\boldsymbol{\theta}$ and P the internal pressure $\boldsymbol{\tau}_g{=}f(\boldsymbol{\theta},\ P, D)$. Other smaller factors that affect this restoration moment include vine material elasticity and tether tension.

The wrench of the MVR will therefore depend on the pose of the robot, the diameter of the vine, the applied pressure and the relative EPM- IPM pose. From Equations 4.1 to 4.5, it can be noted how magnetic torques and magnetic forces drop off with distance (i.e. $\frac{1}{\mathbf{r}^3}$ and $\frac{1}{\mathbf{r}^4}$, respectively). The overall tip force is the summation of the force contributions of the pressurized vine body and the magnetic force on the IPM (Equations 4.5 and 4.6).

In order to steer the vine body, the overall magnetic wrench applied must overcome the restoration moment introduced by the pressurized vine body. An IPM must therefore be selected with sufficient volume to generate the required wrench for the specific external magnetic actuation system used while fitting within the constraints of the overall MVR diameter.

4.3.2 Hardware of Magnetic Vine Robots

To achieve magnetic steering of vine robots, three main components are required. A magnetic tip, a system to generate and control an external magnetic field and a vine robot that allows for tip locking and tether feeding.

4.3.2.1 Magnetic Tip

The magnetic tip was constructed from a 20 mm x 35 mm 3D printed cylindrical clear resin shell (Formlabs) containing an 11 mm x 22 mm axially magnetized cylindrical NdFeB N52 permanent magnet (K&J Magnetics) wrapped in a flexible magnetic sensor array circuit for 6 DoF real-time localization ($\pm$2 mm position and $\pm3^\circ$ orientation accuracy) [18]. An endoscopic camera and LED were included to provide visual feedback from the tip, as well as a tool channel for passing tools down the tether (See Figure 4.3).

4.3.2.2 Magnetic Field Generation

For external magnetic field manipulation, a 101 mm x 101 mm NdFeB N52 EPM (Magnetworld AG) with a localization coil was mounted as the end effector of a 7- DoF serial robotic manipulator (14-kg payload, LBR, KUKA). Joint angles of the arm were controlled via a Cartesian joystick controller using ROS [21].

4.3.2.3 Vine Robot

The vine, and vine base were designed to allow the magnetic tip's sensor cable tether to be transported by utilizing a scrunched material stacking method, similar to the origami-inspired base developed by Kim et al. [17]. The notable improvements in our design

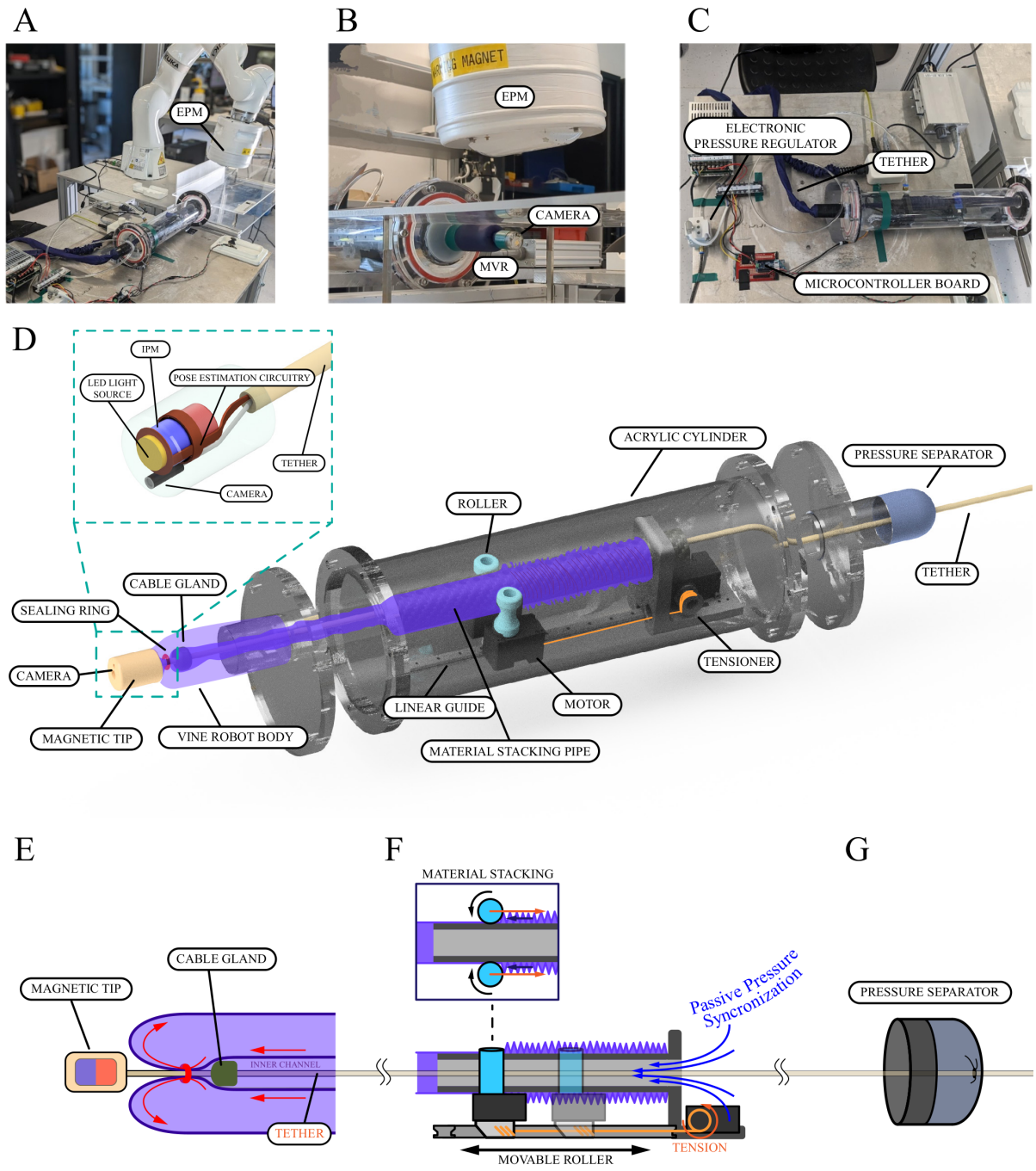

Figure 4.3: Hardware of the MVR. (A) Overview of the MVR system. (B) Vine robot with magnetic tip. (C) Electrical components. (D) CAD model of the MVR. (E) Schematic of the growing tip. (F) Schematic of the material stacking mechanism. (G) Schematic of the pressure separator.

include the integration of movable rollers, a pressure separator that facilitates the free transport of high gauge sensor wire into the pressurized base, and a sealing ring that continuously synchronizes internal pressure while locking the robot tip and facilitating

tether feeding.

As shown in Figure 4.3, the movable rollers are placed on a linear guide and pulled tight by a secondary tensioning motor. With sufficient tension pulling the linear guide, the material can be kept in a fully scrunched state. The fully stacked material just behind the roller then generates a pushing force, which automatically pushes the rollers forward during the stacking of the material. This configuration facilitates even vine material stacking across the stacking pipe allowing more material to be stacked in the same length of pipe without getting stuck just behind the roller.

The entire stacking system is placed in an acrylic cylinder with openings on both sides to pressurize the system. Placing an elastic sealing ring at the tip prevents air leakage and therefore continuously synchronizes the inner pressure with outer pressure for inner channel security. The vine base isolates the pressure inside the cylinder from the atmospheric pressure, while the high gauge cable can still freely move through via the pressure separator. The pressure separator is made of ripstop nylon to minimize friction between the separator and the tether, tightening the tether by elastic rubber built in the fabric.

By placing the sealing ring at the front tip and maintaining equal pressure levels between the inner channel and the main body, compression and, therefore, friction can be relieved to allow the wires to move freely inside the inner channel of the vine. The elastic sealing ring behind the magnetic tip allows the position of the magnetic tip to be maintained, preventing the spitting of the tip during growing. A cable gland prevents this elastic sealing ring from sliding down the tether during growing (See Figure 4.3E).

Figure 4.4 describes the fabrication of the inflatable vine robot body. The cylindrical shape was made by sewing Ripstop nylon fabric (Seattle Fabrics) and sealing it with silicone adhesive. A resulting diameter of 25 mm was achieved. The vine body's diameter is deliberately larger than that of the magnetic tip to ensure that the frictionless navigation aspect of vine locomotion can be retained.

To reduce the restoring moment that opposes magnetic actuation while the MVR tip is bending, we placed the fabric at a 45-degree angle when sewing it into a cylindrical

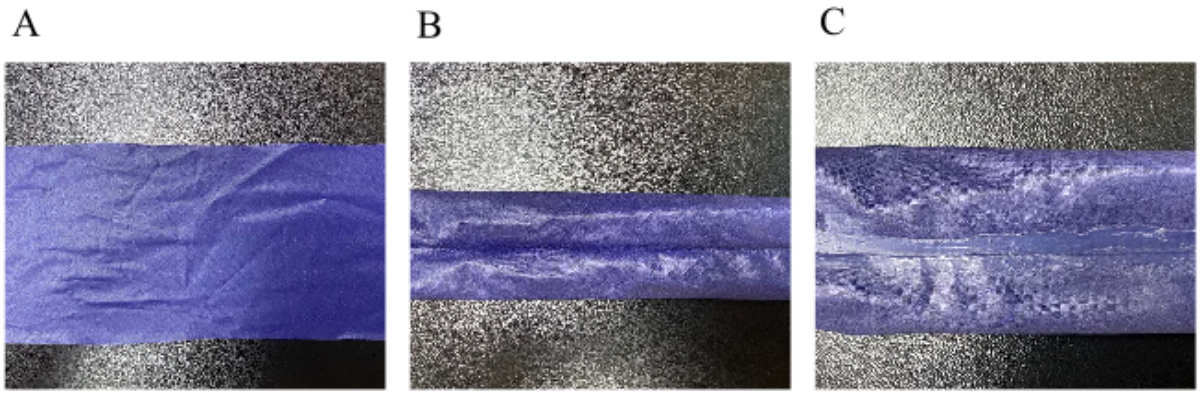

Figure 4.4: Fabrication of the growing body from Ripstop nylon fabric. (A) Fabric weave oriented at 45°. (B) Seam sewn. (C) Seam sealed with silicone adhesive.

shape. This orientation leverages the anisotropic stretchability of ripstop nylon, aligning it with the vine robot's principal axis and minimizing volume changes during curvature, thereby reducing the restoring moment [10]. Finally, to control the growth of the vine robot, the pressure was regulated using an electronic pressure regulator (SMC ITV-1010) and the rollers and tensioner were controlled using motors (Robotis Dynamixel XL330-M288-T). Both the motors and the electronic pressure regulator were controlled using a microcontroller (Robotis OpenRB-150).

4.4 Experimental Results

4.4.1 Tip Force Measurements

The resultant force at the tip of the MVR is a combination of the magnetic force between IPM and EPM and the growing force of the pressurized section. The magnetic force $\mathbf{F}_m$ is a function of the relative distance and orientation between IPM and EPM (Equation 4.4 and Equation 4.5), while the growing force $\mathbf{F}_g$ is a function of the applied pressure (Equation 4.6). To evaluate the relative contribution of each force, we varied the IPM-EPM separation distance at a range of static growing pressures. Figure 4.5A shows the experimental setup with the MVR constrained within a tube with an inner diameter matching the diameter of the MVR. The tip was placed against a force sensor (Nano 17, ATI Industrial Automation), and the EPM positioned above. Prior to each test,

the EPM was positioned at a starting height of 100 mm and a lateral distance of 85 mm relative to the MVR's tip magnet. The height of 100 mm was chosen as the lower limit of the clinically applicable range, informed by previous work showing an effective actuation range of 100 mm to 150 mm for applications such as colonoscopy [21]. The lateral distance of 85 mm was experimentally found through stepwise measurements to maximize tip force at the chosen height. The pressure was set to a fixed value for each test ranging from 0-30 kPa in steps of 5 kPa.

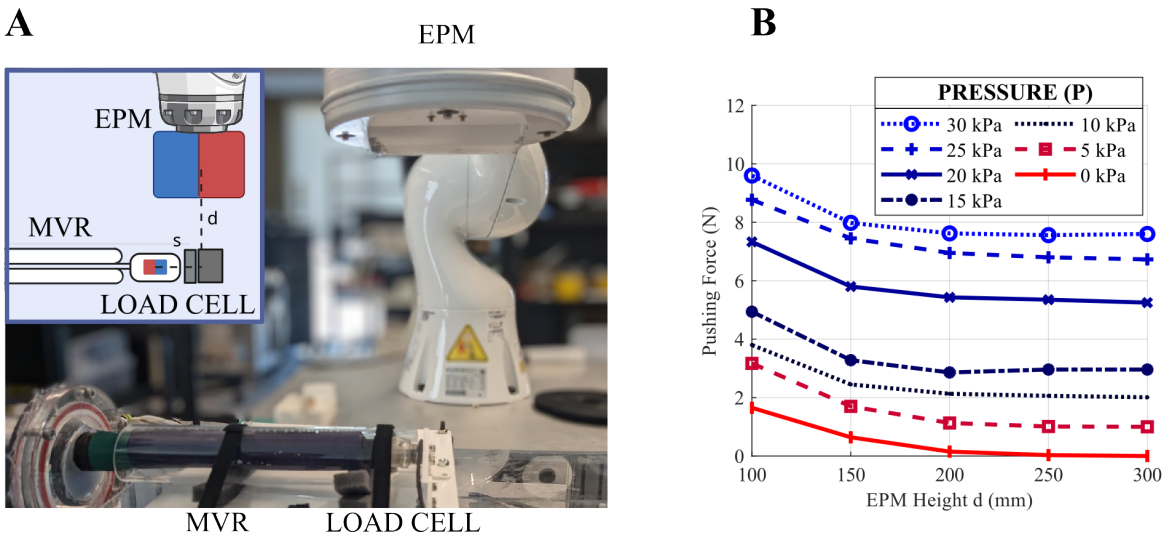

Figure 4.5: Tip force measurements. (A) Arrangement of MVR in the perspex tube with the load cell. (B) Graph of pushing force of MVR with varying pressure P and EPM height d.

At each pressure, the EPM height d was increased in steps of 50 mm up to a maximum height of 300 mm. At each height, the force on the load cell was observed over a period of 20 seconds and the mean value was recorded as the pushing force.

Figure 4.5B shows the average pushing force results as a function of EPM height at each pressure. It can be observed that pushing force converges with greater height of the EPM. The plateau reached at each pressure represents the respective contribution of growing force to the total pushing force. At higher pressures, the pushing force is dominated by the contribution of the growing portion. For example at 30 kPa, the growing force is 79 % of the overall force with an EPM height of 100 mm. As expected, at lower pressures the magnetic forces form a larger contribution, however, when EPM height is greater than 200 mm, the contribution is negligible.

4.4.2 Steering of MVR

In order to steer the MVR using magnetic actuation, the bending moment from the magnetic wrench must overcome the restoration moment of the growing section. To demonstrate this capability, we consider the maximal bending of the MVR that is achievable in free space using magnetic actuation.

The MVR was positioned in free space under a constraining plate to prevent contact between the EPM and the tip (See Figure 4.3B) and grown through an acrylic tube of similar diameter to constrain the proximal portion and allow control over its unconstrained grown length. The MVR was pressurized to 30 kPa and the separation between EPM and IPM height was set at 160 mm. As observed in the results of the tip force measurements, at this distance and pressure, the magnetic force contribution in the direction of travel is minimal. The MVR was subsequently grown until its unconstrained length, the length from the end of acrylic tube to the MVR tip, was 10 cm (Figure 4.6A) and 20 cm (Figure 4.6B) respectively. The EPM was then manipulated to achieve the minimum bending configuration of the MVR body without buckling. It can be observed that the MVR achieves a minimal bending radius of 4.95 and 3.85 cm in the 10 cm and 20 cm cases, respectively. It can also be observed how the MVR tip can still be steered independently of the bending of the growing section by rotation of the EPM, as indicated by the red arrows in Figure 4.6A and B. To show the ability of the MVR to achieve high (non-constant) curvature, the EPM was manipulated so that the MVR was bent beyond the point of buckling as shown in Figure 4.6C (See Supplementary Video 1) where the proximal constraint acts as a pivot point for the vine's body.

To study the repeatability of the bending control of the MVR using the EPM, we considered fixed circular trajectories of the EPM. Here, the EPM was positioned at a height of 160 mm and moved in a fixed circular trajectory with a radius equivalent to the MVR's length from 0 to 130 degrees. These tests were conducted over a range of pressures (P = 10.0 kPa, 20.0 kPa, 30.0 kPa) and robot lengths (l = 100 mm, 150 mm, 200 mm) with five repeats each. Starting from a straight pose, as the MVR is bent, it forms an approximate

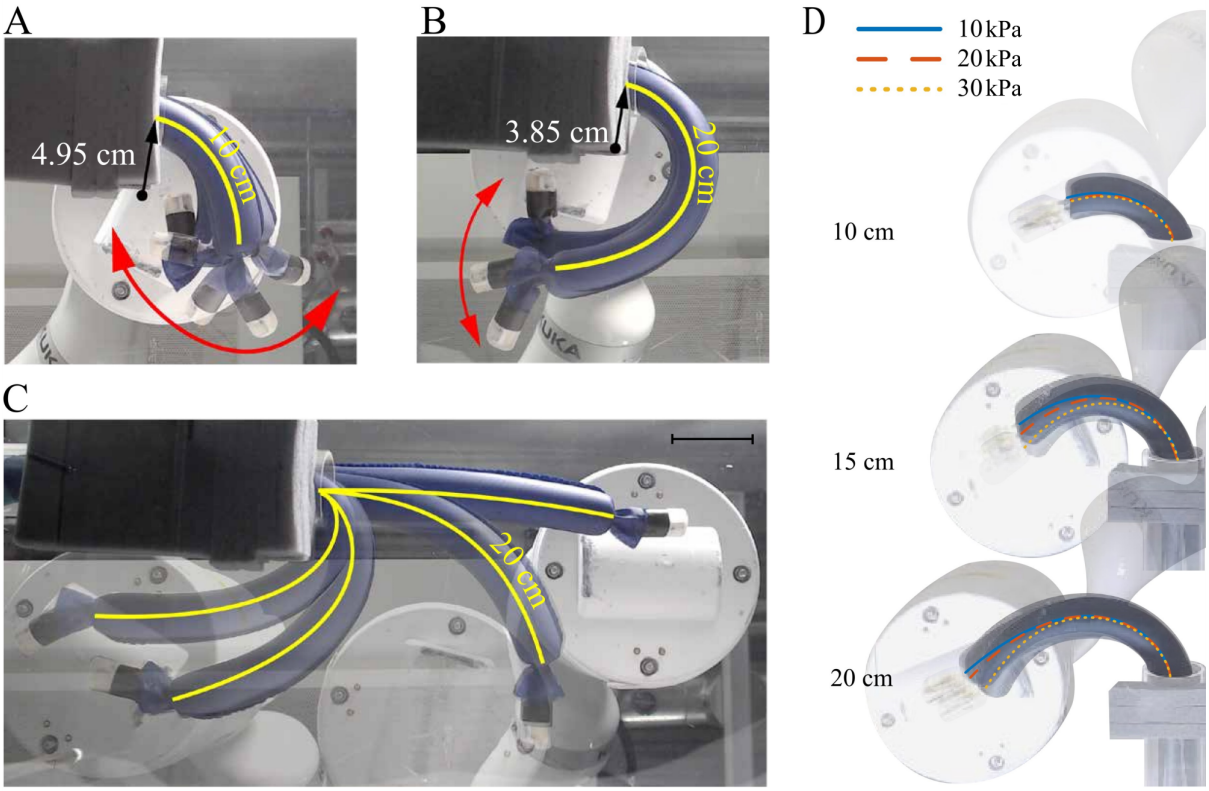

Figure 4.6: Magnetic steering of the MVR. (A) Minimum bending radius of 4.95 cm with 10 cm of grown body. (B) Minimum bending radius of 3.85 cm with 20 cm of grown body. (C) Demonstration of the ability to buckle the robot body even at a pressure of 30 kPa. (D) Repeatability of achieving bending radii under differing pressures and MVR lengths.

constant curvature which was quantified as a mean bending radius via image analysis (see Figure B.3, supplementary materials). Table 4.1 summarizes these results. It can be observed that bending radii is approximately constant and independent of applied pressure and robot length. This shows the dominance of the magnetic wrench over restoration torque within the vine body and the repeatability of the actuation methodology to achieve high curvature bending of the MVR (See Figure 4.6D).

4.4.3 Navigation with Suspended Tip

One of the characteristic behaviors of vine robots is the ability to locomote shear-free as a result of their everting nature. The inclusion of a magnetic tip for steering reintroduces a component which moves relative to the environment and therefore would be a source of friction when contact is maintained. To demonstrate the ability to suspend the magnetic

Table 4.1: Mean bending radii of the MVR's final position across a range of robot lengths and pressures under fixed circular EPM trajectories.

Robot Length (mm)	**Pressure (kPa)**	**Mean Bending Radius (mm)**	**Bending Radius Standard Deviation (mm)**
100	10.0	65.5	0.3
100	20.0	66.3	0.2
100	30.0	67.0	0.1
150	10.0	67.3	0.5
150	20.0	69.7	1.1
150	30.0	69.0	0.4
200	10.0	63.4	1.5
200	20.0	72.2	0.4
200	30.0	66.5	0.9

tip during growing and steering, the MVR was navigated around a 90-degree bend within a 60 mm diameter perspex tube, illustrated in Figure 4.7. Here, the EPM was positioned at a height of 160 mm and moved in a fixed pre-planned path in the x-y plane to follow the 90 degree bend. Five repetitions were conducted at two different EPM speeds of 3 mms^{-1} and 4 mms^{-1} under the fixed EPM trajectory. These speeds correspond to just 10% and 20% of the robotic manipulator's maximum speed and were chosen due to limitations in the experimental setup, specifically the manual pressure regulation. Although the robotic manipulator is capable of moving faster, these speeds allowed for the internal pressure to be adjusted, ensuring reliable and controlled navigation. Automating pressure regulation in future work will enable faster speeds to be achieved.

Figure 4.8A shows the 3D position data from the robot's localization system for three independent repetitions at each speed (see Figure B.2, supplementary materials for all five repetitions), and the EPM's pre-planned path demonstrating that the robot was repeatedly navigated through the 90-degree path at both speeds. Figure 4.8B shows the 2D top view of the x-y plane and Figure 4.8C shows the 2D projected view of the mean and standard deviation of the IPM's center in z (height) versus the distance travelled for each speed. Over five repetitions, an average gap of 11.2 ± 4.3 mm for 3 mms^{-1} and 12.8 ± 3.4 mm for 4 mms^{-1} was maintained between the edge of the magnetic tip and the

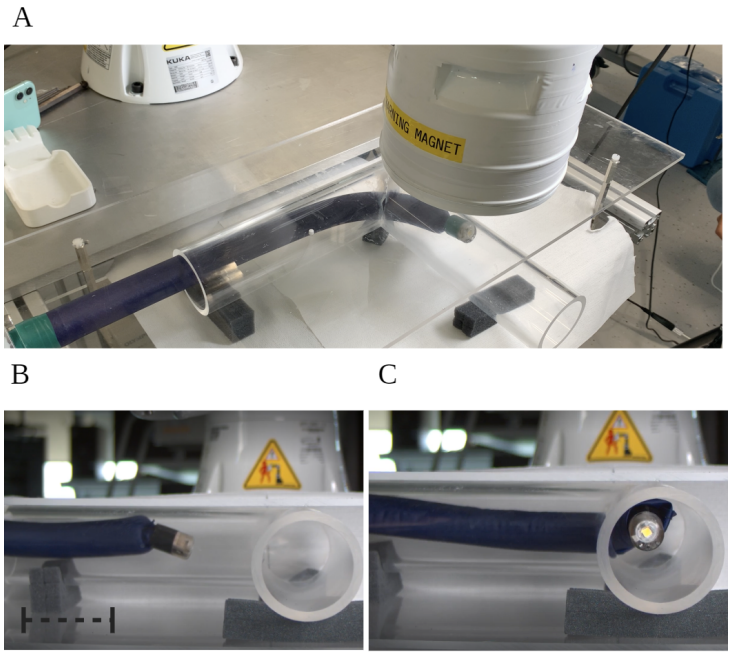

Figure 4.7: Setup of suspended tip experiment. The robot navigates through a 90-degree turn while keeping the tip suspended, preventing any interaction with the tip and the surrounding tubular environment. (A) Top view. (B) Side view in first half of the 90-degree turn. (C) Side view in the second half of 90-degree turn. Scale Bar: 5 cm.

upper surface of the perspex tube (See Supplementary Video 2). EPM- IPM coupling deviations in the x-y plane across all five repetitions for 3 mms^{-1} and 4 mms^{-1} were found to be 19.0 ± 2.8 *mm* and 19.6 ± 1.8 *mm* in x, 24.3 ± 3.6 *mm* and 21.0 ± 3.3 *mm* in y and $19.1 \pm 5.8°$ $22.3 \pm 10.3°$ in yaw respectively Deviations for each repetition can be found in Table B.1 of the Supplementary Materials. When the EPM is directly above and parallel to the tip magnet, no torque or force is generated in the lateral plane. These EPM- IPM coupling deviations are therefore necessary in order to generate the magnetic wrench required for steering the MVR.

4.4.4 Preliminary Results of Retraction using Magnetic Wrench

In the context of vine robots, retraction refers to the reversal of the growing process, where material inverts at the tip and the vine's length reduces. Without additional constraints on the robot motion however, retraction can fail due to an induced moment from the tensioned tether [26]. To compensate for this, several studies have considered how applying a *grounding force* to the tip can stabilize the vine body, allowing for successful

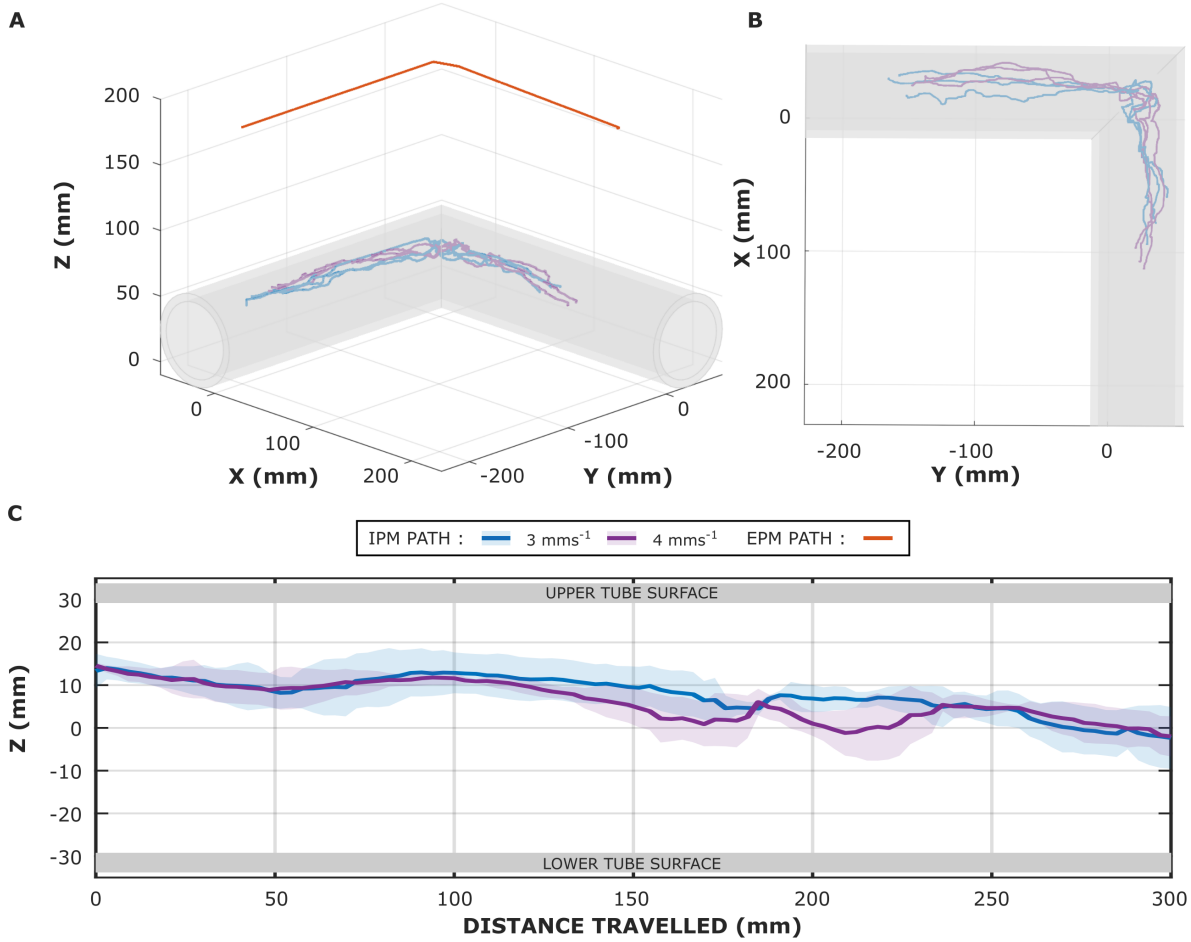

Figure 4.8: Suspended tip experiment data. (A) 3D position data of the center of the EPM and IPM for EPM speeds of 3 mms^{-1} and 4 mms^{-1} for three repetitions within the perspex tube. (B) 2D projected view of the IPM's position on the x-y plane. (C) 2D projected view of the mean and standard deviation of the IPM's z position (height) versus distance travelled along the perspex tube.

retraction. This force acts in opposition to the tether tension, stabilizing the vine body and therefore allowing the material to be inverted and eventually retracted into the robot base.

If such a force is not applied, the outer material of the robot may collapse first, or in the case of an inflated vine robot, buckling may occur. Buckling during retraction is established as an open problem in vine robots, as it would be desirable for the robot to exit the environment with the same non-shearing behavior as which it entered, particularly in delicate enviroments [27]. Due to vine robots' susceptibility to buckling during this process [27], we propose harnessing magnetic interaction to address this problem. Our

focus lies in utilizing magnetic wrench to counteract the buckling phenomenon caused by the pulling of the internal tether from the end of the robot.

To assess the feasibility of this approach, retraction was attempted on a high friction surface under four different conditions. The four scenarios are a deflated MVR with no EPM (Figure 4.9A), inflated MVR (3 kPa) with no EPM, (Figure 4.9B), deflated MVR with EPM (Figure 4.9C) and inflated MVR (3 kPa) with EPM (Figure 4.9D). In scenario 3 and 4 (Figure 4.9C&D), the EPM is positioned 60 mm above the magnetic tip and tracked above the tip position. For each retraction attempt, the MVR was first grown in its axial direction to a length of 320 mm and then retracted under manual control.

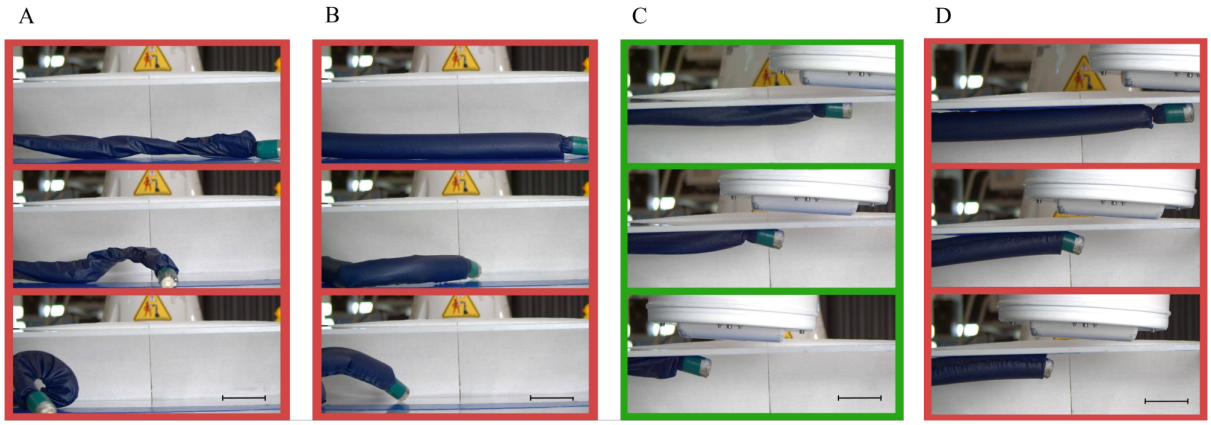

Figure 4.9: Experimental results of retraction under varying conditions. (A) Deflated MVR with no EPM. (B) Inflated MVR with no EPM. (C) Deflated MVR with EPM. (D) Inflated MVR with EPM. Case (C) highlighted green to indicate successful retraction. Scale bar: 5 cm.

In both of the "no EPM" cases (Figure 4.9A&B), absence of the EPM providing magnetic wrench led to rapid buckling of the body when the internal material was pulled for retraction (See Supplementary Video 3). In contrast, Figure 4.9C shows that the magnetic wrench generated by the EPM successfully prevented buckling, ensuring the retraction process proceeded smoothly. Interestingly, Figure 4.9D shows that while buckling did not occur, friction resistance occurred between the material and the tether at the tip, along with the resistance of the sealing ring as a result of the increased pressure, causing the tip to become engulfed occasionally. It is to be noted that, at EPM- IPM separations greater than 60 mm, the magnetic wrench was not sufficient to assist retraction in either case and therefore presentation of this experiment serves only as a preliminary result.

4.4.5 Demonstration of Navigating a Complex Environment

To evaluate the maneuverability of the MVR, an experiment in which the MVR was navigated using joystick control of the EPM through a complex path of length 0.5 m with consecutive sharp curves (Figure 4.10A) was conducted. The MVR was navigated through the maze, at which point tip steering was performed before proceeding along a linear trajectory in free space towards a designated target object.

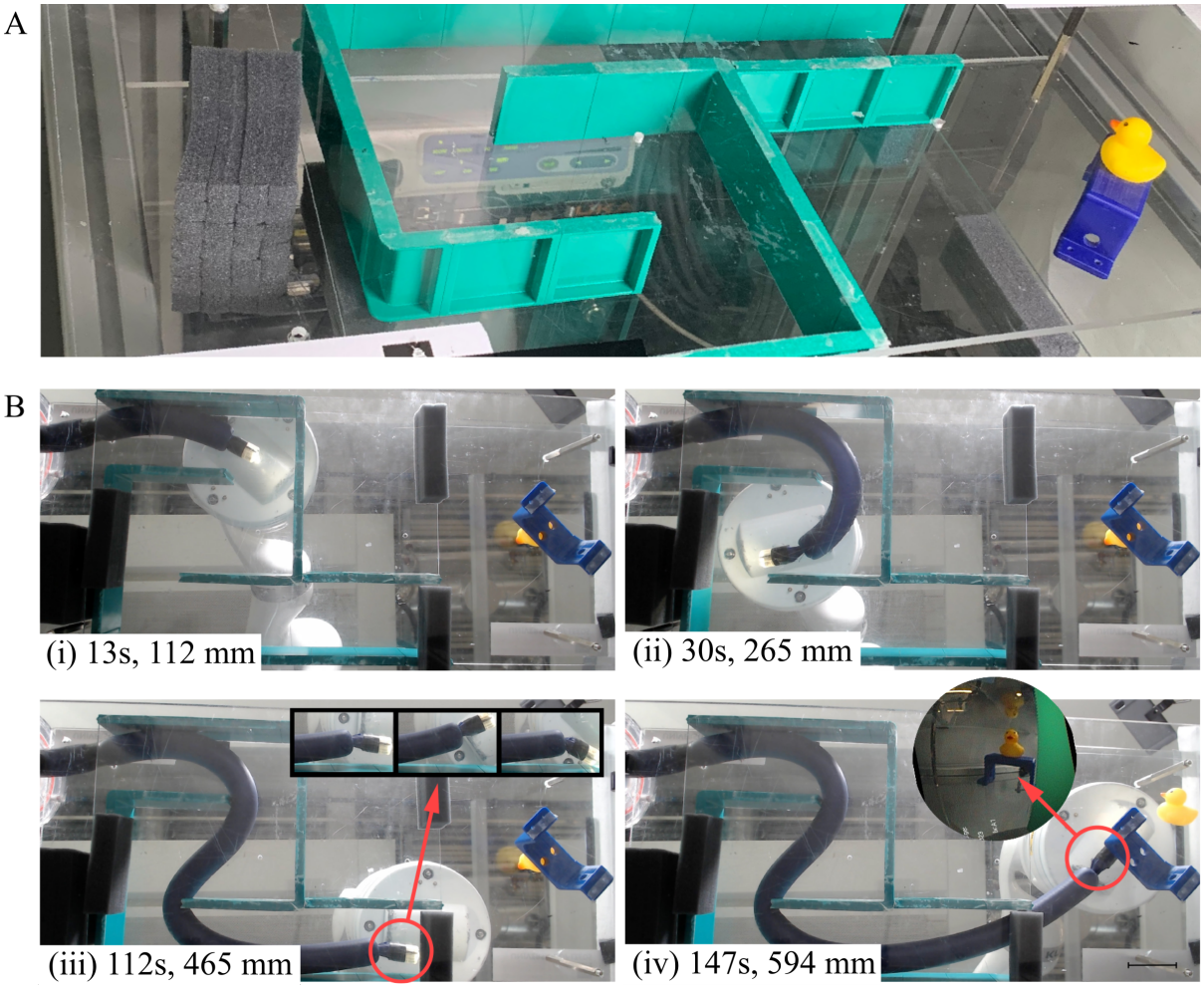

Figure 4.10: Demonstration of MVR navigating the maze environment reporting time and navigation distance. (A) Maze overview. (B) Tiled images of MVR navigating the maze, with the inset in (iii) showing isolated steering of MVR and the inset in (iv) showing the camera view from the MVR tip. Scale Bar: 5 cm.

Figure 4.10B illustrates the ability of the MVR to continue to grow as it successfully navigates through multiple sharp turns. Additionally, tip-concentrated steering of the MVR after negotiating two consecutive sharp turns is shown in the inset of Figure 4.10B(iii).

The inset of Figure 4.10B(iv) shows the camera's view as the MVR maintains visibility of the target object and direction whilst growing in a linear trajectory, ultimately reaching the target and knocking it off its pedestal. Over five successful repetitions, the average time to navigate the maze was 3 minutes and 15 seconds (See Supplementary Video 4).

4.5 Discussion and Conclusion:

In this work, we sought to advance vine robot technology by proposing an external magnetic tip steering mechanism, capable of inducing high curvatures in the MVR body whilst maintaining its compliant, shear-free growing nature. Building on our previous work in magnetic flexible endoscopy, this system forgoes complicated internal mechanisms, instead utilizing a sensorized magnetic tip to facilitate steering, localization and visual feedback. To enable this, we introduced a novel mounting system that not only ensures the secure attachment of the sensorized magnetic element at the MVR's tip during eversion but also provides a reliable method for allowing translation within the inner channel, facilitating seamless transition of sensor cables.

Our investigation of the pushing force of the MVR confirmed the independent influence of both magnetic and pneumatic contributions, with pneumatic contributions being the most significant. Critically, under magnetic manipulation, torque decays with a relationship of $1/r^3$ with the EPM-IPM distance, while force has the relationship $1/r^4$. This relationship highlights the ability of the MVR to be effectively controlled at larger EPM-IPM separation distances (compared to magnetic manipulation alone [21]), relying on magnetic torques for orientation control and pneumatic growing force for forward locomotion. This means that, although downward force is not directly controllable, in the case of MVRs in endoluminal applications, downward force may be achieved through the growing force of the vine while the magnetic torque assists with steering at higher EPM-IPM separation distances. The larger workspace afforded to the system can also seek to accommodate larger patients than would be possible with approaches relying on magnetic manipulation alone [21].

At the design scale evaluated, magnetic steering studies showed that magnetic actuation was found to be dominant over the restoring moment of the pressured section, allowing for high curvature bending of the vine as well as independent tip steering. This exemplifies our design's intent: to focus actuation at the tip while allowing the rest of the vine body to adapt its shape compliantly to the environment; achieving both constant curvature bending when unobstructed, which is dependent on the vine diameter and operating pressure (Figure 6A&B), and non-constant curvatures when bending around an obstruction or a constraint (Figure 6C). This feature is particularly useful in endoluminal scenarios, where adaptability to varying and confined spaces is crucial.

Although the presented MVR requires the addition of a small rigid component at its tip, we have shown that it is possible to suspend the tip during MVR navigation via the balance of magnetic forces and elasticity of the inflated vine body. This approach maintains the shear-free growing motion that is typical of vine robots. It also shows that by virtue of magnetic manipulation, when compared to other mechanisms [15] the weight of the tip is of less concern as it can be compensated for.

In previous work on magnetic robots for colonoscopy, magnetic levitation was used to prevent tissue interaction [28], but it required complex EPM control for gravity compensation and did not address tether drag. Our MVR design reduces harmful tissue interaction and tether drag through friction-free navigation, achieved by the growing vine body and tip suspension, with the tether remaining internal to the outer body. In addition, the soft nature of the growing body could provide a source of stabilization for tooling and for performing procedures such as tissue biopsies.

Addressing retraction challenges [7], our approach of using magnetic wrench was enough to successfully retract the robot in a straight line without buckling the growing body (Figure 9C). However, this method did rely on very close proximity of EPM and IPM and a high friction contact surface. Short EPM-IPM distances limit feasibility for medical applications although larger working distances may be realized by increasing the magnetic volume of the EPM and/or IPM.

The final demonstration of navigating a complex environment (Figure 10) showed that the eversion process is instrumental in facilitating the vine robot's navigation through tortuous environments by eliminating tether drag and enhancing the tip force applied to the magnetic tip. This is an improvement on traditional magnetic endoscopes which struggle to navigate deeper within the anatomy due to friction between the tether and the environment [21]. The maze navigation also highlights the MVR's ability to perform high curvature steering and to continue to grow at arbitrary vine lengths both around obstacles and in free space. In addition, the unique ability to orient the tip independent to the vine body is demonstrated and could be useful to adjust camera and tool orientations in a clinical setting. Although our experiments were conducted in an open-loop manner, our system's design presents a substantial opportunity for closed-loop vine robot control, utilizing our 6 DoF tip localization (shown in Figure 8) and visual servoing. This is supported by the low deviations observed across repetitions, highlighting the stability of the MVR behavior.

Compared to other vine robot steering mechanisms, such as tendon-driven or pneumatic muscles, our design enables high curvature, tip focused steering, and the unique ability to steer the tip independently of the vine body. The associated design simplicity, devoid of internal motorized components and rigid tip mounts, can enable smaller scales and inherent safety, which is conducive to medical applications like endoluminal navigation (e.g. gastrointestinal endoscopy, bronchoscopy or cardiovascular navigation), but is limited to scenarios amenable to external magnetic field generation. MVRs also retain the benefits of shear-free motion due to the combination of everting "growth" motion, which simply adds material at the tip to move forward, with the magnetic suspension of a short, rigid component at the tip that is smaller in diameter than the outer vine.

The collective features of MVRs can thus minimize the risk of complications for the patient associated with friction-based movement, offering a gentle and safe option for navigation within delicate biological structures. Additionally, the higher tip forces generated by the pneumatic component and elimination of tether drag may allow MVR's to navigate deeper into endoluminal anatomy than conventional magnetic endoscopes [21]

or catheters [23].

Although we have successfully demonstrated the feasibility of magnetic manipulation for vine robots, the general scalability of MVRs remains to be investigated. Magnetic manipulation systems have been successfully demonstrated at smaller scales, however with miniaturized MVRs with lower overall magnetic volume, it remains to be proven if steering of the pressurized body can still be achieved. A systematic design study would be required to evaluate the feasibility of the concept across multiple scales, as our current design was motivated by endoluminal applications (specifically for gastrointestinal endoscopy), where a camera, localization and tool channel are required.

Overall, our findings highlight the first successful integration of magnetic steering mechanisms into vine robots, expanding their dexterity while maintaining shear-free navigation for endoluminal applications. Future research will be directed towards enhancing the MVR's performance by implementing closed-loop control for visual servoing, tip suspension and retraction in complex environments. We aim to further validate our technology's practical utility in clinically relevant experiments, incorporating a larger magnetic volume to extend the EPM-IPM separation distance and improve retraction efficiency. We also aim to investigate the miniaturization potential for use in smaller lumens to extend our technology to a wider range of endoluminal applications.

References

[1] D. Mishima, T. Aoki, and S. Hirose, "Development of Pneumatically Controlled Expandable Arm for Search in the Environment with Tight Access," en, in *Field and Service Robotics: Recent Advances in Reserch and Applications*, S. Yuta, H. Asama, E. Prassler, T. Tsubouchi, and S. Thrun, Eds., Berlin, Heidelberg: Springer, 2006, pp. 509–518, ISBN: 978-3-540-32854-4. DOI: 10.1007/10991459_49. [Online]. Available: https://doi.org/10.1007/10991459_49.

[2] E. W. Hawkes, L. H. Blumenschein, J. D. Greer, and A. M. Okamura, "A soft robot that navigates its environment through growth," *Science Robotics*, vol. 2, no. 8,

eaan3028, Jul. 2017. DOI: 10.1126/scirobotics.aan3028. [Online]. Available: https://www.science.org/doi/10.1126/scirobotics.aan3028.

[3] P. Berthet-Rayne, S. M. H. Sadati, G. Petrou, *et al.*, "MAMMOBOT: A Miniature Steerable Soft Growing Robot for Early Breast Cancer Detection," *IEEE Robotics and Automation Letters*, vol. 6, no. 3, pp. 5056–5063, Jul. 2021, ISSN: 2377-3766. DOI: 10.1109/LRA.2021.3068676. [Online]. Available: https://ieeexplore.ieee.org/document/9387605.

[4] M. Li, R. Obregon, J. J. Heit, A. Norbash, E. W. Hawkes, and T. K. Morimoto, "VINE Catheter for Endovascular Surgery," *IEEE Transactions on Medical Robotics and Bionics*, vol. 3, no. 2, pp. 384–391, May 2021, ISSN: 2576-3202. DOI: 10.1109/TMRB.2021.3069984. [Online]. Available: https://ieeexplore.ieee.org/document/9392018.

[5] P. Valdastri, M. Simi, and R. J. Webster, "Advanced Technologies for Gastrointestinal Endoscopy," *Annual Review of Biomedical Engineering*, vol. 14, no. 1, pp. 397–429, 2012. DOI: 10.1146/annurev-bioeng-071811-150006. [Online]. Available: https://doi.org/10.1146/annurev-bioeng-071811-150006.

[6] J. Luong, P. Glick, A. Ong, *et al.*, "Eversion and Retraction of a Soft Robot Towards the Exploration of Coral Reefs," in *2019 2nd IEEE International Conference on Soft Robotics (RoboSoft)*, Apr. 2019, pp. 801–807. DOI: 10.1109/ROBOSOFT.2019.8722730. [Online]. Available: https://ieeexplore.ieee.org/document/8722730.

[7] M. M. Coad, L. H. Blumenschein, S. Cutler, *et al.*, "Vine Robots," *IEEE Robotics & Automation Magazine*, vol. 27, no. 3, pp. 120–132, Sep. 2020, ISSN: 1558-223X. DOI: 10.1109/MRA.2019.2947538. [Online]. Available: https://ieeexplore.ieee.org/document/8917931.

[8] J. D. Greer, T. K. Morimoto, A. M. Okamura, and E. W. Hawkes, "Series pneumatic artificial muscles (sPAMs) and application to a soft continuum robot," in *2017 IEEE International Conference on Robotics and Automation (ICRA)*, May 2017, pp. 5503–5510. DOI: 10.1109/ICRA.2017.7989648. [Online]. Available: https://ieeexplore.ieee.org/document/7989648.

[9] J. D. Greer, T. K. Morimoto, A. M. Okamura, and E. W. Hawkes, "A Soft, Steerable Continuum Robot That Grows via Tip Extension," en, *Soft Robotics*, vol. 6, no. 1, pp. 95–108, Feb. 2019, ISSN: 2169-5172, 2169-5180. DOI: 10.1089/soro.2018.0034. [Online]. Available: https://www.liebertpub.com/doi/10.1089/soro.2018.0034.

[10] N. D. Naclerio and E. W. Hawkes, "Simple, Low-Hysteresis, Foldable, Fabric Pneumatic Artificial Muscle," *IEEE Robotics and Automation Letters*, vol. 5, no. 2, pp. 3406–3413, Apr. 2020, ISSN: 2377-3766. DOI: 10.1109/LRA.2020.2976309. [Online]. Available: https://ieeexplore.ieee.org/document/9013028.

[11] N. D. Naclerio, A. Karsai, M. Murray-Cooper, *et al.*, "Controlling subterranean forces enables a fast, steerable, burrowing soft robot," *Science Robotics*, vol. 6, no. 55, eabe2922, Jun. 2021. DOI: 10.1126/scirobotics.abe2922. [Online]. Available: https://www.science.org/doi/10.1126/scirobotics.abe2922.

[12] P. A. der Maur, B. Djambazi, Y. Haberthür, *et al.*, "RoBoa: Construction and Evaluation of a Steerable Vine Robot for Search and Rescue Applications," in *2021 IEEE 4th International Conference on Soft Robotics (RoboSoft)*, Apr. 2021, pp. 15–20. DOI: 10.1109/RoboSoft51838.2021.9479192. [Online]. Available: https://ieeexplore.ieee.org/document/9479192.

[13] D. A. Haggerty, N. D. Naclerio, and E. W. Hawkes, "Hybrid Vine Robot With Internal Steering-Reeling Mechanism Enhances System-Level Capabilities," *IEEE Robotics and Automation Letters*, vol. 6, no. 3, pp. 5437–5444, Jul. 2021, ISSN: 2377-3766. DOI: 10.1109/LRA.2021.3072858. [Online]. Available: https://ieeexplore.ieee.org/document/9403886.

[14] D.-G. Lee, N. G. Kim, and J.-H. Ryu, "High-Curvature Consecutive Tip Steering of a Soft Growing Robot for Improved Target Reachability," in *2023 IEEE/RSJ International Conference on Intelligent Robots and Systems (IROS)*, Oct. 2023, pp. 6477–6483. DOI: 10.1109/IROS55552.2023.10341407. [Online]. Available: https://ieeexplore.ieee.org/document/10341407.

[15] S.-G. Jeong, M. M. Coad, L. H. Blumenschein, *et al.*, "A Tip Mount for Transporting Sensors and Tools using Soft Growing Robots," in *2020 IEEE/RSJ International Conference on Intelligent Robots and Systems (IROS)*, Oct. 2020, pp. 8781–8788. DOI: 10.1109/IROS45743.2020.9340950. [Online]. Available: https://ieeexplore.ieee.org/document/9340950.

[16] W. E. Heap, N. D. Naclerio, M. M. Coad, S.-G. Jeong, and E. W. Hawkes, "Soft Retraction Device and Internal Camera Mount for Everting Vine Robots," in *2021 IEEE/RSJ International Conference on Intelligent Robots and Systems (IROS)*, Sep. 2021, pp. 4982–4988. DOI: 10.1109/IROS51168.2021.9636697. [Online]. Available: https://ieeexplore.ieee.org/document/9636697.

[17] J.-h. Kim, J. Jang, S.-m. Lee, S.-G. Jeong, Y.-J. Kim, and J.-H. Ryu, "Origami-inspired New Material Feeding Mechanism for Soft Growing Robots to Keep the Camera Stay at the Tip by Securing its Path," *IEEE Robotics and Automation Letters*, vol. 6, no. 3, pp. 4592–4599, Jul. 2021, ISSN: 2377-3766. DOI: 10.1109/LRA.2021.3068936. [Online]. Available: https://ieeexplore.ieee.org/document/9387161.

[18] J. C. Norton, P. R. Slawinski, H. S. Lay, *et al.*, "Intelligent magnetic manipulation for gastrointestinal ultrasound," *Science Robotics*, vol. 4, no. 31, eaav7725, Jun. 2019. DOI: 10/gjpgdc. [Online]. Available: https://www.science.org/doi/10.1126/scirobotics.aav7725.

[19] Y. Kim, G. A. Parada, S. Liu, and X. Zhao, "Ferromagnetic soft continuum robots," *Science Robotics*, vol. 4, no. 33, eaax7329, Aug. 2019. DOI: 10.1126/scirobotics.aax7329. [Online]. Available: https://www.science.org/doi/10.1126/scirobotics.aax7329.

[20] G. Pittiglio, J. H. Chandler, T. da Veiga, *et al.*, "Personalized magnetic tentacles for targeted photothermal cancer therapy in peripheral lungs," en, *Communications Engineering*, vol. 2, no. 1, pp. 1–13, Jul. 2023, ISSN: 2731-3395. DOI: 10.1038/s44172-023-00098-9. [Online]. Available: https://www.nature.com/articles/s44172-023-00098-9.

[21] J. W. Martin, B. Scaglioni, J. C. Norton, *et al.*, "Enabling the future of colonoscopy with intelligent and autonomous magnetic manipulation," en, *Nature Machine Intelligence*, vol. 2, no. 10, pp. 595–606, Oct. 2020, ISSN: 2522-5839. DOI: 10/gm79tx. [Online]. Available: https://www.nature.com/articles/s42256-020-00231-9.

[22] S. Gervasoni, J. Lussi, S. Viviani, *et al.*, "Magnetically Assisted Robotic Fetal Surgery for the Treatment of Spina Bifida," *IEEE Transactions on Medical Robotics and Bionics*, vol. 4, no. 1, pp. 85–93, Feb. 2022, ISSN: 2576-3202. DOI: 10.1109/TMRB.2022.3146351. [Online]. Available: https://ieeexplore.ieee.org/document/9702265.

[23] G. Pittiglio, M. Brockdorff, V. T. da, J. Davy, J. Chandler, and P. Valdastri, "Collaborative magnetic manipulation via two robotically actuated permanent magnets," en, *IEEE Transactions on Robotics. Published online*, 2022.

[24] A. Z. Taddese, P. R. Slawinski, M. Pirotta, E. De Momi, K. L. Obstein, and P. Valdastri, "Enhanced real-time pose estimation for closed-loop robotic manipulation of magnetically actuated capsule endoscopes," en, *The International Journal of Robotics Research*, vol. 37, no. 8, pp. 890–911, Jul. 2018, ISSN: 0278-3649. DOI: 10/gd5k9x. [Online]. Available: https://doi.org/10.1177/0278364918779132.

[25] L. H. Blumenschein, A. M. Okamura, and E. W. Hawkes, "Modeling of Bioinspired Apical Extension in a Soft Robot," en, in *Biomimetic and Biohybrid Systems*, M. Mangan, M. Cutkosky, A. Mura, P. F. Verschure, T. Prescott, and N. Lepora, Eds., Cham: Springer International Publishing, 2017, pp. 522–531, ISBN: 978-3-319-63537-8. DOI: 10.1007/978-3-319-63537-8_45.

[26] N. G. Kim, D. Seo, S. Park, and J.-H. Ryu, "Self-Retractable Soft Growing Robots for Reliable and Fast Retraction While Preserving Their Inherent Advantages," *IEEE Robotics and Automation Letters*, vol. 9, no. 2, pp. 1082–1089, Feb. 2024, ISSN: 2377-3766. DOI: 10.1109/LRA.2023.3341697. [Online]. Available: https://ieeexplore.ieee.org/document/10354368.

[27] M. M. Coad, R. P. Thomasson, L. H. Blumenschein, N. S. Usevitch, E. W. Hawkes, and A. M. Okamura, "Retraction of Soft Growing Robots Without Buckling,"

IEEE Robotics and Automation Letters, vol. 5, no. 2, pp. 2115–2122, Apr. 2020, ISSN: 2377-3766. DOI: 10.1109/LRA.2020.2970629. [Online]. Available: https://ieeexplore.ieee.org/document/8977330.

[28] G. Pittiglio, L. Barducci, J. W. Martin, *et al.*, "Magnetic Levitation for Soft-Tethered Capsule Colonoscopy Actuated With a Single Permanent Magnet: A Dynamic Control Approach," *IEEE Robotics and Automation Letters*, vol. 4, no. 2, pp. 1224–1231, Apr. 2019, ISSN: 2377-3766. DOI: 10.1109/LRA.2019.2894907.

4.6 Evaluation and Summary of Findings

This chapter demonstrates the first integration of external magnetic tip steering with vine-robot technology for endoluminal applications. By eliminating the friction and tether drag that have traditionally limited the depth and maneuverability of magnetic flexible endoscopes, the proposed MVR system enables true shear-free navigation within the tortuous lumen, paving the way for the OME to reach deeper regions of the GI tract for advanced scanning and diagnosis.

High-curvature steering was validated, confirming that the MFE system retained effective maneuverability even when combined with the vine robot. Experiments with S-shaped paths revealed a substantial improvement in navigational capability compared to the prior MFE tether, with the MVR efficiently executing complex bends that would otherwise result in high friction and a loss of control. Importantly, the magnetic torque decays less rapidly with distance than the magnetic force, allowing precise tip orientation and steering to be maintained over a much greater EPM-IPM separation range. Meanwhile, the compliant, everting body of the vine robot provides the necessary axial force for propulsion. This primarily torque-based approach enables the use of a smaller IPM at the tip, which is critical for miniaturization and accessing narrower lumens, such as the small intestine, without compromising performance or safety. Additionally, it increases the feasibility of treating patients with a higher Body Mass Index, a scenario that poses a potential challenge for magnetic endoscopy due to the increased separation between the

need for the external magnet to be further away from the patient's GI.

This study establishes the basis for the future integration of OME technology at the tip of a vine robot. By combining the shear-free travel of the MVR with the autonomous, high-resolution imaging and sweeping capabilities of the OME, this approach has the potential to transform endoluminal diagnostics, enabling clinician-controlled or autonomous scanning in previously inaccessible areas. Moving forward, future studies should focus on achieving this integration alongside the development of advanced retraction methods to further expand the clinical impact of these technologies.

Chapter 5

Conclusions

5.1 Summary of contributions

In this thesis, we have outlined the urgent need for endoscopic technologies capable of enabling the early detection and screening of GI cancers worldwide. Beginning with the current gold standard, the standard flexible endoscope, we identified six critical areas for improvement: limited access, excessive push force causing patient pain and discomfort, operator ergonomics (physical burden), ease of use (mental burden), lack of in situ histopathology, and frictional drag associated with tethered navigation.

The introduction discusses how robotic endoscopes, particularly magnetic flexible endoscopes, have opened new frontiers by transitioning from conventional "push" locomotion to magnetic "pull" locomotion. This innovation significantly reduces the forces transmitted to the patient, thereby minimizing discomfort and the risk of injury. Furthermore, these systems enhance the ease of use and ergonomics of endoscopic procedures by incorporating multiple levels of autonomy into their magnetic platforms. By lessening the cognitive and physical demands on the operator and implementing intelligent steering and automation strategies, magnetic endoscopic systems empower both novice and expert users. This paves the way for broader global adoption and the development of parallelized and remotely supervised workflows. Additionally, the potential for teleoper-

ation offered by robotic systems can address disparities in access by reducing the reliance on highly skilled professionals.

Through a series of technological advancements at the intersection of magnetic actuation and soft robotics, this thesis builds upon the progress made in magnetic endoscopy to address the remaining challenges.

First, Chapter 2 presents a novel strategy to enhance the dexterity of magnetic endoscopes without compromising the simplicity and pain-free navigation enabled by magnetic manipulation. Specifically, this chapter addresses a fundamental limitation shared by both standard flexible endoscopes and magnetic systems: the inability to perform precise rolling motions.

Second, Chapter 3 introduces a new method for in situ histopathology, detailing the design and validation of a magnetic endoscopic system capable of performing autonomous virtual biopsies via high-resolution, closed-loop microUS imaging. This technology allows real-time lesion detection and characterization during the procedure, supporting immediate therapeutic intervention. Integrating this capability streamlines the patient care pathway, shortens waiting times, reduces costs, and addresses a significant bottleneck in the early diagnosis of GI disease.

Third, Chapter 4 addresses the enduring problem of frictional drag and tether accumulation, which is a major obstacle limiting the reach and maneuverability of previous magnetic and tethered endoscope designs. By integrating vine-inspired robotics with external magnetic steering, this thesis presents a solution for truly shear-free navigation, enabling endoscopes to penetrate deeper into the GI tract than previously possible. This development expands the potential for minimally invasive procedures in anatomical regions that have, until now, remained out of reach.

Finally, this research builds upon established progress in painless, autonomous endoscopy by adding new algorithms to the system's autonomous capabilities, while preserving the gentle and pain-free methods of navigation. By incorporating virtual biopsies into the workflow, the potential for telesurgery is further enhanced, making advanced care accessi-

ble in settings lacking infrastructure for rapid or cost-effective tissue analyses. Automating the processes of lesion detection and characterization streamlines clinical pathways and increases access to early diagnosis.

In summary, this work collectively propels endoscopy toward a future where procedures are safer, more comfortable, highly automated, and diagnostically robust, with enhanced capacity for deep navigation and same-session diagnosis and treatment. The integration of magnetic actuation, autonomy, virtual biopsy, and vine-inspired navigation establishes a comprehensive platform for ongoing innovation and clinical translation.

5.2 Future directions

Future directions will emphasize further miniaturization and comprehensive preclinical and clinical studies.

Building upon the successful validation of the OME's virtual biopsy capability using an in vivo artificial polyp model, future efforts will extend this approach to real polyps and a diverse range of pathological tissue types. This expansion will enable a robust evaluation of the potential of the OME for lesion characterization and margin determination. By advancing to studies that include human pathology, the goal is to demonstrate that this technology can produce clinically actionable imaging, paving the way for virtual biopsies to replace traditional tissue sampling in screening programs.

Subsequent research using on the vine robot will transition the findings from bench-top experiments to in vivo animal models. This next step will further demonstrate the MVR's ability to access and operate within deeper, more complex anatomical regions compared to traditional magnetic endoscopes and standard flexible endoscopes. In parallel, work will continue to optimize retraction mechanisms, build on promising preliminary results, and refine the approach for smooth, safe, and reliable clinical use.

Furthermore, there is significant potential to enhance patient monitoring by integrating this magnetic flexible endoscope platform with advanced colon-reconstruction techniques.

By mapping polyp locations onto three-dimensional reconstructions of the colon, clinicians will be able to longitudinally track lesions between screening procedures. This will enable careful surveillance and more targeted, less invasive interventions for benign or low-risk lesions, ultimately improving patient outcomes and resource efficiency.

Collectively, these efforts will accelerate the translation of these innovations into clinical practice, paving the way for safer, more accessible, and more effective endoluminal procedures.

Appendix A

Appendix to Autonomous 3D Micro-ultrasound Virtual Biopsies

A.1 Supplementary Discussion

A.1.1 Addressing the DoF Limitation in Magnetic Manipulation

In an attempt to minimize the potential energy between an external magnetic field $\mathbf{B_E} \in \mathbb{R}^3(T)$ generated by the controlling source (external dipole) and a magnetic object (internal dipole) with magnetic moment, $\mathbf{m}_I \in \mathbb{R}^3\,(A \bullet m^2)$, an alignment torque τ_m is induced on the magnetic object and is given by:

$$\tau_m = \mathbf{m}_I \times \mathbf{B_E} = S(\mathbf{m}_I)\mathbf{B_E} \tag{A.1}$$

where $S(\cdot) : \mathbb{R}^3 \mapsto \mathbb{R}^{3\times3}$ is the skew-symmetric matrix operator. The gradient-induced force exerted on the magnetic object is denoted by $\mathbf{F}_m$:

$$\mathbf{F}_m = \nabla(\mathbf{B_E} \bullet \mathbf{m}_I) \tag{A.2}$$

In the magnetic object's local coordinate frame with orthonormal vectors $\mathbf{X_I}, \mathbf{Y}_I$, and $\mathbf{Z}_I \in \mathbb{R}^3$, Euler angles, ϕ, θ and ψ denote the rotation around these vectors (Figure 3.3). Conventionally, $\mathbf{X_I} \parallel \mathbf{m}_I$ (as shown in Figure 3.1 and 3.3), but when $\mathbf{m}_I \parallel \mathbf{B_E}$ then according to Equation A.1.1, $\tau_m = \mathbf{0}$. Consequently, it is not possible to generate magnetic alignment torque around the magnetization axis to control the roll angle (ϕ).

As discussed in the manuscript, other methods have primarily been demonstrated in fluid environments where force and torque requirements are low. These systems typically rely on electromagnetic coil systems, requiring eight magnetically controllable inputs, leading to high power consumption and limited workspaces compared to single EPM systems.

Table A.1 highlights how the introduction of roll in the single EPM system represents a significant improvement over previous approaches. In electromagnetic coil systems, the workspace and applied field are proportional to power consumption.

A.1.2 Roll Generation in the Oloid

By concatenating orthonormal basis vectors of $\mathbb{R}^3$ we can formulate a rotation matrix, $\mathbf{R}_O^F$ which can be expressed as:

$$\mathbf{R}_O^F = \begin{bmatrix} \widehat{\mathbf{x}}_O & \widehat{\mathbf{y}}_O & \widehat{\mathbf{z}}_O \end{bmatrix}. \tag{A.3}$$

If:

The oloid is magnetized about the $\mathbf{x}$-axis $\widehat{\mathbf{x}}_O \parallel \mathbf{m}$, and

It rotates about the line $\mathbf{p}_2 - \mathbf{p}_1$, then

Its orientation can be controlled so long as $\widehat{\mathbf{x}}_O \nparallel \mathbf{p}_2 - \mathbf{p}_1$.

In other words, rotation can be induced so long as $\widehat{\mathbf{x}}_O$ is not perpendicular to the surface normal $\widehat{\mathbf{z}}_F$:

$$\widehat{\mathbf{x}}_O \perp \widehat{\mathbf{z}}_F \implies \widehat{\mathbf{x}}_O^T \widehat{\mathbf{z}}_F \neq \mathbf{0} \tag{A.4}$$

Where $\widehat{\mathbf{z}}_F$ is equivalent to the z-axis of {F}.

From inspection of $\mathbf{R}_O^F$ it must hold that:

$$-\frac{sin(u)}{\sqrt{2(1+cos(u))}} \neq 0 \forall u \in \left(-\frac{2\pi}{3}, 0\right) \cup \left(0, \frac{2\pi}{3}\right) \tag{A.5}$$

This is true only if:

$u = 0$, or $u = \pi$

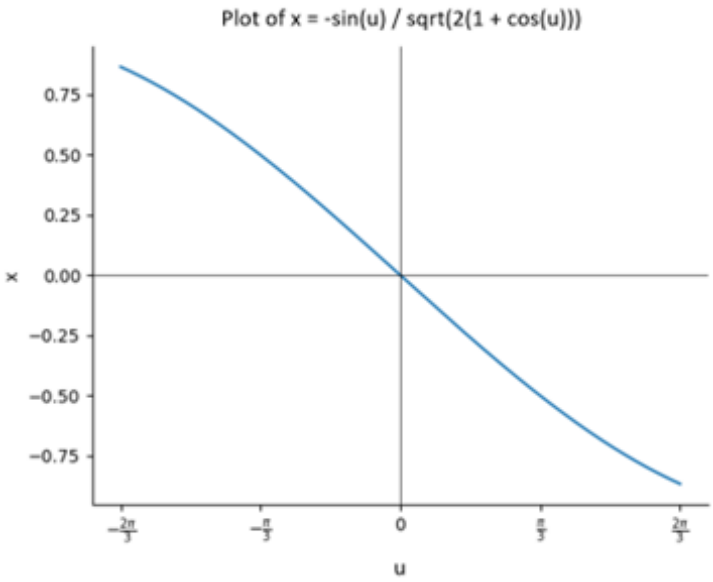

Figure A.1: Function plot over the range u.

In a cylinder, this is true throughout the entire surface.

Table A.1: **Roll Approaches Comparison.** All values were estimated based on the details provided in the respective papers. N/A – information not provided. *This workspace is based on the static range of the EPM which can be moved within a larger workspace (1000 × 800 × 800 mm^3) due to the mobility provided by the robot arm.

Paper	**Magnetic Workspace**	**Environment**	**Required Magnetically Controllable Inputs**	**Applied Field**	**Maximum Power**	**Roll**
Wang et al. (13)	100 × 100 × 100 mm^3	Water	8	N/A	1.4 kW	Yes
Xu et al. (10)	N/A	Non-Newtonian fluid (paraffin oil, glycerol)	8	20 mT	6 kW	Yes
Diller et al. (8)	20 × 20 × 20 mm^3	Silicone oil	8	8.3 mT	N/A	Yes
Giltinan et al. (11)	1000 mm^3	Silicone oil	8	22 mT	6 kW	Yes
Taddese et al. (44)	300 × 300 × 150 mm^3 *	In vivo – colon	5	25 mT	1–1.5 kW	No
This work	300 × 300 × 150 mm^3 *	In vivo – colon	5	25 mT	1–1.5 kW	Yes

A.2 Supplementary Figures

A.2.1 3 DoF Orientation Comparison between OME and MFE

The magnitudes of the points in the radar plot shown in Figure 3.4 of the manuscript were determined by calculating the average change in each DoF across the three repetitions presented for each movement in Figure A.2. As evidenced by the raw data in Figure A.2, the starting point for roll is consistently near zero in all the OME's movements. In contrast, the MFE exhibits arbitrary baseline values for roll initiation. Additionally, there is increased variability during movements not intended to induce roll, such as tilt and translation. Lastly, when subjected to the same input intended to trigger roll in the OME, the MFE's roll response was ineffective, especially for positive roll.

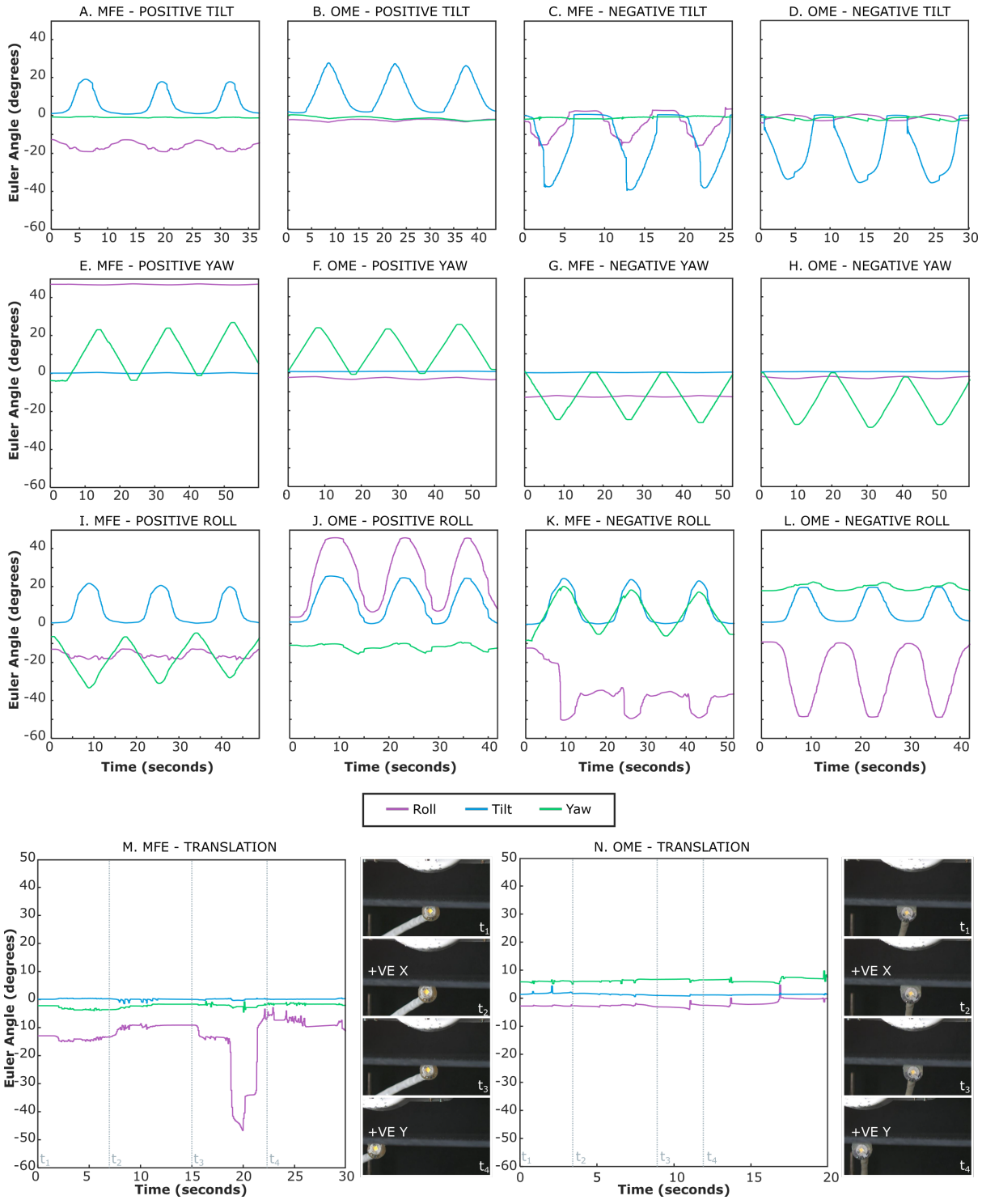

Figure A.2: 3-DoF Orientation Comparison between OME and MFE. The figure illustrates the coupling between roll, tilt and yaw, positive and negative, for both the MFE and OME. It also depicts the variation in orientation during x and y translation for both devices. See Data S2 for the corresponding multimedia.

A.2.2 Generating Rolling Motion with the Oloid in Open-Loop

A.2.2.1 Using MFE System

Figure A.3 is an extended representation of Figure 3.5 in the manuscript.

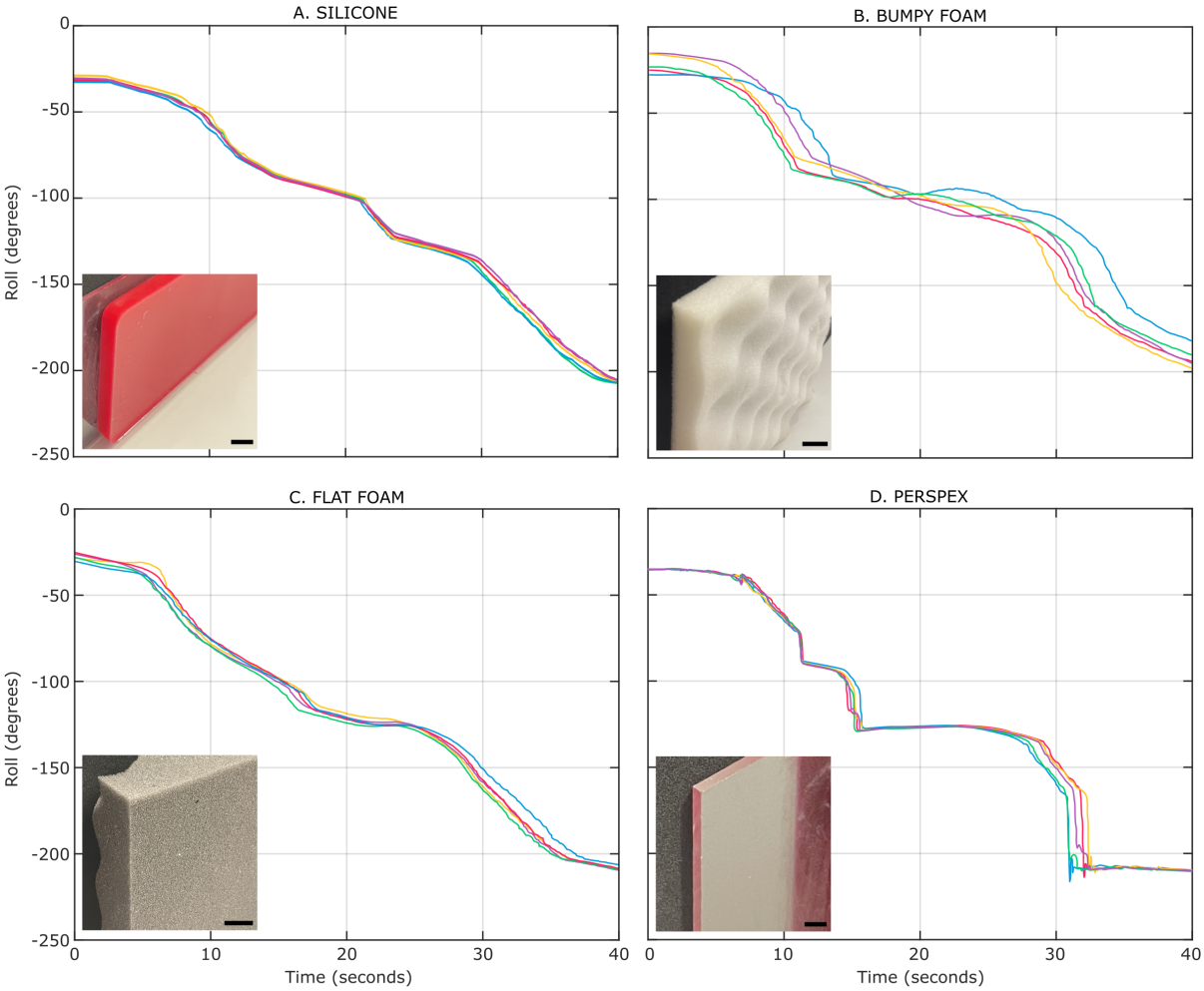

Figure A.3: **Oloid Rolling on Various Surfaces.** Rolling performance of the oloid on (A) silicone, (B) bumpy foam, (C) flat foam, and (D) Perspex. Five repetitions shown for each. See Data S5 for the corresponding multimedia. Scale bars, 10 mm.

A.2.2.2 Using Electromagnetic Coil System

The oloid control model is generic and not exclusively designed for use with a robotic arm and an external permanent magnet. To support this claim, we demonstrate that, by applying a similar model to the one described in the paper, the oloid shape can perform a rolling motion on a flat surface, using electromagnetic coils. For this demonstration, a MiniMag system (MagnebotiX, Switzerland) shown in Figure A.4 (A) was employed.

In order to fit this setup and to demonstrate scalability, the OMD was scaled down to a defining oloid radius of 5 mm called the Mini-OMD. Snapshots of the rolling motion are illustrated in Figure A.4 (B). This result demonstrates scalability, a tetherless configuration and that roll can be achieved with the oloid regardless of contact with the upper or lower surfaces.

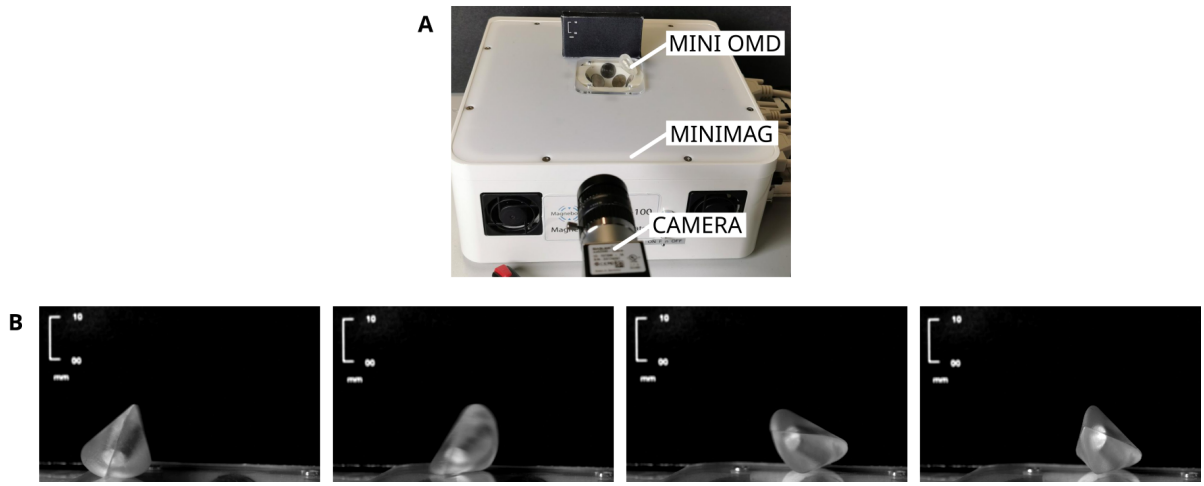

Figure A.4: **Oloid Rolling in MiniMag.** (A) Experimental Setup and (B) Snapshots of a 5 mm Mini OMD rolling on a flat surface. See Data S1 for the corresponding multimedia.

A.2.3 Closed-Loop Control of the Oloid-shaped Magnetic Device (OMD)

Figure A.5 is an extended representation of Figure 3.6 in the manuscript.

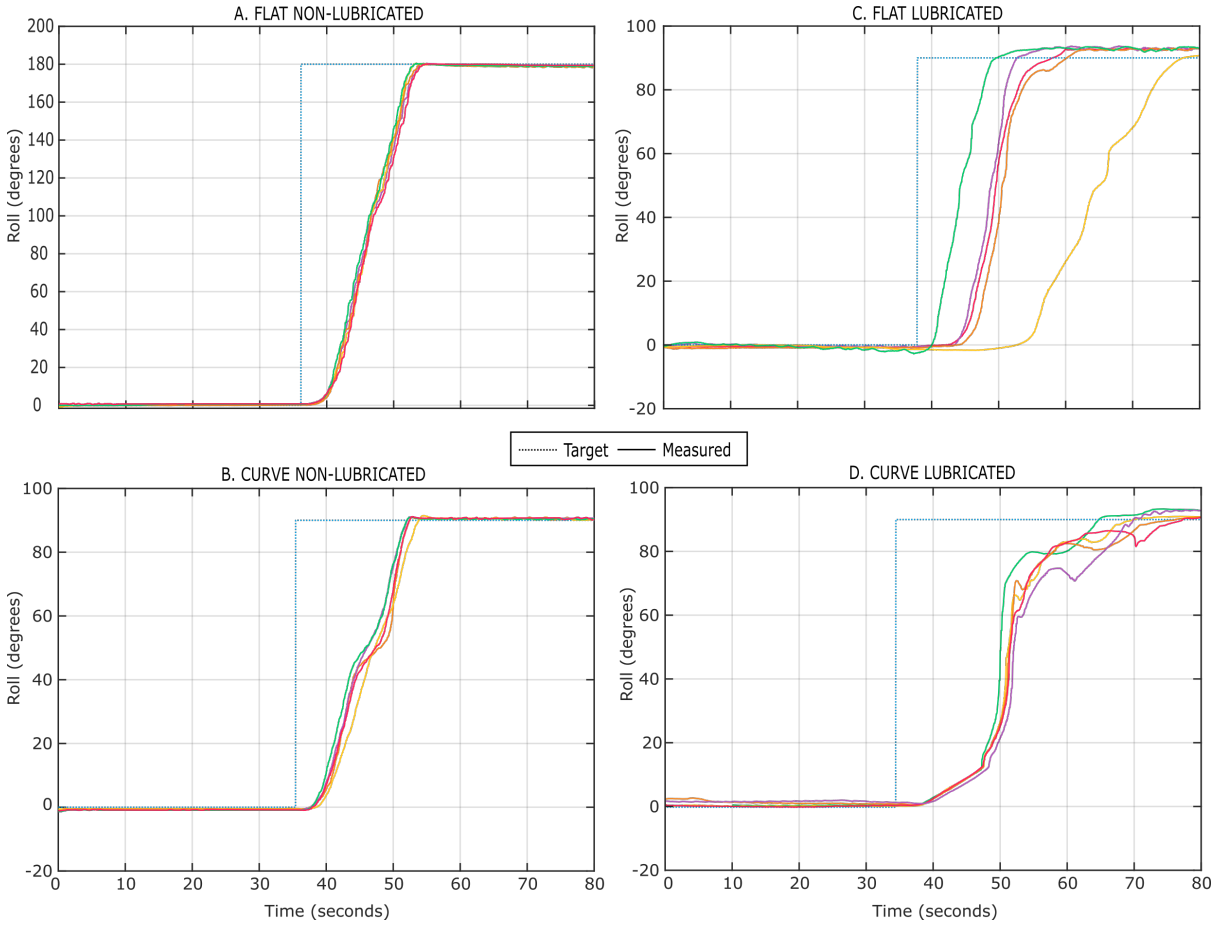

Figure A.5: **Closed-loop control of the OMD, step input on a:** (**A**) flat non-lubricated surface (**B**) curved non-lubricated surface (**C**) flat lubricated surface (**D**) curved lubricated surface. Five repetitions shown for each.

Small oscillations are observed especially on the lubricated surfaces from a combination of localization errors and inherent dynamics of the KUKA robot's control system. In scenarios involving faster environments, such as the lubricated surfaces, these oscillations become more pronounced. To reduce oscillations, KUKA's Fast Robot Interface (FRI) could be implemented in place of the current smart servo control. The FRI offers higher update rates and more precise control, which can significantly minimize oscillatory behavior by enabling faster and more accurate responses to control inputs.

A.3 Supplementary Methods

A.3.1 Benchtop Autonomous Ultrasound Sweeping Setup

The capsule was evaluated using the platform described in Figure A.6, which includes the OME-U, the KUKA LBR robotic arm, and the microUS system. A silicone phantom was used for benchtop trials and the initial characterization of the robotic system.

Two display monitors were employed: one for the robot control user interface and the other for ultrasound visualization.

The capsule's dexterity was recorded using a Basler Ace camera (acA2040-120uc, Basler AG, Ahrensburg, Germany), as depicted in the red square in Figure A.6.

The 8 mm thick silicone phantom (Ecoflex 00-30, Smooth-on, PA, USA), utilized to validate different algorithms, was enclosed within a 7 cm inner diameter acrylic tube. Copper strips were integrated into the phantom to create components with high echogenicity, facilitating clear identification with the ultrasound probe. The white area in the second image (enclosed by the purple frame) becomes apparent when the array is oriented towards the copper strip, confirming both the proper functioning of the OME-U and the probe's ability to capture images simultaneously. The green and red bars at the top of the snapshot, enclosed by the purple frames, highlight the quality of contact between the OME and the silicone phantom.

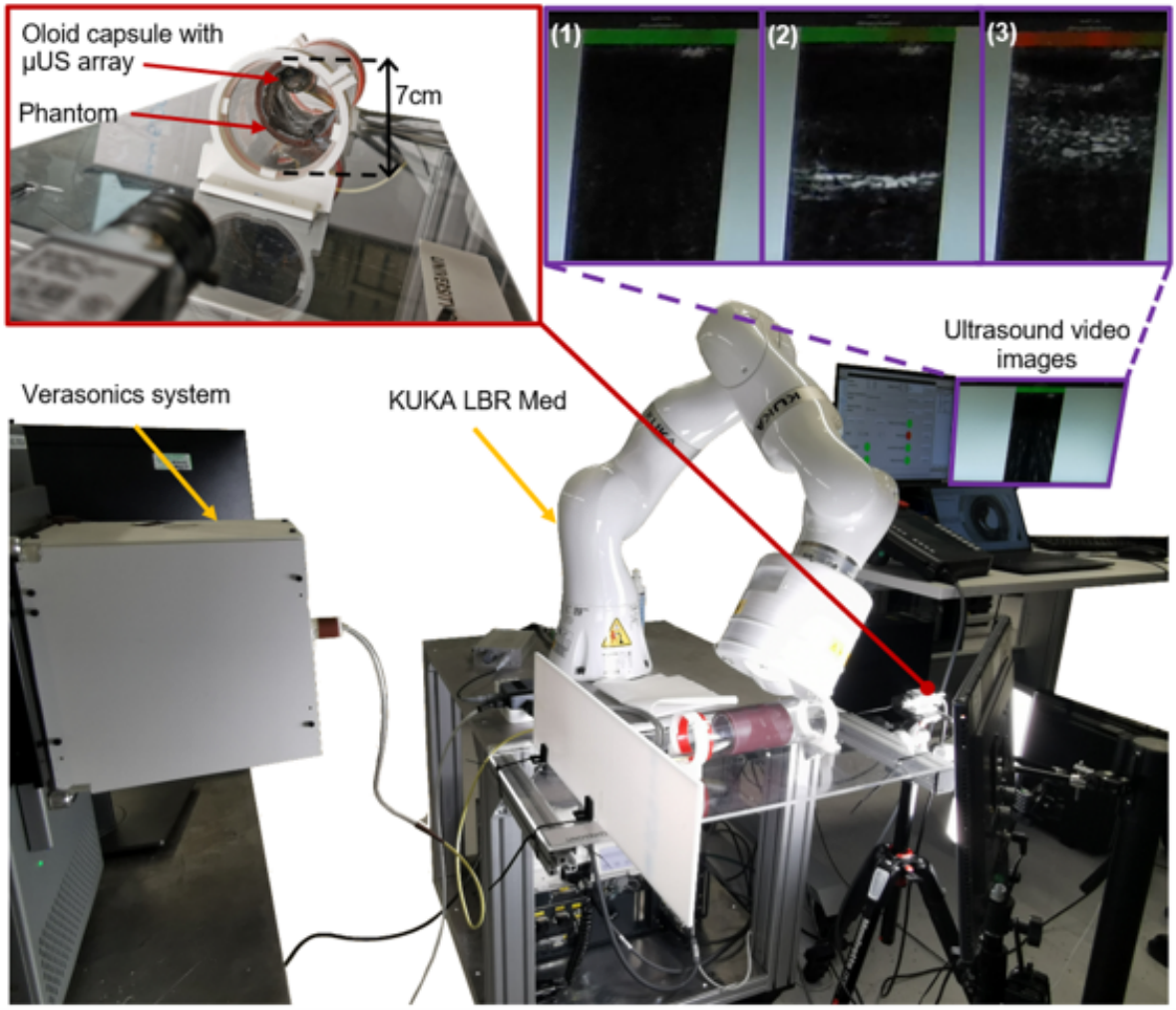

Figure A.6: **Detailed illustration of the experimental setup.** Overview of the various components utilized during the benchtop experimentation with (red square) validation point of view for contact detection and roll/sweep performance and (purple square) snapshot depicting feedback on contact quality (1-2: good, 3: none) and visualization of the copper strip (2).

A.3.2 Contact Detection Algorithm

Contact detection was performed using real-time images provided by the ultrasound probe. A series of tests was conducted on phantoms to demonstrate the effective integration of the microUS array and Verasonics acquisition of ultrasound images. The setup and phantom were used as previously described.

Figure A.7 illustrates five different snapshots of the post-processed outputs using the proposed algorithm. The ultrasound images were cropped to a sector outlined in the frame where differences were most significant, approximately 7% - 30% of the image

width. The maximum value for each column was then condensed to obtain the mean, resulting in values between 0 (decoupled) and 1 (coupled). The algorithm's detected coupling quality is visualized by the colored bar at the top, transitioning from green (good coupling) to red (poor coupling).

This coupling value was integrated into a control loop to enable sweeping while correcting for any loss of contact to maintain continuous imaging. This control strategy was experimentally validated by arbitrarily positioning the capsule within the tube without contact with the phantom. Using the localization system, movements of the robotic arm enabled repositioning of the capsule in contact with the tissue and initiation of the sweeping motion. Observation of the two copper strips (Figure A.7.3 and A.7.5) present in the silicone as the probe swept in continuous motion further validated the operation of the closed-loop control strategy for automatic imaging tasks.

During the animal trials, contact threshold parameters were calibrated by performing 10 manual repetitions:

- 5 contact recoveries with a tilt manoeuvre
- 5 contact recoveries from an upside-down configuration

These parameters were saved in the ROSbag* and implemented in the control loop. A series of 5 repetitions of autonomous sweeping were then performed, starting from no contact with the mucosa, to validate proper functioning.

*A ROSbag is a file format in ROS used for storing ROS message data. It is essentially a log file that can record and subsequently replay ROS message streams. It enables postprocessing and analysis of the robotic systems and sensors data.

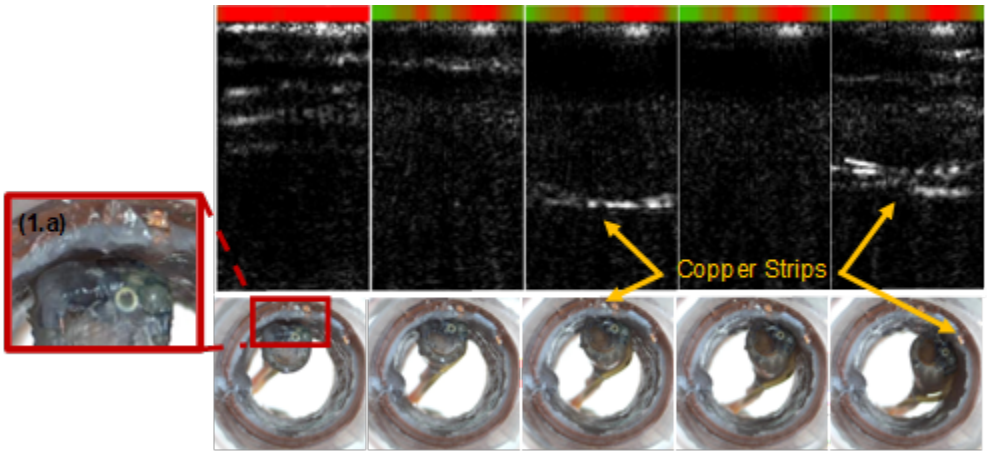

Figure A.7: **Illustration of the contact detection algorithm and benchtop autonomous sweeping.** The snapshots illustrate sweeping from a non-contact situation highlighted in the magnified image (1.a) and by the red bar at the top of the US image to successful autonomous sweeping while keeping contact and identification of the copper strip in the phantom. See Data S3 for the corresponding data.

A.3.3 In Vivo Experimental Setup

The animal experiments were conducted in accordance with the Animal (Scientific Procedures) Act 1986, as well as the guidelines provided by NC3Rs and ARRIVE.

During the animal experimentation, the setup employed was quite similar to that described for the benchtop experiments. All procedures were recorded from both the perspective of the OME-U and an external viewpoint, utilising a standard Olympus endoscope (shown in Figure A.8).

Dexterity validation experiments were initially conducted, followed by the recording of healthy tissue and probe validation and, subsequently, the creation of false polyps and scanning of them.

Real-time evaluation of all experiments was performed, and recordings were made using ROSbags (Data S4).

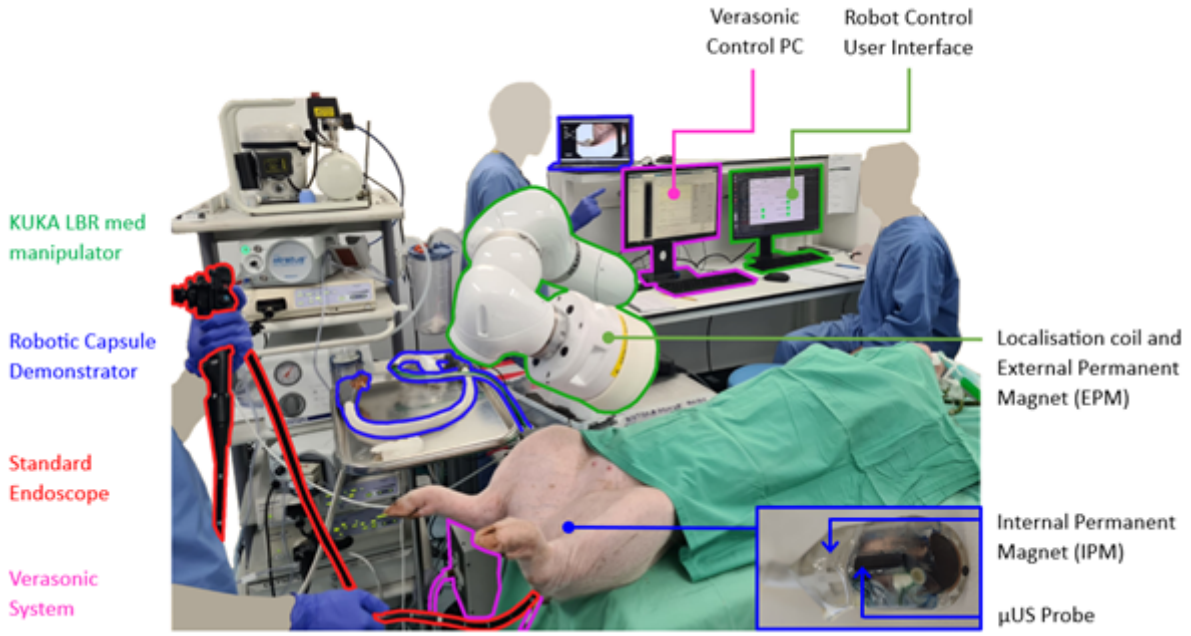

Figure A.8: **Detailed illustration of the in vivo setup highlighting the different devices used during the animal trial and color identification of the related parts.**

A.3.4 Three-dimensional Subsurface Reconstruction Algorithm

This script outlines the steps involved in reconstructing a 3D volume from a series of 2D images, including reading images, adjusting positions, and visualizing the volume and its surface as shown in Figure A.9.

1. **Initialization:**
   - An empty matrix named 'volume' is created to store the reconstructed volume.
   - Another matrix 'robotPositions' is initialized to store the positions of the robot corresponding to each image.
2. **Loading ROSbag File:**
   - The ROSbag file named 'XXX_XXX.bag' is loaded into the workspace.
3. **Reading US Images:**
   - All image topics present in the ROSbag file are obtained using the 'select' function, filtering by message type 'sensor_msgs/Image'.

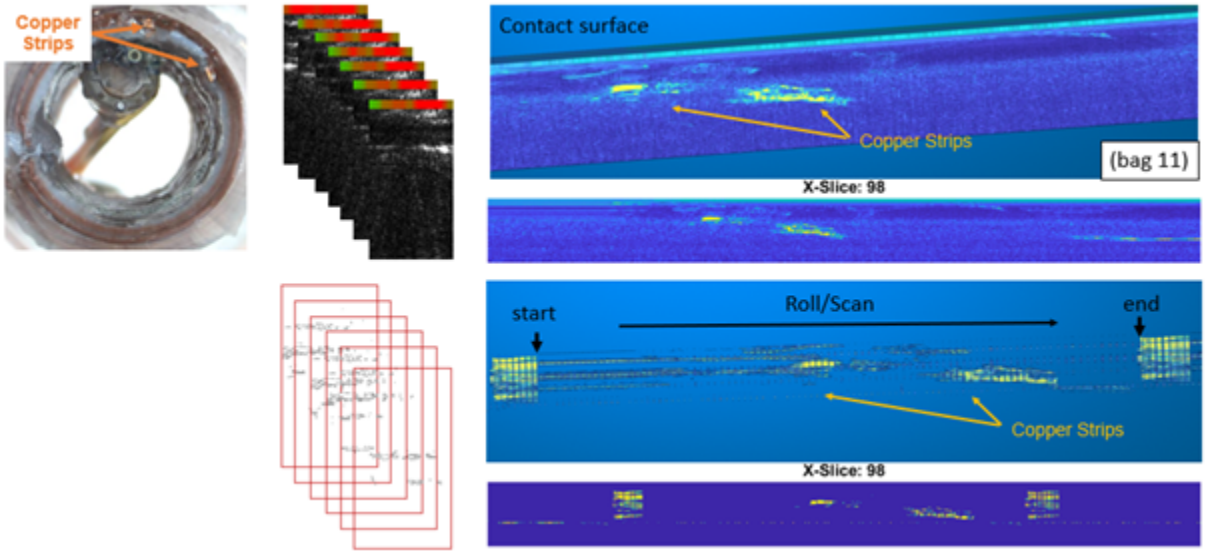

Figure A.9: **Detailed image reconstruction using the algorithm.** Snapshot of the experimental setup on the left. Stack of images before and after extraction of the desired information in the center. Volume visualization after voxel creation before and after extraction of the desired information on the right.

- The images are stored in a dedicated folder.

4. Reading Robot Positions:

- There is a call of the topic 'mfe/pose' to retrieve the robot positions from the ROS bag file.
- The positions are stored in the 'robotPositions' matrix.

5. Image Processing Loop:

- The script iterates through each image.
- The file path for the image is constructed.
- The image is read.
- If the image is not grayscale, it is converted to grayscale. Additionally, the top 23 rows of the image are set to black (logical mask to false). [23 rows of contact detection]
- The position of the image is adjusted based on the robot's position.
- The adjusted image is stored in the 'volume' matrix.

6. Volume Visualization:

- The reconstructed volume is visualised.
- Various settings for visualization such as size, view angle, etc., are adjusted.

7. Surface Visualization:

- An isosurface is generated based on the volume data. The isovalue is set as a fraction of the maximum value in the volume.
- The surface is visualized using 'trimesh' function.

A.3.5 Benchtop 3D Reconstruction Validation

The reconstruction algorithm's spatial fidelity and accuracy were validated through two distinct approaches: utilising the robotic arm, mirroring conditions observed during animal trials, and within a controlled environment employing the setup depicted in Figure A.10. For the controlled experiment, the capsule was connected to a servomotor (MX-28, ROBOTIS DYNAMIXEL) to simulate seamless motion and continuous contact.

To ensure a comparable scenario, the silicon phantom with a copper strip was employed for both experiments.

Across both setups, the positional consistency along the x and y axes remained constant, while the precision of the US images remained unaffected by the robotic setup. Conversely, the accuracy along the z-axis was found to be directly influenced by the robotic platform and the coupling algorithm.

In quantifiable terms, the error of the strip width estimation using the Figure A.10 setup was measured at 2%, contrasting with an 8% error when integrated into the robotic platform.

This discrepancy must be contextualised with the robot's localization capabilities, which dictate the reconstructed voxel sizes. Indeed, the 8% error falls within the expected uncertainty range of the localization system.

It should be noted that this error remained within the same order of magnitude during the in-vivo tests assessing its reliability.

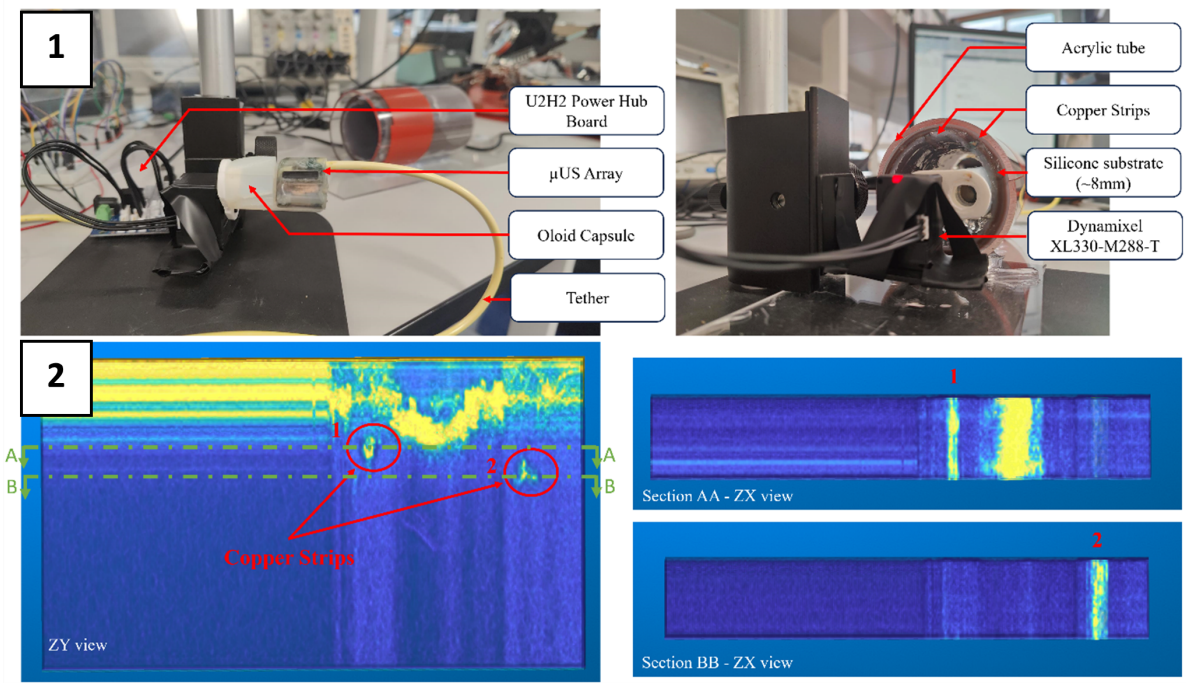

Figure A.10: **Calibration and evaluation setup for the reconstruction algorithm.** (1) Experimental setup using a servomotor and constant speed for accuracy evaluation and threshold calibration. (2) Different views of the reconstructed volume, highlighting the reconstruction accuracy of copper strips. See Data S3 for the corresponding data.

A.3.6 ROS Interface

Robot Operating System (ROS) was utilized to manage all aspects of our robotic endoscope's functionality. The KUKA LBR Med R820 robot is managed in joint space through the 'iiwa_stack' software package (version 1.3.0) (`https://github.com/IFL-CAMP/iiwa_stack/wiki`), which seamlessly integrates with ROS Melodic (Ubuntu 18.04).

MATLAB was utilized for ultrasound data processing, and the processed data were transmitted via the Olympus Decklink Mini Monitor 4K frame-grabber which interfaces with ROS for real-time processing.

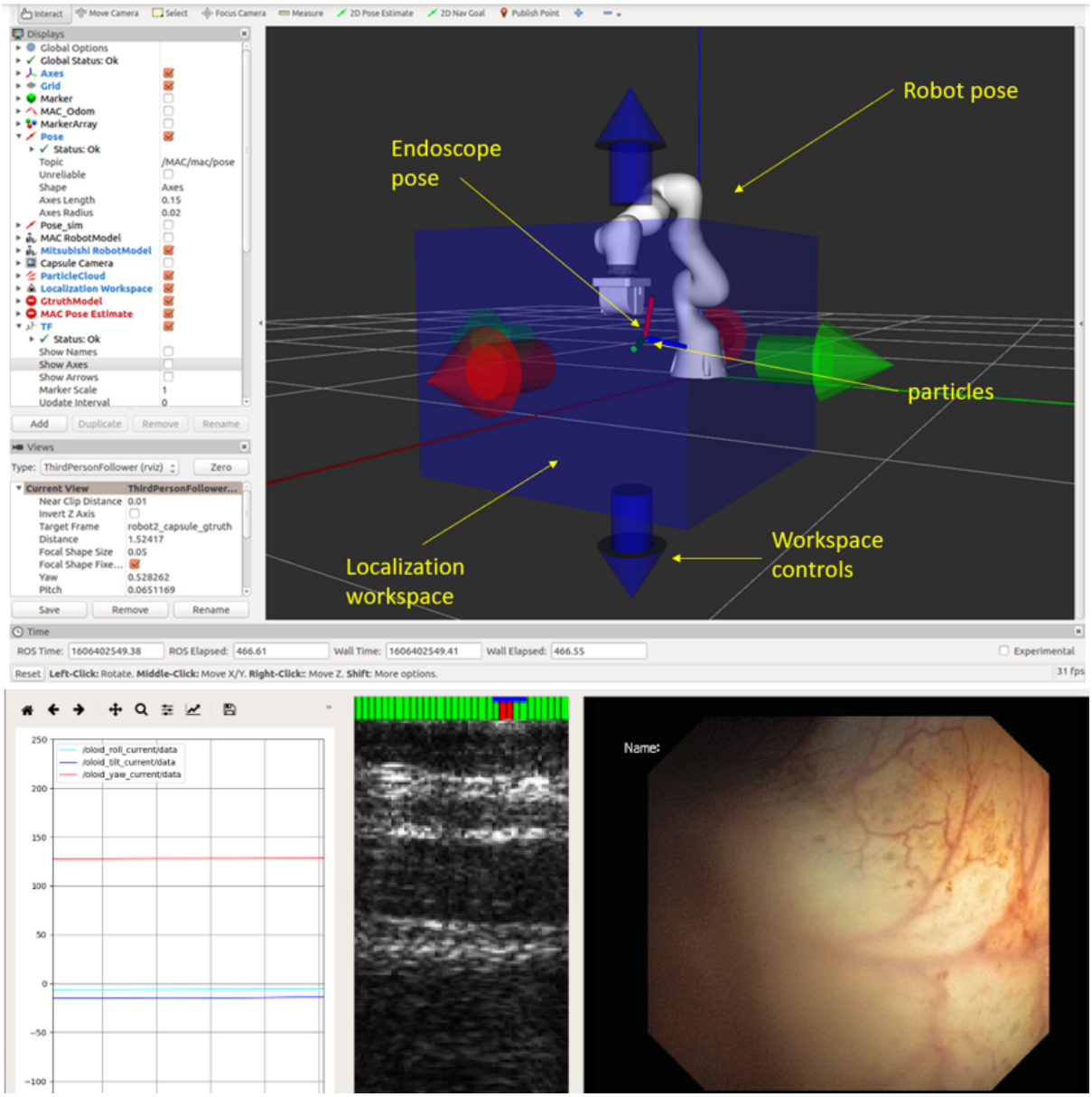

Figure A.11: ROS Interface

A.3.7 Localization Calibration

The localization system in the endoscope is calibrated using a calibration cube precisely tailored to the endoscope's overall shape. The cube, machined from a solid block of Delrin, ensures sub-degree accuracy by providing dedicated features that secure the endoscope in a reference orientation relative to gravity. This process computes the orientation of the IMU with respect to the endoscope reference frame and the relative orientation of each sensor with respect to the IMU.

The calibration only involves orientations, and so, the position of the endoscope during calibration is not critical. The main variable affecting accuracy is the orientation of the surface upon which the cube rests during data acquisition, which should be flat with respect to gravity. The calibration process is robust, with errors up to 5% of the sensors' range having negligible effects on localization.

To address potential drift over repeated uses, the system incorporates a secondary 'on-the-fly' gyro bias removal calibration. This feature ensures consistent calibration over more than 10 procedures (typically no more than 30 minutes), with any constant bias easily detected by placing the endoscope in a known pose and verifying static accuracy. These measures ensure the robustness and reliability of the localization system, even under conditions that may introduce minor disturbances.

A.3.8 Other Supplementary Material

Movies:

- **Movie S1:** Concept Overview of the Oloid-Shaped Magnetic Medical Device.
- **Movie S2:** Oloid Magnetic Endoscope (OME) versus Magnetic Flexible Endoscope (MFE) Degrees of Freedom (DoFs)
- **Movie S3:** Open-Loop Control of the Oloid-Shaped Magnetic Device (OMD).
- **Movie S4:** Closed-Loop Control of the Oloid-Shaped Magnetic Device (OMD).
- **Movie S5:** *In Vivo* Rolling and Sweeping Motion of the Oloid Magnetic Endoscope (OME).
- **Movie S6:** *In Vivo* Autonomous Sweeping of the Oloid Magnetic Endoscope with Integrated microUS (OME-U) and 3D Virtual Biopsy Reconstruction.

`https://www.youtube.com/playlist?list=PLWtIpCj5v7Nez_fUVWN239PC-4kG1nhsh`

Data:

- **Data S1: MiniMag-miniOMD.mp4:** Video showing mini-OMD oloid rolling in the MiniMag electromagnetic coil system.
- **Data S2: DoF_comparison.zip:** This folder contains video footage with live Euler angle graphs comparing the degrees of freedom (DoF) of the system under different conditions.
- **Data S3: 3D_Reconstruction.zip:** This folder contains data related to the 3D reconstruction experiments.
- **Data S4: In_vivo_-_roll_sweep.zip:** This folder contains in vivo roll sweep experiments, including .bag files, endoscopic videos and synced demonstration videos.
- **Data S5: Open_loop_roll.zip:** This folder contains videos from the open-loop roll experiments on different surfaces.

- **Data S6: Oloid_development.m:** MATLAB script to apply a transformation to a single point using Theorem 4 to handle the full transformation for the oloid geometry.
- **Data S7: Parametric_Oloid_Surface.m:** MATLAB Script to plot the oloid shape based on parametric equations.
- **Data S8: Theorem4_sym.m:** MATLAB Script with function for Theorem 4 from the paper by Dirnbock and Stachel (1997), "The Development of the Oloid" to generate the transformation matrices for the oloid's motion.

Dryad Database: `https://doi.org/10.5061/dryad.t1g1jwtbx`

Appendix B

Appendix to SoRo

B.1 Navigation with Suspended Tip

Table B.1: Coupling deviation between the EPM and IPM along the x-y plane.

Speed (mm/s)	**Run**	**X deviation (mm)**	**Y deviation (mm)**	**Yaw deviation (°)**
3	1	19.7	18.9	17.5
3	2	16.8	22.7	25.0
3	3	19.4	27.3	10.1
3	4	15.8	27.7	20.0
3	5	23.1	25.0	22.8
3	**Overall**	**19.0 ± 2.8**	**24.3 ± 3.6**	**19.1 ± 5.8**
4	1	16.7	17.1	39.4
4	2	19.1	19.7	23.9
4	3	20.6	22.7	18.3
4	4	21.6	25.7	17.1
4	5	19.9	19.9	13.0
4	**Overall**	**19.6 ± 1.8**	**21.0 ± 3.3**	**22.3 ± 10.3**

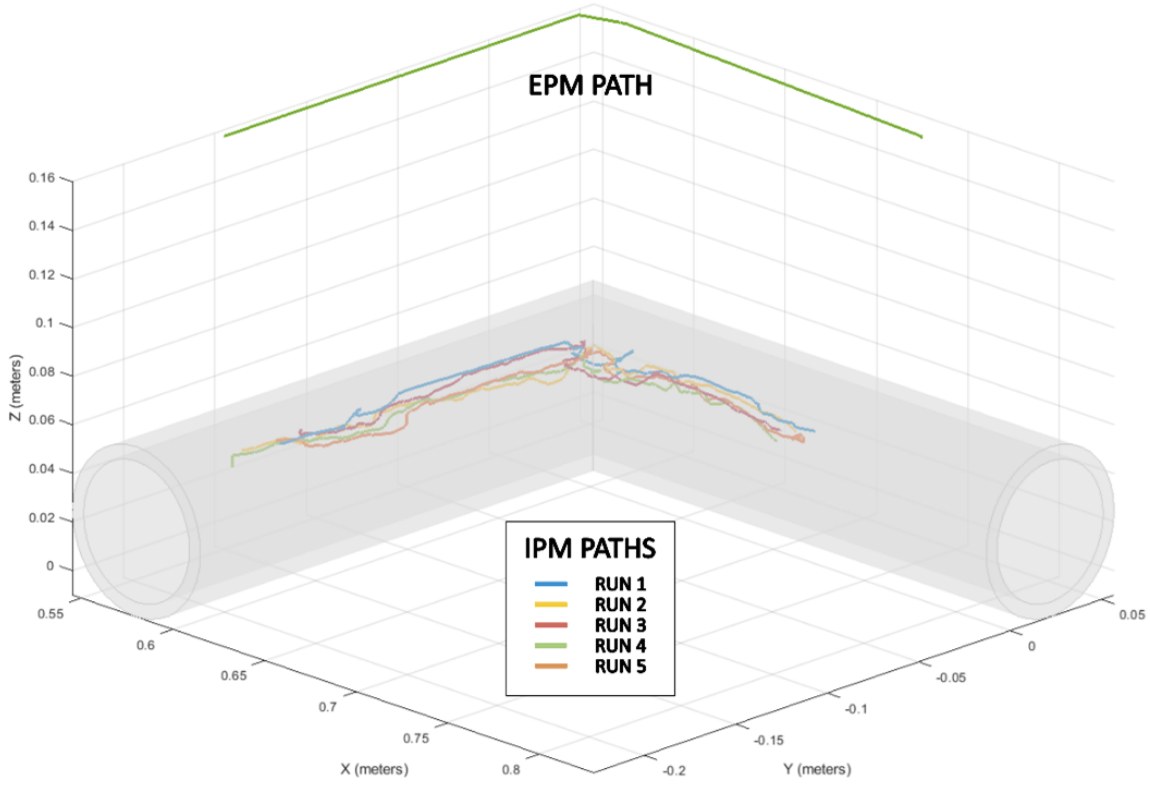

Figure B.1: 3D position data of the center of the EPM and IPM at 3mm/s for five repetitions.

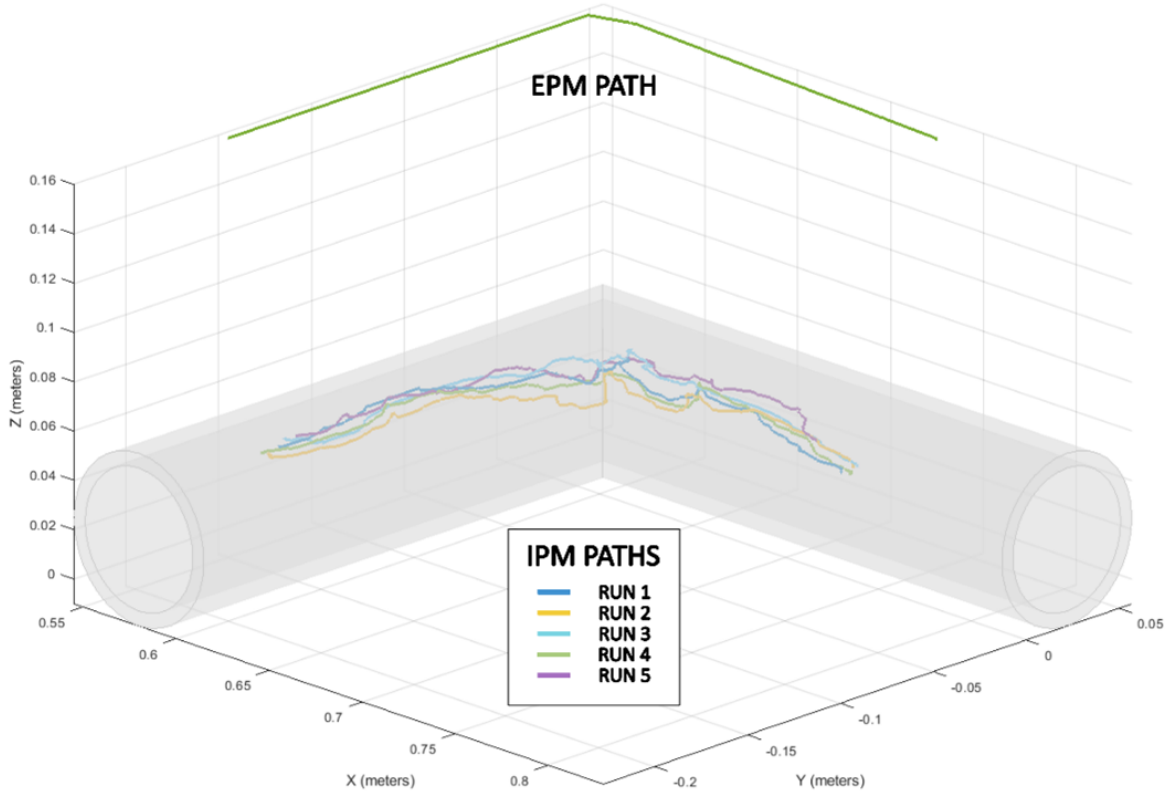

Figure B.2: 3D position data of the center of the EPM and IPM for 4mm/s for five repetitions.

B.2 Calculating of Bending Radii

The process for calculating bending radii relied on image analysis. Images were obtained of the final rest state of the MVR at the end of the EPM trajectory. From here, two concentric circles were fit to the robot's body (see Figure B.3) and their centre line (average radius) was taken as the robot's bending radius

Figure B.3: Calculating the bending radius.